The rotation of the halo of NGC6822 determined from the radial velocities of carbon stars

– Graham Peter Thompson –

Centre for Astrophysics Research
School of Physics, Astronomy and Mathematics
University of Hertfordshire

Submitted to the University of Hertfordshire
in part fulfilment of the requirements of the degree of
Master of Philosophy in Astrophysics

Supervisor: Professor Sean G. Ryan

– April 2016 –

Declaration

I hereby certify that this dissertation has been written by me in the School of Physics, Astronomy and Mathematics, University of Hertfordshire, Hatfield, Hertfordshire, and that it has not been submitted in any previous application for a higher degree. The core of the dissertation is based on original work conducted at the University of Hertfordshire, and some of the ideas for further work are drawn from topics studied during an earlier Master of Science. All material in this dissertation which is not my own work has been properly acknowledged.

– Graham Peter Thompson –

Acknowledgements

I thank Professor Ryan for his invaluable support and patient guidance as my supervisor, throughout this study. His incisive questioning, thoughtful comments, helpful suggestions and, at times, hands-on assistance throughout the study, preparation of a paper to MNRAS and the writing of this dissertation have been invaluable.
I thank also Dr Lisette Sibbons, whose work on the spectral classification of carbon stars in NGC 6822 was the genesis of my study. Dr Sibbons was responsible for the acquisition and reduction of the spectra I used in the study. She also provided me with background information related to the stars in the sample, and general advice. I would also like to thank Scott Croom (AAO) for undertaking the original AAOmega service observations and Sarah Brough (AAO) for her assistance to Dr Sibbons in reducing the original data.
This research uses services or data provided by the National Optical Astronomy Observatory (NOAO) Science Archive. NOAO is operated by the Association of Universities for Research in Astronomy (AURA), Inc. under a cooperative agreement with the National Science Foundation. IRAF is distributed by the NOAO.
Finally, I would like to thank the unknown referee for the useful comments provided on a paper reporting the results of the study and submitted to MNRAS for publication.

Abstract

The kinematics of stars in galaxies is becoming a key means to understand the dynamics of galaxies, their formation and merger history. For many years, kinematics has been measured using integrated field techniques in the optical, infra-red and radio wavebands, but modern CCD multi-channel cameras are now making it possible to measure the spectra of individual stars in galaxies and thus enabling more detailed analysis of galaxy kinematics.

Using spectra taken with the AAOmega spectrograph, I measure the radial velocities of over 100 stars, many of which are intermediate age carbon stars, in the direction of the dwarf irregular galaxy NGC 6822. Kinematic analysis suggests that the carbon stars in the sample are associated with NGC 6822, and estimates of its radial velocity and galactic rotation are made from a star-by-star analysis of its carbon star population. I calculate a heliocentric radial velocity for NGC 6822 of -51 ± 3 km s^{-1} and show that the population rotates with a mean rotation speed of 11.3 ± 2.1 km s^{-1} at a mean distance of 1.1 kpc from the galactic centre, about a rotation axis with a position angle of $25° \pm 14°$, as projected on the sky. This is close to the rotation axis of the HI gas disk and suggests that NGC 6822 is not a polar ring galaxy, but is dynamically closer to a late type galaxy. However, the rotation axis is not aligned with the minor axis of the AGB isodensity profiles and this remains a mystery.

Finally, further work is suggested which would examine stars in the galaxy outside the central sample for which I had data, to confirm my findings and to attempt to understand the misalignment of the rotation axis and isophotes. In addition, I suggest further work to constrain the dynamical mass of the galaxy, which up to now is not well determined.

Contents

List of Figures

List of Tables

1. Introduction

1.1. Overview

The measurement of radial velocity has played a pivotal role in the analysis and understanding of the cosmos. It provides a signature of the motion of objects tracing the distribution of matter and gravitational potential. The discovery of an expanding universe by Hubble [1925] was made from radial velocity measurements of galaxies, and Hubble's Law embodies radial velocity in its formulation, $V_{\rm rad} = Hd$, where $V_{\rm rad}$ is the radial velocity of a galaxy, H is the Hubble parameter and d is the distance to the galaxy. Radial velocity measurements have also been instrumental in the discovery of 'dark matter', first described in the German paper on the motion of extra-galactic clusters by Zwicky [1933], and later in spiral galaxies by van Albada et al. [1985] and others. These studies show that the kinematics of objects, under Newtonian gravitational theory, cannot be fully accounted for by the mass of observed luminous matter in the universe, and additional matter must be added. While it is unlikely that all baryonic matter has been discovered at present, contemporary cosmological theory does not contain sufficient baryonic matter to satisfy Newtonian dynamics, leading to the conjecture that much of the universe is made up of non-baryonic matter, which is usually referred to as dark matter.

The expansion of the universe and the presence of dark matter are embodied in modern cosmological theory as the Standard ΛCDM Cosmological Model, which is discussed in §1.2.1. In this model, Λ refers the cosmological constant, which is responsible for the acceleration of universe, and CDM to cold dark matter, responsible for the collapse of matter into the structure we see [Coles and Lucchin, 2002]. As we shall see in §1.2.1, there are insufficient baryons in the universe to account for the amount of matter required for structure formation so CDM usually refers to non-baryonic matter. The model has been quite successful in explaining the evolution of the universe and the formation of galaxies on large scales, yet it does not offer a complete solution to our understanding of cosmology, as it runs into some difficulties over small scales. These are discussed in §1.2.1. Recent surveys

Table 1.1.: Cosmological parameters from WMAP data releases 7 and 9, and Planck 2013 Results.

	Ω_Λ	Ω_c	Ω_b	H_0	Notes
WMAP7	0.725 ± 0.016	0.229 ± 0.015	0.0458 ± 0.0016	70.2 ± 1.4	1
WMAP9	0.712 ± 0.010	$0.2408^{+0.0093}_{-0.0092}$	0.0472 ± 0.0010	69.33 ± 0.88	2
Planck 2013	0.693 ± 0.019	0.2572 ± 0.0085	0.04809 ± 0.00134	67.9 ± 1.5	3,4

Ω_c and Ω_b are the present day values of cold dark matter and baryon densities, respectively, in the universe.
All errors are quoted at 68% confidence levels.

Note 1: Komatsu et al. [2011], Table 1. WMAP+BAO+H_0, using RECFAST 1.5 / v4.1 WMAP likelihood code.
Note 2: Hinshaw et al. [2013], Table 3. WMAP+BAO+H_0.
Note 3: Planck Collaboration et al. [2014b], Table 2. Planck temperature data plus lensing.
Note 4: Ω_c and Ω_b and their errors are derived from data in Planck Collaboration et al. [2014b], Table 2. (see Appendix A) for derivation.

of the cosmic microwave background, §1.2.2, by the Planck and WMAP spacecraft probes, have quantified the value of Λ and the amount of CDM in the universe, as shown in Table 1.1. These values imply that currently $< 5\%$ of the universe can be observed directly, and $> 95\%$ is inferred indirectly. It is thus very important to understand the physical nature of both dark energy and dark matter to validate present cosmological theories.

The study of kinematics in nearby (low$-z$) galaxies, both within and beyond the Local Group (LG), can give insight into dark matter, as they are all affected by it in differing degrees [Chernin et al., 2004, Karachentsev et al., 2009, McConnachie, 2012].

- LG galaxies are affected by four factors: the gravitational potential of the LG, the gravitational potential of other nearby galaxy clusters, cosmological expansion and the dynamical history of each galaxy, e.g. past mergers.

- Many LG galaxies are dwarf spheroidal (dSph) types, which are discussed more in §1.3.2. They typically have a very high mass to light ratio[1], Υ, as they are faint but their velocity dispersions imply a high dynamical mass. Such galaxies are good candidates for researching dark matter in the nearby region.

- Irregular galaxies tend to be few and to lie in the outer half of the LG [Karachentsev et al., 2004, McConnachie, 2012]. They are gas rich and star forming, so they are much brighter than dSphs and have a much lower Υ. It is

[1]Mass to light ratio, $\Upsilon = \mathcal{M}/\mathcal{L}$, where $\mathcal{M}$ is the mass of a galaxy in solar units, $\mathcal{M}_\odot$, and $\mathcal{L}$ is the luminosity of the galaxy also in solar units, $\mathcal{L}_\odot$. Υ is often also quoted in solar units, $\Upsilon_\odot = \mathcal{M}_\odot/\mathcal{L}_\odot$.

not obvious whether these are bound to the LG, or just visiting, nor whether they are or have been tidally disrupted to cause the star formation.

- At the border of the LG, the gravitational potential of the LG is just in equilibrium with external gravitational potentials and the cosmological expansion (Hubble Flow). The dynamical behaviour of objects close to the border might reveal some signature of this [Karachentsev et al., 2009, Karachentsev and Nasonova, 2010, Chernin et al., 2010].

An opportunity to study the kinematics of the resolved, intermediate age stellar population of the dwarf irregular galaxy NGC 6822, within the LG, arose as an extension of work already undertaken by Sibbons et al. [2015], where spectra had been obtained and reduced for stellar classification. Although the original spectra were not optimised for radial velocity measurement, it was proposed that they would provide a platform to learn about the interpretation of spectra and to obtain radial velocities from them. Soon after starting, it was realised that it was possible to distinguish between members of NGC 6822 and foreground stars in the Milky Way and that the analysis tools available could be used to obtain useful velocity results from the spectra. This led to the discovery of a rotating population of intermediate age stars in the halo of NGC 6822, which constitutes the core of this dissertation.

1.2. Cold dark matter and structure formation

1.2.1. Standard ΛCDM Cosmology

Modern gravitational theory on the largest scales and over the largest extremes is based on general relativity (GR). In its first formulation, it predicted a number of cosmological phenomona, which have been observed subsequently, such as black holes, time dilation due to gravitational acceleration by massive objects, and most recently, direct evidence of gravitational waves [Abbott et al., 2016, Abbott, 2016].

Contrary to scientific opinion at that time, that the universe is static, GR predicted a dynamic universe, which led Einstein to include a term, the cosmological constant, into his field equations to counteract gravity and create a static universe. Hubble's discovery of an expanding universe [Hubble, 1925] changed this perception. Initially, it was believed that, although expanding, the rate of expansion would be slowed by gravity [Friedmann, 1922], but over the last decade and a half, it has became clear that the expansion is being accelerated, [Riess et al., 1998, Perlmutter

et al., 1999]. The term now has scientific significance and is referred to as the Cosmological Constant, Λ. It has been accurately measured by a number of satellite based and earth based surveys, see Table 1.1, but its physical origin is unknown. It is commonly called 'dark energy' or sometimes 'vacuum pressure' to provide some impression of its role.

Friedmann's interpretation of GR [Friedmann, 1922] results in a well known suite of equations, which, amongst other factors, are affected by the geometry of the universe[2]. The Friedmann equations show that at a critical matter density, ρ_c, the universe will be flat. Modern cosmological measurements [Komatsu et al., 2011, Planck Collaboration et al., 2014b] show that the density of the universe is close to ρ_c [Coles and Lucchin, 2002]. The difficulty is that observed luminous matter, which is made up of baryons, is not sufficient to reach ρ_c on its own. Calculations of the number of baryons produced during nucleosynthesis shortly after the Big Bang also fall well short of the amount required to reach ρ_c [Coles and Lucchin, 2002]. Table 1.1 shows measurement results for cosmological parameters. Ω represents the ratio of density of dark energy, dark matter or baryons to the critical density, $\Omega = \rho/\rho_c$.

Modern theory states that the shortfall in baryonic mass is made up by non-baryonic particles which do not interact strongly with radiation, but do interact with gravity. There are many species of particle which are proposed for non-baryonic dark matter, most of which are yet to be discovered. A detailed discussion of many of the types can be found in Feng [2010]. The favoured variety is known as a weakly interacting massive particle, 'WIMP'. These particles have a mass which is considerably heavier than a hydrogen nucleus, and they move slowly. Thus their kinetic energy is low and the generic term for them is cold dark matter, CDM. Their synthesis is not predicted from the standard model of particle physics but from super-symmetry (SUSY). Neither the particle itself nor the SUSY theory is yet proven by test or observation.

So the standard ΛCDM model of cosmology attributes dark energy to driving expansion and non-baryonic dark matter to driving contraction through increased gravity. While ΛCDM has been remarkably successful at predicting the behaviour of the universe on large scales, it runs into some problems at smaller scales, which are listed below:

- *The 'missing satellites' problem.* The first discussion of this problem was by Klypin et al. [1999], who performed $N-$body simulations of the growth

[2]see Coles and Lucchin [2002] for discussion of open, closed and flat models of the universe

of structure within the ΛCDM paradigm. At the time of the simulations only about 30 satellite galaxies of the Local Group (LG) were known. The simulation traced the growth of dark matter halos and predicted that in a region similar to the LG, ≈ 280 dark matter halos should be present. This prompted the question "Where are the missing galaxies?", which assumes that all dark matter halos will contain a galaxy. A number of later simulations, such as Aquarius [Springel et al., 2008] and Via Lactea [Zemp, 2009], have been performed with similar results.

Discoveries of more satellites since the publication of the original study have closed the gap significantly and further discoveries may still be made with wider and deeper surveys which are ongoing or planned. Tollerud et al. [2008] compares the numbers of dark matter halos predicted by the Via Lactea simulation with an estimate of the numbers of new galaxies likely to be discovered with present day surveys in progress. 18 different scenarios in Via Lactea result in a wide range in the number of dark matter halos, from 69 to 1093 with a mean of 375, yet the number of new discoveries likely at an apparent magnitude of 27.5 or brighter is 283. This limit is at least 2 to 3 magnitudes fainter than current surveys, so that experimental validation will have to wait.

It would appear that this problem is not yet understood, and this has been one of the motivations for warm dark matter (WDM), which produces many fewer dark matter halos in simulations [Lovell et al., 2012]. Klypin et al. [2015] have extended their analysis of the number of dark matter halos over ~ 10 Mpc from the LG barycentre for both the CDM and WDM paradigms. Their original conclusion that the CDM paradigm produces far more dark matter halos in the region than are observed as galaxies remains. The WDM paradigm performs better, but it under-predicts the number of small halos compared with the number of such galaxies observed, and over predicts the number of large halos, the crossover being at a galactic virial mass $M_{\rm vir} \lesssim 10^9 h^{-1}\ M_\odot$.

- *The 'Too Big to Fail' (TBTF) problem.* This is essentially a re-interpretation of the missing satellites problem. In the recent simulations, a variety of dark matter halo sizes is predicted. Large simulated halos are expected to host galaxies, and their predicted rotation velocities should match those observed [Boylan-Kolchin et al., 2011]. However, they do not [Boylan-Kolchin et al., 2011], which prompts the question why these large halos appear to have failed to produce a galaxy. Most $N-$ body simulations consider only dark matter halos and exclude the effects of baryonic content in real galaxies, which may

be a cause and Boylan-Kolchin et al. [2011] even considers whether DM halos exist at all.

A number of authors [Zolotov et al., 2012, Di Cintio et al., 2014, Chan et al., 2015, Papastergis and Shankar, 2015] have attempted to examine what the impact is of baryons on dark matter halos, through infall, star formation efficiency, outflows. In general, by applying baryonic feedback of this type, the density of the cores is spread out more than dark matter simulations would suggest. The density in the core is much reduced, and rotation velocities similarly reduced. Moreover, this effect is greater the more baryons there are in the halo, as their feedback effects are greater. So large galaxies have a proportionately lower rotation rate than small ones which could explain why DM-only simulations over-predict high mass halos, leading to a bias in the observations.

Zolotov et al. [2012] shows that DM-only simulations produce denser halos when neglecting baryonic affects and Di Cintio et al. [2014] shows that baryons affect the shape of the central core of the galaxy density profile, particularly at high star formation efficiencies, which becomes flatter. Chan et al. [2015] deduces that baryonic feedback in this manner could explain the 'Too Big to Fail' problem without the need for non-standard dark matter models.

- *The core/cusp problem.* Navarro et al. [1997] first proposed a density profile for dark matter halos, which has since become known as the NFW profile, equation (1.1). This density profile is ubiquitous in $N-$body simulations.

$$\rho = \frac{\rho_0}{(r/r_{200})(1 + r/r_{200})^2} \tag{1.1}$$

where r is a radial coordinate from the centre of the halo and r_{200} is normally taken to be the radius at which the mean density is $200\times$ the cosmological critical density [Binney and Tremaine, 2008].

The formulation, however, contains a term, r^{-1}, which results in a cusp, or singularity, at the centre of halo, where $r = 0$, and there has been much discussion over how real this is. Recent work introducing baryonic feedback effects into simulations, such as described above, appear to show that the central region is smoothed into a physically satisfactory core by their introduction, suggesting that the problem has now been explained in this manner.

Until dark matter is unequivocally discovered, alternative theories will persist. For completeness, two other candidates for cosmological models will be summarised

here. The first is the so-called ΛWDM model, where compared to ΛCDM very much lighter and faster moving dark matter particles exist, hence 'warm dark matter' [de Vega and Sanchez, 2010, Destri et al., 2012]. Such particles are believed to be about $10^{-3}\times$ lighter than the electron, and simulations suggest they solve the missing satellites problem. The second is modified Newtonian dynamics, MOND [Milgrom, 1983, Famaey and McGaugh, 2011], where the power law in the equations of motion changes in regions where the acceleration due to gravity, g, is less than a critical value, a_0, suggesting that matter has a bigger effect on the acceleration of a particle than expected under Newtonian gravity in these regions. Taking this a step further it could be argued that if the matter content is constant then G would have to change. a_0 has been calculated to be $\approx 10^{-10}$ m s^{-2} which is interestingly, or maybe coincidently, $\equiv cH_0/2\pi$. Both theories have adherents, who continue to work them and will do so, until dark matter is discovered and its nature is fully understood.

1.2.2. Cosmic Microwave Background (CMB)

One of the most important discoveries of the 20th century, was the observation of an isotropic background of radiation in the microwave band. It was discovered by two Bell Labs radio engineers, Penzias and Wilson, in 1964, for whom it was a source of noise which could not be eliminated. This coincided with work being done at Princeton University to build a radiometer to measure the temperature of the universe. The source of the noise was originally predicted by Alpher and Hermann in 1940 as a consequence of the cooling of the universe after the Big Bang and has became known as the Cosmic Microwave Background (CMB).

At the time of its discovery, the CMB appeared to be a homogeneous noise source, but since then, it has been measured with ever more precise instruments. Figure 1.1 shows the most recent measurement of the CMB by the Planck Collaboration.

After the Big Bang, the temperature of the universe fell rapidly. Protons, neutrons and electrons formed in the first second after the Big Bang, but the temperature of the universe at this time was too high for nuclei to form, as the energy of the photons was higher than the dissociation energy of the nuclei [Coles and Lucchin, 2002]. At this epoch, the universe was radiation dominated. After about 1 second, it became cool enough for nuclei to form, and after about 15 minutes, approximately the half-life of an unbound neutron, the chemistry of the primordial universe was fixed, hydrogen-1 (75%) and helium-4 (25%) with traces of heavier isotopes such as deuterium, helium-3, and lithium-7 [Coles and Lucchin, 2002].

The universe remained radiation dominated and continued to expand, until at

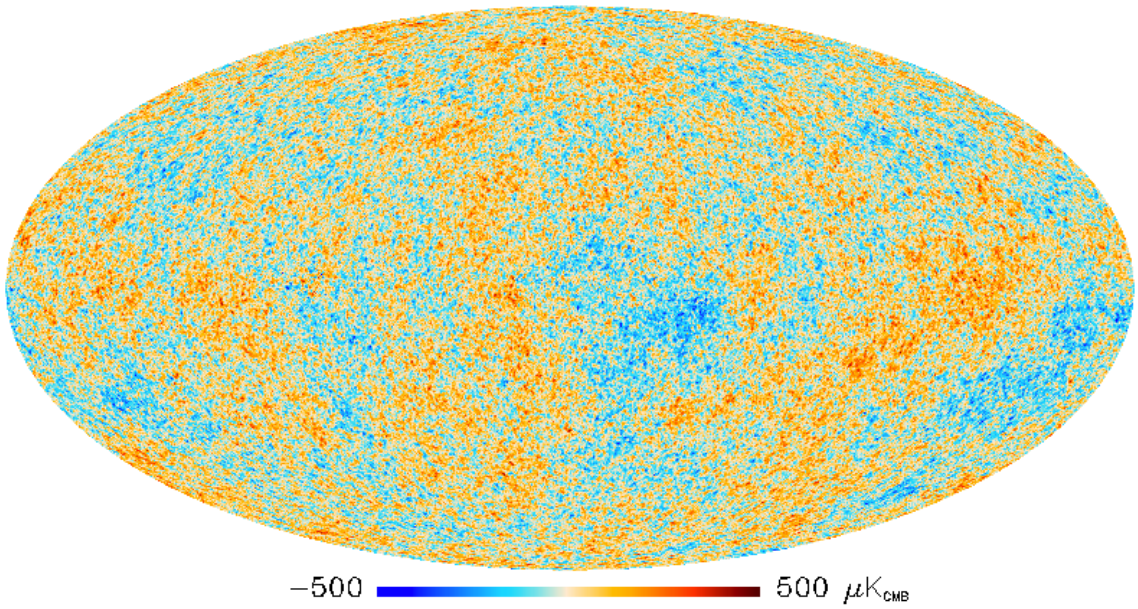

Figure 1.1.: Planck Collaboration 2013 image of the CMB.
The image shows the variations of temperature about a mean temperature of 2.72548± 0.00057 °K [Fixsen, 2009]. The orange points are hotter regions, the bluer points are the cooler regions. The temperature variation between orange and blue is ±500 μK. Denser regions have a larger potential well and owing to the Sachs-Wolfe effect, photons lose more energy leaving a deeper potential well and therefore become cooler (i.e. bluer in this figure). Structure filaments grew from the cooler, denser regions, shown in blue, and voids from the hotter, less dense regions, shown in orange.
Image credit: ESA and the Planck Collaboration [Planck Collaboration et al., 2014a]

$\sim 60,000$ years, it became matter dominated [Binney and Tremaine, 2008], but it was still hot enough that atoms could not form and it existed as a hot ionised plasma containing ions. The mean free path of photons was short, resulting from Thomson scattering. Photons were unable to freely stream so that the plasma was opaque and glowing. It remained so for $\sim 380,000$ years [Coles and Lucchin [2002], Liddle [2003], Binney and Tremaine [2008]] when eventually, the plasma cooled sufficiently for the photon energy to fall below the dissociation energy of atoms, which allowed nuclei and electrons to form atoms of neutral gas. The universe became de-ionised and photons could stream freely away, so that the universe became transparent [Liddle [2003], Binney and Tremaine [2008]]. This epoch, at $z = 1100$, is called 'recombination'. The CMB observed is the last scattering surface (LSS) presented to us by the plasma immediately at the point of recombination [Binney and Tremaine, 2008, Coles and Lucchin, 2002, Liddle, 2003]. While ionised, the plasma was in magnetohydrodynamic motion and at the point of the recombination, the state of the density fluctuations in the plasma were imprinted in the temperature variations now observed in the CMB, see Figure 1.1.

1.2.3. Galaxy formation.

The density fluctuations indicated in the CMB have, over time, given rise to the structure in the universe, resulting in a cosmic web of filaments of dark matter, baryonic matter, stars and galaxies surrounded by voids of very low density. The higher density regions had a deeper gravitational potential, causing primordial gas to infall from the surrounding less dense regions. This resulted in the formation of filaments of gas surrounded by voids. The filaments grew in density until eventually stars and galaxies could form. Present theory is that dark matter filaments formed prior to recombination, providing the structure for the growth of the cosmic web, and these are traceable in the CMB power spectrum.

Prior to the formation of the first stars and galaxies, the universe was dark. Collapse of gas in dense regions resulted in the formation of the early (Population III) stars, and the early galaxies. The stars are thought to be much bigger than the Sun for example and very short lived so we do not see any trace of them now, although their supernovae would have seeded the universe with the first metals. The collapse can be quantified by Jeans' Theory, which stated qualitatively, says that as a cloud of gas cools, its kinetic energy (and thus thermal pressure) falls until at a critical point, self-gravity will cause it to collapse. The point at which collapse occurs depends on the radius, mass and temperature of the original cloud. As the cloud shrinks, its potential energy is released. Half is radiated away and half increases the internal temperature and pressure of the cloud. This temporarily slows the collapse, but does not stop it. At this stage, a cloud has formed a 'protostar' which slowly collapses under self-gravity until its core is hot enough for nuclear fusion of hydrogen to take place at the centre, when a star is born. Clouds may fragment and each cloudlet may collapse to form a star, thus forming stellar clusters.

Dense regions attract more and more matter even up to galactic scales. Galactic clusters commonly form within the cosmic web and then galaxies fall in on each other and merge. Major mergers occur when two galaxies of similar mass interact and the effects can be very disruptive. Existing stars can be ejected from the galaxies and form streams of stars flowing away from the merger centre. These are sometimes called antenna galaxies. The gas is compressed and star formation on a large scale starts up making the galaxies very bright with new stars. Minor mergers occur where the colliding galaxies are significantly different in mass; the smaller of the galaxies is usually tidally disrupted / shredded and the stars within it tend to end up absorbed into the halo or thick disk, if present, of the larger galaxy. The process continues in the present epoch. The MW has several examples of stellar streams

in its halo [Morrison et al., 2000, Belokurov et al., 2006, Belokurov et al., 2007, Guhathakurta et al., 2006, Starkenburg et al., 2009], which are believed to be the result of minor mergers leaving their trace.

This evolutionary process has been studied many times. Using ΛCDM cosmology and CMB density variations as priors, $N-$body simulations have been performed to evolve the growth of the cosmic web and structure from primordial times to the present day. These typically simulate matter particles in a homogeneous three dimensional fluid and progress their dynamics step by step over time in the context of the evolving gravitational potential. For the entire universe, this is a major computing challenge.

One of the most recent cosmological simulations of galaxy evolution is the Millennium Simulation performed at the Max Planck Institute for Astrophysics, between 2003 and 2014. A first simulation used 10^{10} particles in a $500h^{-1}$ Mpc cube, where h is the Hubble parameter expressed in units of 100 km s^{-1} Mpc^{-1} at a spatial resolution of $5h^{-1}$ kpc, which is approximately the distance of the Sun from the centre of the MW. It followed the formation and evolution of $\sim 10^7$ objects brighter than the SMC, and its first results were published in 2005. In 2008, a second simulation was run with much finer mass resolution and published in Guo et al. [2011]. In 2012, the simulation was re-run with WMAP7 updated cosmological parameters and with the Planck 1st data release cosmology in 2014. The history of the development of the Millenium Simulation over the past decade or so is well described on the following Max-Planck Institute website http://wwwmpa.mpa-garching.mpg.de/millennium/.

A large scale image of one part of the simulation at $z = 0$ is shown in Figure 1.2 [Springel et al., 2005] and clearly shows the filamentary nature of the evolved universe. The filaments represent regions of high density dark matter where gas collects. At filament intersections, the density is highest and galaxies develop as star formation within the gas occurs.

Two surveys, the 2dF survey [Colless et al., 2001] and the Sloan Galactic Survey [Blanton et al., 2003] completed since the turn of the century have revealed further structure in the cosmos. Figure 1.3 shows the structure observed by these surveys and a marked similarity to each other, despite covering slightly different slices of the sky, showing filamentary structures and voids, very similar to those in the simulated structure in Figure 1.2.

The first such survey to be performed was the CfA Redshift Survey which started in 1977 and was completed in 1982, performed by Harvard-Smithsonian Institute for Astrophysics. A description of its development can be found on the Harvard

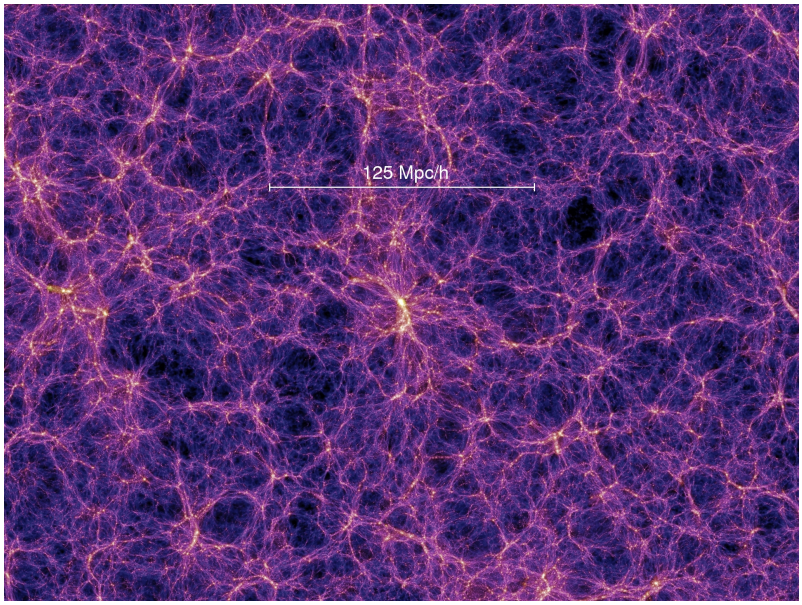

Figure 1.2.: Millennium Simulation
The image shows a structure of filaments and intersections of matter particles at $z = 0$. Galaxies tend to form at the intersections from gas falling into the filaments. The bright spot at the centre of the image is a typical galaxy forming intersection. The regions outside the filaments become voids and contain little gas.
Image credit: Millennium Simulation at Max-Planck-Institute for Astrophysics [Springel et al., 2005].

website https://www.cfa.harvard.edu/~dfabricant/huchra/zcat/. Its second, more detailed survey of over 18,000 galaxies in the northern hemisphere produced the first indications of a web like structure in the universe [Geller and Huchra, 1989], including the discovery of voids and the 'Great Wall'.

1.2.4. The Local Group

At the time of writing, there are more than 75 confirmed galaxies within a radius of 1 Mpc of the barycentre of the LG [McConnachie, 2012][3] [Karachentsev et al., 2009]. There are two large spiral galaxies, MW and Andromeda (M31), which together dominate the gravitational potential of the group, and one smaller spiral galaxy (Triangulum). Andromeda has an elliptical companion, M32. There are 7 irregular / dwarf irregular galaxies: LMC, SMC, IC 10, IC 1613, NGC 6822, WLM, Leo A, and 58 dwarf spheroidal, suspected dwarf spheroidal or dwarf elliptical galaxies. Galaxies are classified as dwarf if their $M_V > -18$. At present, four other galaxies cannot be differentiated between dwarf irregular or dwarf spheroidal and a further two could

[3]The catalogue in McConnachie [2012] covers objects out to 3 Mpc, is fully referenced and draws upon other catalogues (e.g. NED, Karachentsev). It is maintained on-line and was last updated in September 2015 with recent discoveries.

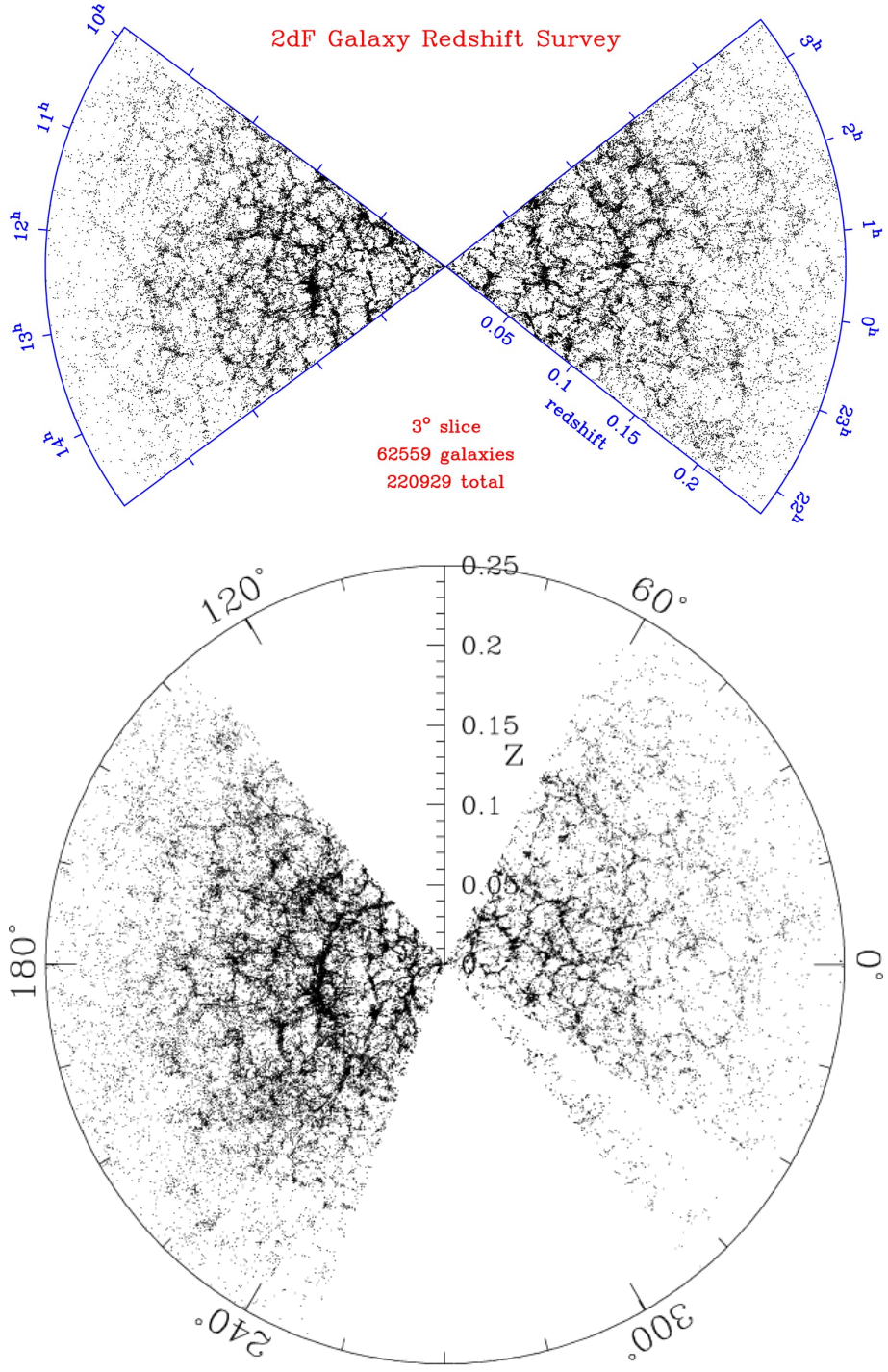

Figure 1.3.: Galactic Surveys
Upper panel, 2dF survey showing present day filamentary structure in regions of low z [Colless et al., 2001]. The survey views planes in the southern hemisphere. The structure fades at higher z, but this may be due to limitations of the measuring equipment. Lower panel, Sloan galaxy survey, 6° slice from DR1 [Blanton et al., 2003], Image credit: Sloan Digital Sky Survey. Although covering a different plane in the northern hemisphere, the observed structure is similar to 2dF. Some large features are noticeable, including the Sloan Great Wall.

be either globular clusters or dwarf satellites. In addition, the catalogue has recently re-classified the dwarf galaxies Canis Major and Bootes III to 'ambiguous'. There are a further 23 newly discovered galaxies which are not yet confirmed as members of the LG.

The LG barycentre lies between MW and M31, and within the LG, dwarf spheroidals are spread fairly evenly in distance from 153 kpc from the barycentre to 969 kpc, whereas the dwarf irregulars tend to congregate towards the outer region of the LG (440, 517, 556 − 941 kpc). The LMC and SMC lie at 421 and 422 kpc respectively, with Triangulum at 442 kpc and M31 at 392 kpc [McConnachie, 2012].

Figure 1.4 indicates that galaxies lying inside a radius of $\sim$ 1 Mpc of the LG barycentre exhibit both positive and negative radial velocities, while galaxies lying outside exhibit only positive (red-shifted) radial velocities. It is believed that the galaxies outside $\sim$ 1 Mpc are dominated by the Hubble expansion (Hubble Flow) and by infall towards nearby galaxy clusters (e.g. the Virgo Cluster), abd those inside $\sim$ 1 Mpc appear to be dominated by the gravitational potential of the LG [Chernin et al., 2010, Karachentsev et al., 2009, McConnachie, 2012]. In McConnachie [2012] the calculation of barycentric velocities from the heliocentric radial velocity is explained as follows. In principle, the calculation assumes that the barycentre lies midway between MW and M31. It then converts radial velocities into a LG frame using the method developed by Karachentsev and Makarov [1996], and subtracting the velocity component of the MW in the direction of each galaxy.

At the boundary between these two paradigms is a surface of zero velocity where the gravitational force generated by its matter is in equilibrium with the cosmological expansion and other external gravitational forces. Six galaxies lie close to this surface: WLM (dIrr) (794kpc), Leo A (dIrr) (941 kpc), Aquarius (dIrr/dSph) (1053 kpc), Tucana (dSph) (1076 kpc), SagDig (dIrr) (1156 kpc) and UGC4879 (dIrr/dSph) (1321 kpc) [McConnachie, 2012]. They are all dwarf irregular galaxies or dwarf elliptical galaxies with irregular features. Irregular galaxies are possibly being tidally disrupted or have been in the past, and if they have gas they will tend to be star forming.

1.2.5. Contemporary Local Group Surveys

Many of the galaxies now catalogued within the LG, and indeed outside it, were unknown until the turn of the 21st Century, when the Sloan Digital Sky Survey (SDSS) provided photometric and spectroscopic data of objects in the northern hemisphere. Up to now, SDSS has mapped 14,555 square degrees of the full sky (approximately

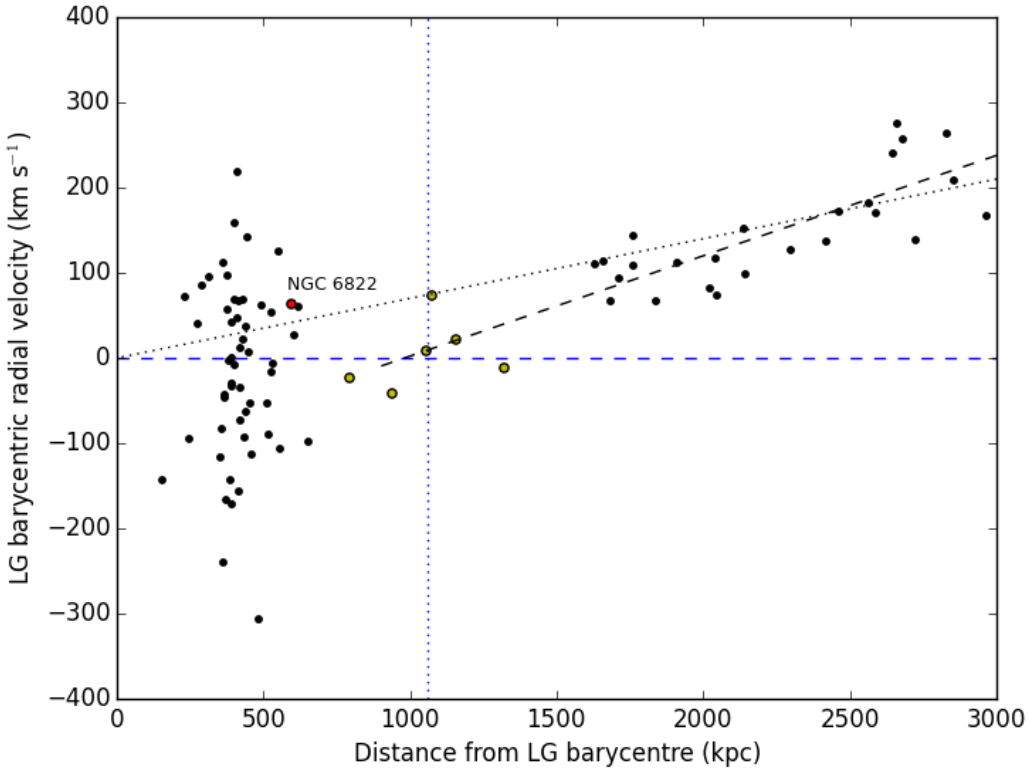

Figure 1.4.: Plot of barycentric radial velocities against distance from the LG barycentre based on data from Table 2 of McConnachie [2012], for all galaxies which have a value for barycentric radial velocity. NGC 6822 is shown in red. It can be seen that beyond 1500 kpc, galaxies follow a Hubble-like velocity increment with distance. The dashed line is a least squares straight line fit for the galaxies which lie beyond 1500 kpc. The dotted line represents Hubble Flow, where $H_0 = 70$ km s^{-1} Mpc^{-1}. Below ~ 1000 kpc LG gravity dominates and radial velocities are dispersed positively and negatively (i.e. red shifted and blue shifted). The vertical line at 1060 ($\pm$70) kpc represents the zero-velocity surface derived from the mean distance of the dwarf galaxies WLM, LeoA, Aquarius, Tucana, SagDIG, UGC4879, which lie in that order between 794 kpc and 1321 kpc [McConnachie, 2012].

35%), to a magnitude depth of $m_{\rm app}$ = 22.0, 22.2, 22.2, 21.3, and 20.5 over 5 bands *ugriz* respectively. Technical data can be found on the SDSS websites: http://classic.sdss.org/dr7/ (data release 7), and http://www.sdss3.org/dr8/ (data release 8). Data release 12 [Alam et al., 2015] is the most recent. Analysis of the data has revealed many more faint galactic objects within the LG than were previously known. Since 2001, the SDSS discoveries have revealed $\sim$ 40 dwarfs.

Although SDSS continues to deliver data and results, other surveys are now being undertaken and are starting to yield more discoveries. These surveys cover a much greater area of sky and will also probe 2 to 3 magnitudes deeper. Within the last year, several papers from the Dark Energy Survey (DES), a ground based survey using Gemini N and S telescopes, covering both hemispheres, have revealed the discovery of 16 very faint objects which are thought to be possible LG dwarf galaxies, although most yet have to be confirmed. These are included in Table 1.2.

Four new discoveries from the Pan-STARRS survey in the northern hemisphere have also been published. While its primary role is to search for near earth objects, it completed its first full sky survey in 2014, which led to the discoveries. These are also included in Table 1.2. Pan-STARRS covers a total of 30,000 square degrees of the sky ($\sim$ 73%) from Hawaii. At 6000 square degrees per night, it covers its entire field of view over 5 nights and in 5 filters (*grizy*), to a limiting $m_{\rm app}$ of 24. Some technical data can be found on the following website: http://pan-starrs.ifa.hawaii.edu/public/design-features/wide-field.html).

In the southern hemisphere, the Australia National University is undertaking a southern sky survey (SkyMapper) covering approximately 20,000 square degrees in 6 bands (*uvgriz*) to a limiting $m_{\rm app}$ = 20.5, 20.5, 21.7, 21.7, 20.7, 19.7 respectively with an exposure time of 100 seconds per exposure. One of the stated goals is to search for new dwarf galaxy companions to the Milky Way. The telescope saw first light in 2008 but the full sequence survey is less than 10% complete. A short survey aimed at calibration using stars and based on 5-second exposures, where the limiting $m_{\rm app} \sim 16$, is almost complete; http://rsaa.anu.edu.au/research/projects/skymapper-southern-sky-survey.

ESO is developing a new multi-feed spectrograph for use on its very large telescope (VLT) http://www.eso.org/sci/publications/announcements/sciann16020.html and http://www.roe.ac.uk/~ciras/MOONS/VLT-MOONS.html. It will be able to harness the collecting power of the 8.2 m telescope. The Multi Object Optical and Near-infrared Spectrograph (MOONS) will be able to simultaneously measure $\sim$ 1000 objects in the near infra-red. In the I-band and targeted at the the Ca II triplet it will have a resolving power of $\sim$ 9000. It is currently in the early de-

Table 1.2.: Recent discoveries of faint LG objects up to 20 September 2015 [McConnachie, 2012]

No.	Galaxy names	References	Survey
(8)	Tucana III, Grus II, Columba I, Tucana IV,Reticulum III, Tucana V, Indus I, Cetus II	Drlica-Wagner et al. [2015]	DES
(7)	Reticulum 2, Eridanus 2, Horologium I,Pictoris 1,Phoenix 2, Eridanus 3, Tucana 2	Koposov et al. [2015], Bechtol et al. [2015]	DES DES
(1)	Grus 1	Koposov et al. [2015]	DES
(1)	Kim 2	Kim et al. [2015b], Koposov et al. [2015], Bechtol et al. [2015]	Stromlo DES DES
(1)	Pegasus 3	Kim et al. [2015a]	SDSS/DES
(1)	Horologium 2	Kim and Jerjen [2015]	DES
(2)	Draco II, Sagittarius II	Laevens et al. [2015a]	PanStarrs
(1)	Triangulum II	Laevens et al. [2015b], Kirby et al. [2015a]	PanStarrs ...
(1)	Hydra II	Martin et al. [2015] Kirby et al. [2015b]	DES ...
Three new dwarfs lie beyond 1 Mpc:		Antlia B [Sand et al., 2015], KK 258 [Karachentsev et al., 2014], KKs3 [Karachentsev et al., 2015a,b].	

sign stage having just passed its preliminary design review and is expected to be in operation from 2019.

The total number of new objects within 1 Mpc of the barycentre now stands at 23, 16 as a result of the first year of operation of the Dark Energy Survey, 4 from Pan-STARRS and 3 from the Stromlo MW Survey. All are currently considered ambiguous objects, either globular clusters or dwarf satellites. Table 1.2 lists these most recent discoveries.

Many of the new satellites discovered are elliptical and very faint. They are believed to be very old and no longer forming stars. Radial velocity dispersions from integrated light spectroscopy are very high, consistent with a high mass, even though their luminosities are low.

If the discoveries continue at the present rate with the deeper and wider surveys of PanSTARRS and DES, then it might be expected that ~ 80 more dwarf objects might be discovered over the whole sky bringing the total to ~ 150, which is $> 50\%$ of Klypin et al. [1999]'s prediction.

1.2.6. Mass-to-light ratio

The mass-to-light ratio, Υ, already introduced in §1.1, is a commonly quoted galaxy property and is the ratio of the dynamical mass of a galaxy, $\mathcal{M}$, and its integrated luminosity, $\mathcal{L}$, quoted in solar units. Dynamical mass is measured by observing the velocity dispersion of galaxies, usually in integrated optical or radio spectra, and luminosity is measured photometrically. The mass-to-light ratio of galaxies varies over a wide range depending on galaxy type.

Faint galaxies appear to have a proportionately greater Υ than their brighter siblings. In the solar neighbourhood, $\Upsilon \sim 2$ to $2.5\ \Upsilon_\odot$ and the Milky Way is estimated to have $\Upsilon = 70^{+100}_{-63}\ \Upsilon_\odot$ [Binney and Tremaine, 2008], although the errors are large owing to the uncertain quantity of dark matter in the Galactic halo. Typically dwarf elliptical and dwarf spheroidal galaxies, see §1.3.2, range from $\sim 200\ \Upsilon_\odot$ to $500\ \Upsilon_\odot$. Dwarf spheroidal galaxies (dSphs) appear to be abundant in comparison with other galaxy types, particularly in the LG. They are faint, and some are ultra-faint and extremely dispersed. These values are similar to the average cosmological $\Upsilon \approx 220 \pm 80\ \Upsilon_\odot$ [Binney and Tremaine, 2008], which would imply that they are strongly dominated by dark matter.

Following the recent Pan-STARRS discovery of Triangulum II, Kirby et al. [2015a] has estimated $\Upsilon \sim 3600^{+3500}_{-2100}\ \Upsilon_\odot$, which is by far the largest mass-to-light ratio claimed for a galaxy of the LG and suggests an ultra-faint, very massive object. These high Υ objects have been proposed as good laboratories for the study of dark matter.

1.2.7. Dynamics at the Local Group boundary.

The ΛCDM cosmological model implies that on large scales the Hubble flow dominates and at small scales gravity dominates. The Hubble flow is driven by the cosmological constant, Λ, and gravity is governed by dark matter. This leads to a conjecture that at some point - the zero velocity surface referred to above - there should be a crossover from one regime to the other, and that a transition region should exist around objects or clusters of objects. Outside this region the Hubble flow dominates and inside gravity dominates, and this may leave some trace in the kinematics of objects in the region.

Work has been published in the recent past on transition regions in the Local Group (LG) and on the Virgo cluster [Karachentsev et al., 2009, Chernin et al., 2010], which take place at a zero-velocity surface surrounding galaxy groups. For the LG, the radius of the zero-velocity surface from the barycentre has been vari-

ously calculated [Karachentsev et al., 2009, McConnachie, 2012] and lies at a radius $R_{\rm LG} \approx$ 1 Mpc. Karachentsev et al. [2009] provide values for the radius of the zero velocity surface, $R_0 = 0.94 \pm 0.05$ Mpc for $H_0 = 70$ km s^{-1} Mpc^{-1}, $R_0 = 0.96 \pm 0.03$ Mpc for $H_0 = 72$ km s^{-1} Mpc^{-1}, using the velocities of 20 galaxies lying between 0.7 and 3 Mpc from the LG barycentre. Six galaxies (Leo A, Tucana, WLM, Sagittarius dwarf irregular, Aquarius and UGC 4879) lie close to the zero-velocity surface, and McConnachie [2012] uses their mean distance to derive the radius, $R_{\rm LG}$, of the zero-velocity surface at 1060 ± 70 kpc, which is shown in Figure 1.4. In comparison Karachentsev et al. [2009] obtains $R_0 = 0.98 \pm 0.05$ Mpc from the same 6 galaxies. The zero-velocity surface for the Virgo Cluster (distance ~ 16.5 Mpc) falls at radius $R_{\rm VC} \approx 10$ Mpc [Chernin et al., 2010], well outside the zero-velocity radius of the LG.

These 6 galaxies all appear to be irregular and should contain red giant branch (RGB) and asymptotic giant branch (AGB) stars bright enough for radial velocity measurement. HI gas velocities and rotation are already known for these galaxies but there is virtually no information concerning the kinematics of the stellar population. The dynamical behaviour of the gas is governed by gas equations and particle collisions and is likely to be quite different from stars. The two populations will normally give different results.

Making radial velocity measurements may enable examination of how much the slope of the radial velocity per unit distance in Figure 1.4 is attributable to the Hubble Flow and how much is attributable to the gravitational forces of the LG, the Virgo cluster and other nearby clusters. Making radial velocity measurements of the six dwarf galaxies close to the zero velocity surface of the LG may also may help to separate out the dynamical histories of the galaxies and explain why this region appears to be so devoid of galaxies.

1.3. Galaxies

1.3.1. Galaxy classification

Before presenting the analysis of NGC 6822, it is appropriate to say a little more about the different kinds of galaxies found in the LG and beyond. Galaxies are classified in terms of their apparent shape in the sky. One of the first attempts to classify galaxies was performed by Hubble in his 'Realm of the Nebulae' [Hubble, 1936] and is shown in Figure 1.5. The classification followed the shape of a tuning fork with elliptical galaxies at the left hand side and spiral galaxies on two branches

on the right hand side. In Hubble's time, it was believed that elliptical galaxies were the progenitors of spiral galaxies, so they came to be called early types, and spirals as late types. Nowadays, this evolutionary model is no longer accepted, if anything ellipticals are probably the result of major mergers of spirals, not the reverse, but the terms are still used.

Elliptical galaxies tend to be gas poor and have few young stars [Sparke and Gallagher, 2007], thus they are made up of old stars and are therefore generally redder in colour. Their shape becomes increasingly more elliptical as the sequence moves to the right, from E0 to E7 in Figure 1.5. En indicates the eccentricity of the ellipse where $n = 10[1 - (b/a)]$, a is the major axis of the ellipse as projected on the sky and b the minor axis [Binney and Merrifield, 1998].

Spiral galaxies tend to have an old redder central bulge but are actively star forming in the arms which appear bluer. At the point of division between the two forks in Figure 1.5, the upper branch depicts the structure of spiral galaxies where the spirals emanate from the central bulge of the galaxy and the spirals become less and less tightly wound as the sequence progresses. These are S type galaxies and designated Sa, Sb, Sc as the sequence moves to the right. The lower branch depicts the structure of barred galaxies with the nomenclature SBa, SBb, SBc as the sequence progresses.

Hubble himself recognised shortcomings in his classification method, which did not adequately address irregular galaxies, for example, but the classification is still in use, modified and improved principally by de Vaucouleurs in the 1950s [de Vaucouleurs, 1959]. One of the principal revisions made by de Vaucouleurs was the addition of the $r-$ and $s-$ type sub-division for barred spiral galaxies, which recognises two different attachments of the spirals to the central bar. In $s-$ types, the spirals attach directly to the ends of the bar, such as SBb in Figure 1.5, whereas in $r-$ type galaxies the spirals attach to a ring-like structure around the bar, such as SBa in Figure 1.5. Hodge [1966] depicts this as a classification volume showing gross galaxy types along the central axis from elliptical (E) to Magellanic spirals (Sm) and (Im). Barred and non-barred galaxies are depicted on opposite sides of the volume, and the sub-divisions $s-$ and $r-$ in quadrature to them, as in the lower panel of Figure 1.5.

A good discussion of the development of the classification is given in 'Classification and Stellar Content of Galaxies' in Sandage et al. [1975], Chapter 1. It is worth just noting at this point the remarkable success of the Galaxy Zoo citizen science project, which requests members of the general public to classify SDSS images presented online. It uses the basic galactic types of Hubble and de Vaucouleurs and has released

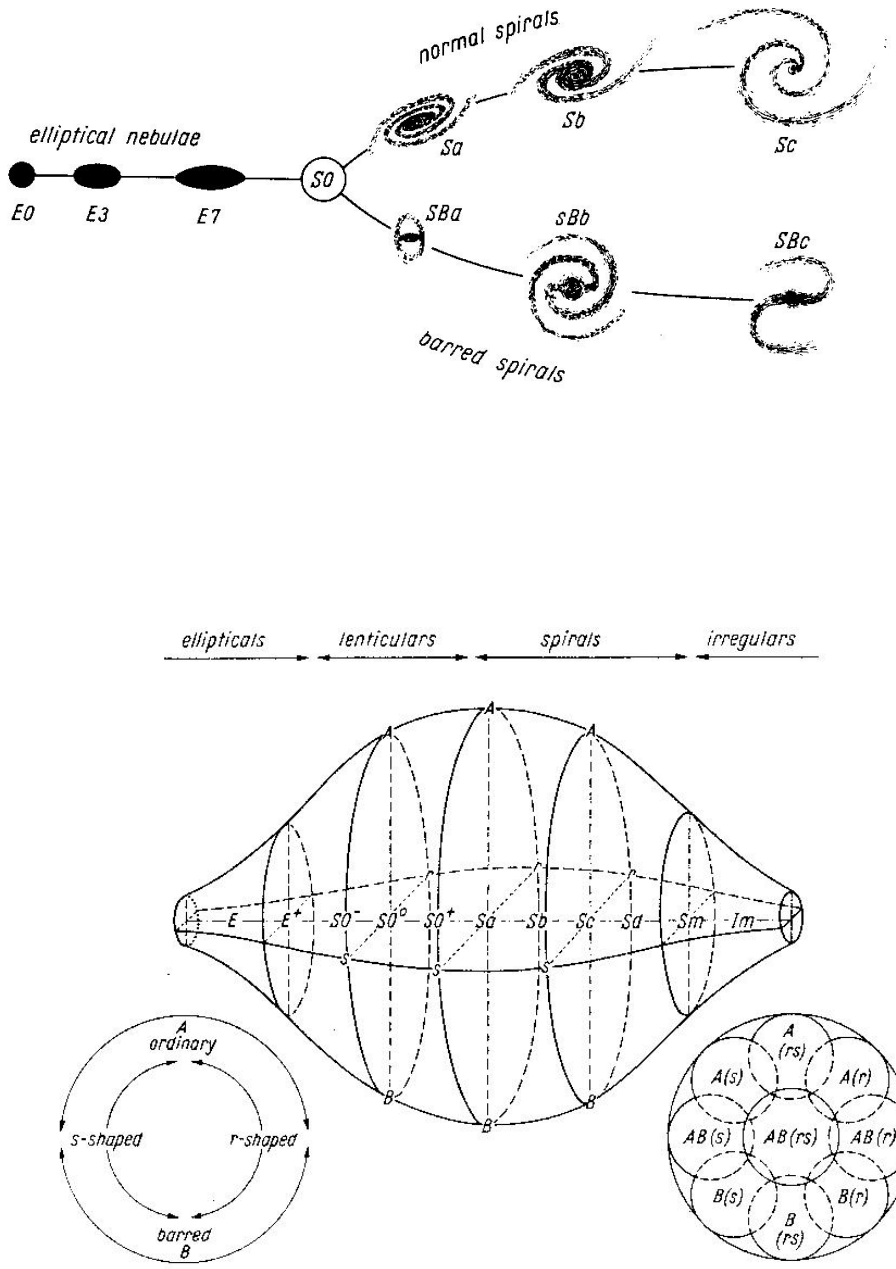

Figure 1.5.: Galaxy Classification
Upper panel: Hubble 'Tuning Fork' of galaxy classification [Hubble, 1936].
Lower Panel: Hodge's 1966 depiction [Hodge, 1966] of the De Vaucouleurs 1959 revisions [de Vaucouleurs, 1959].

its second morphological classification of over 304,122 galaxies [Willett et al., 2013].

1.3.2. Galaxy types

Characteristics of the galaxy types are summarised below:

- *Elliptical galaxies.* Elliptical galaxies tend to contain old stars and are red in colour. There contain little gas at present and there is little though some star formation in some ellipticals [Rogers et al., 2009]. In relaxed systems, the system is pressure supported by the random motion of the stars, and the velocity dispersion of the stars, σ, is empirically linked to the luminosity, L, of the galaxy by the Faber-Jackson relation, $L \propto \sigma^4$. Empirically, this can be quantified as follows:

  $$\frac{L_V}{2 \times 10^{10} L_\odot} \approx \left(\frac{\sigma}{200 \text{ km s}^{-1}}\right)^4 \text{ (in the } V-\text{band) [Sparke and Gallagher, 2007]}$$

  $$\frac{L_R}{1 \times 10^{10} L_\odot} \approx \left(\frac{\sigma}{150 \text{ km s}^{-1}}\right)^4 \text{ (in the } R-\text{band) [Binney and Tremaine, 2008]}$$

  Ellipticals have a surface brightness which is high in the centre of the sky-projected image and drops off exponentially with radius. A common surface brightness profile is the Sérsic law, $I_m(R) = I(0)\exp(-kR^{1/m})$, where $I_m(R)$ is the surface brightness at radius R and $I(0)$ is the surface brightness at the centre. k is a constant of proportionality and m is the Sérsic Index which is proportional to the luminosity of the galaxy ranging from $m \simeq 6$ for bright galaxies to $m \simeq 2$ for dim galaxies [Binney and Tremaine, 2008].

  The sizes of ellipticals, when plotted in 3 dimensional space with surface brightness and central velocity dispersion, results in them lying on or close to a *fundamental plane*, which is formulated empirically as $R_e \propto \sigma^{1.2} I_e^{-0.8}$. R_e is the effective half light radius, σ is the velocity dispersion within R_e, and I_e is the surface brightness at R_e. High mass galaxies have a correspondingly high velocity dispersion and also tend to be luminous. For large ellipticals it is found that there is a strong correlation between mass/light ratio and velocity dispersion [Binney and Tremaine, 2008].

- *Spiral galaxies.* Spiral galaxies host a central pressure-supported bulge surrounded by spiral arms of gas, dust and stars, which are rotationally supported, attached at one end to the bulge. They typically have a spherical halo of old stars and are believed to lie inside a much larger dark matter halo which

influences their rotation speed. The bulges of spiral galaxies tend to contain mainly late type dwarf stars (K and M types on the main sequence, small, red and abundant) while the spiral arms tend to have more young main sequence stars, whose light is dominated by massive, hot, blue and luminous O, B, A stars). As a result, the bulge tends to be redder than the spiral arms, which are bluer as a result of stars forming.

As for elliptical galaxies, the kinematics of a spiral galaxy can be predicted from its luminosity, following the Tully-Fisher relationship, $L \propto V_{\rm max}^{\alpha}$. This relates the total luminosity with the maximum rotation speed of the disk, where $\alpha \sim 4$. Empirically, $\alpha \approx 4$ in the $I-$band, where it has been found that:

$$\frac{L_I}{4 \times 10^{10} L_{I,\odot}} \approx \left(\frac{V_{\rm max}}{200 \text{ km s}^{-1}} \right)^4 \text{ (in the } I-\text{band) [Sparke and Gallagher, 2007]} \tag{1.2}$$

- *Barred spiral galaxies.* The two largest galaxies in the LG both are barred spiral galaxies, of mass $\sim 10^{12}$ $M_{\odot}$ [Evans and Wilkinson, 2000]. They comprise a large central bulge from which a bar extends outward on both sides. Spiral arms are attached to the bar or to a ring encircling the ends of the bar.

  The bulge and bar of barred spiral galaxies are usually old and red. They are in general not star forming. The spiral arms however contain gas from which stars are formed, hence like spiral galaxies, the arms of the barred spiral galaxies tend to be blue in colour.

  The Milky Way (MW) is a barred spiral galaxy (S(B)bc), lying between the b and c classifications [McConnachie, 2012]. The MW is considered to comprise a bulge of old stars, a halo of old stars, a thin disk containing spiral arms with star forming regions and young stars, and a thick disk of stars which have a lower metallicity than those in the thin disk and are believed to be a separate population.

  Andromeda (M31) is a spiral galaxy (Sb), McConnachie [2012]. In de Vaucouleurs classification it is SA(s)b, de Vaucouleurs et al. [1991]. This classification can be seen in the lower panel of Figure 1.5.

- *Irregular (Irr) galaxies.* Extending beyond the spiral branches of the Hubble Tuning fork, where the spiral arms have become indistinct, lie classes of galaxies which appear to have irregular morphologies [Binney and Tremaine,

2008]. They are gas rich so their luminosity is dominated by hot young stars and HII regions, but the stars are not distributed regularly in spiral arms, but in a more random fashion, which results in an irregular appearance [Binney and Tremaine, 2008]. Typical of these irregular galaxies are the Large and Small Magellanic Clouds, LMC and SMC, although the SMC is given the epithet 'dwarf' galaxy. The Large Magellanic Cloud (LMC) is an Irregular (Irr) galaxy [McConnachie, 2012], or SB(s)m in de Vaucouleurs classification [de Vaucouleurs et al., 1991]. It has an absolute magnitude $M_V = -18.1$ [McConnachie, 2012]. The Small Magellanic Cloud (SMC) is a dwarf irregular (dIrr), SB(s)m pec in de Vaucouleurs classification [de Vaucouleurs et al., 1991]) with an absolute magnitude $M_V = -16.8$ [McConnachie, 2012].

Irregular galaxies are also observed which are the result of galaxy collision or merging, where tidal interaction has disrupted the stellar distribution of spiral or elliptical galaxies, or where streams of stars from the galaxies have been ejected, or where intense bursts of star formation have occurred, distorting the apparent stellar distribution [Binney and Tremaine, 2008]. Major mergers tend to significantly disturb both galaxies and throw out wispy trails of stars, gas and dust (e.g. Antenna galaxy: NGC 4038/NGC 4039). Minor mergers tend to increase star formation in the larger galaxy and completely tidally strip the smaller galaxy transferring its stars, gas and dust into a complex substructure (streams, rings, thick disk) within the galaxy, its precise fate being determined by the initial conditions of the merger [Binney and Tremaine [2008] and references therein]. In the LG, the Magellanic Bridge as an example of tidal disruption involving the dwarf irregular galaxies LMC and SMC. It is seen as a bridge of stars connecting the two galaxies and is believed to have been formed after "collision" of the galaxies [Bagheri et al., 2013].

- *Dwarf galaxies.* Dwarf galaxies typically have masses between 10^6 and 10^8 $M_\odot$ [McConnachie, 2012]. A galaxy is considered 'dwarf' if its absolute magnitude, M_V, is fainter than -18 [Grebel et al., 2003, McConnachie, 2012]. They can be classified as dwarf ellipticals (dE), dwarf spheroidals (dSph) and dwarf irregulars (dIrr). dEs and dSphs are elliptical in shape but dSphs are generally smaller, at around 10^6 $M_\odot$. dEs have generally a greater luminosity than dSphs. Recently a number of ultra-faint dwarfs have been discovered, as discussed in §1.2.2, with extremely low luminosity. Both have a low gas content and show little sign of star formation. Curiously, the velocity dispersions of the stellar content seems to stay quite high (tens of km s^{-1}) even though the

luminosity reduces. Hence the smaller the galaxy appears to be, the greater its mass-to-light ratio. In the LG, dEs are often bound to M31, but dSphs appear to be more generally distributed.

Dwarf irregulars tend to lie in the outer half of the LG and show signs of disruption. They often have sufficient gas content to permit star formation. In many cases, their mass has not been fully estimated, although components of their matter content, for example the gas content in some cases, have.

- *cD galaxies.* cD galaxies are elliptical galaxies with a very bright central surface brightness. They are often surrounded by other bright elliptical galaxies forming clusters. They have a steep fall off in surface brightness with radius [Binney and Merrifield, 1998, Binney and Tremaine, 2008].

  Whereas in normal ellipticals, the velocity dispersion tends to fall with increasing radius from the galaxy centre, in cD galaxies the velocity dispersion tends to rise [Binney and Merrifield, 1998], implying that they are part of a much larger cluster halo. In this event, the term brightest cluster galaxy (BCG) is often used to describe them [Binney and Tremaine, 2008].

1.4. Genesis of this work

This work was an opportunity to study the resolved, intermediate age stellar population of NGC 6822 from spectra already obtained by Sibbons et al. [2015]. NGC 6822 is a dwarf irregular galaxy in the southern hemisphere too faint to be seen with the naked eye[4]. An image of NGC 6822 is shown in Figure 1.6. While originally intended to be an introduction into the techniques of spectral analysis for radial velocity measurement, it was quickly found that good science could be extracted from the spectra even though the observations were not optimised for that purpose.

The spectra used were obtained by Sibbons et al. [2015] using the AAOmega spectrograph over two nights, 30 and 31 August 2011, at the Australian Astronomical Observatory, at Siding Spring, New South Wales. The instrument can measure up to 400 objects over a range of bands in the visible and infra-red spectral regions, using optical fibres mounted on a field plate placed in the focal plane of the telescope. The fibres are led to the spectrograph and are arranged into a pseudo-slit by vertically stacking the fibres at its input. Light from the fibres was split into two

[4]It has an absolute magnitude of $M_B - 15.85$ [Hodge et al., 1991], and an apparent magnitude of $m = 9.31$ (NED), and $m_{\rm V} = 8.1 \pm 0.2$, $m_{\rm J} = 7.483 \pm 0.025$, $m_{\rm H} = 6.916 \pm 0.03$, $m_{\rm K} = 6.724 \pm 0.045$ (SIMBAD).

beams, a red beam and a blue beam, by a dichroic filter, at 5700 Å [5]. Each beam was passed through a transmission diffraction grating before reaching a ccd camera. Each camera has an array of 4096 × 2048 ccd pixels and measures the photon counts in each pixel. The spectrum is dispersed along the 2048 pixel axis.

AAOmega has a range of diffraction gratings for various purposes and the gratings used by Sibbons et al. [2015], 385R with the red camera and 580V with the blue camera, were of the widest spectral range which was desirable for the spectral classification work undertaken therein. Consequently they were also of the lowest resolution in the AAOmega grating set, with resolving powers of $R = 1300$. The raw data had been reduced to science data through the data pipeline and issued as a .fits file. Each .fits file contains a header and the signal level for each pixel. When corrected for bias and gain, the signal level is proportional to the photon count and also contains some noise.

The selection of objects for spectroscopy was made by Sibbons et al. [2015] to validate a photometric AGB classification study. Sibbons et al. [2015] obtained the spectra over a waveband from 3700 Å to 8800 Å, but in this study, radial velocities were measured with the spectra from the red camera only, 5700 Å to 8800 Å, because of inadequate signal to noise ratio (*SNR*) in the blue spectra. A number of fibres were used as sky fibres and guide fibres, others were not used and parked. The spectra of 4 other objects were not used, so the total number spectra available for analysis was 323. Of this total, the sample contained 96 carbon stars within the 4 kpc of the galactic centre, which became the targets for this study.

The spectra were observed for only 25 minutes yielding a rather poor *SNR*. Although the spectral resolution and *SNR* are not ideal for radial velocity measurements and led to large individual errors, there is a sufficiently large number of objects in the sample to reduce the standard error in the mean to an acceptably low value.

Having set out the background to galaxy formation in a cosmological context and introduced the spectral data and analysis approach which was used to study NGC 6822, I now present the details of the measurement of individual stellar velocities in the galaxy and provide its radial velocity, its rotation velocity and the orientation of its rotation axis. This work, as presented in §2, has been submitted for publication [Thompson et al., 2016] [in prep].

[5] another is available at 6700 Å

Figure 1.6.: NGC 6822: Barnard's Galaxy showing the irregular shape of the galaxy. The central bulge is visible, and also a faint halo. The galaxy also has a prominent HI gas disk which is not visible in this image. The image dimensions are 35 arcmins × 34 arcmins Image credit: European Southern Observatory (ESO)

2. Stellar Kinematics in NGC 6822

2.1. Structure of NGC 6822

NGC 6822 (Barnard's galaxy) is a relatively bright and well studied dwarf irregular galaxy. It lies within the Local Group (LG), quite close to the Milky Way, and is the third nearest dwarf irregular galaxy after the Large and Small Magellanic Clouds. It was the first object to be shown to lie outside the Milky Way [Hubble, 1925]. It has no known close companions and lies in a region relatively devoid of other galaxies [de Blok and Walter, 2000]. Despite its apparent isolation, there is some evidence of tidal interaction and a burst of star formation $100 - 200$ Myr ago [de Blok and Walter [2000] and references therein].

The location of NGC 6822 has a range of published values for right ascension (α) and declination (δ)[1], but for the purposes of this paper, I use $\alpha = 19^{\mathrm{h}}44^{\mathrm{m}}56^{\mathrm{s}}$, $\delta = -14°48'06''$ (J2000). This is at the centre of a 3 deg^2 field used by Sibbons et al. [2012, 2015] and is adopted here for consistency, since this study uses spectra drawn from their sample.

The galactic distance is variously reported to lie between 450 to 500 kpc. For the purposes of this paper, its distance is not important, but where I do use it, I again adopt the same value as Sibbons et al. [2012, 2015], 490 ± 40 kpc, for consistency with that work. Sibbons et al. [2012, 2015] also quotes a distance modulus for NGC 6822 of $(m-M)_0 = 23.45 \pm 0.15$ ($\approx 490 \pm 34$ kpc). In recent years, papers have been published which have provided new distance moduli using Cepheid variables, from which the distance and error can be readily derived. Many of these re-estimates have reduced the radial distance to NGC 6822 by about 10% from the value used herein. The distance modulus derived by Gieren et al. [2006] is $(m - M)_0 = 23.312 \pm 0.021$

[1] SIMBAD [Skrutskie et al., 2006]: $\alpha = 19^{\mathrm{h}}44^{\mathrm{m}}56.199^{\mathrm{s}}$, $\delta = -14°47'51.29''$ (J2000).
NED [2010SEG..C.....0C]: $\alpha = 19^{\mathrm{h}}44^{\mathrm{m}}57.7^{\mathrm{s}}$, $\delta = -14°48'12''$ (J2000).
McConnachie [2012]: $\alpha = 19^{\mathrm{h}}44^{\mathrm{m}}56.6^{\mathrm{s}}$, $\delta = -14°47'21''$ (J2000).

($\approx 460 \pm 4.4$ kpc). Feast et al. [2012] gives $(m - M)_0 = 23.40 \pm 0.05$[2] ($\approx 479 \pm 11$ kpc), and Rich et al. [2014] gives $(m-M)_0 = 23.38 \pm 0.02_{\rm stat} \pm 0.04_{\rm sys}$ ($\approx 474 \pm 13_{\rm tot}$ kpc). For the formulae used to determine the distance errors from the distance moduli, see Appendix A.

Morphologically, NGC 6822 has three components: a gaseous disk of HI (Figure 2.1, left hand panel), an outer spheroid of stars (Figure 2.1, right hand panel) and a small central core of young stars [Hodge et al., 1991]. Its HI content has been studied by de Blok and Walter [2000] and its the stellar content, especially Red Giant Branch (RGB) and Asymptotic Giant Branch (AGB) stars, by Letarte et al. [2002], Battinelli et al. [2006], Demers et al. [2006] and Sibbons et al. [2012, 2015]. The HI gas disk appears to lie at a position angle (PA) of $\sim 130°$ when observed from tip to tip [de Blok and Walter, 2000]. However, it also appears to twist and in Weldrake et al. [2003], the PA is stated as $\sim 110°$, which is closer to the major axis of the central part of the disk, as shown in Figure 2.1 (left hand panel). Letarte et al. [2002] shows that carbon stars lie well outside the HI disc and Demers et al. [2006] and Battinelli et al. [2006] show that the isophotes of RGBs of NGC 6822 are also elliptical, where the major axis PA changes from $\sim 65°$ (outermost contour) to $\sim 80°$ (innermost contour), as shown in Figure 2.1 (right hand panel).

Much of the published velocity data for NGC 6822 has been derived from the HI gas content of NGC 6822 using the 21 cm line [Koribalski et al., 2004, Weldrake et al., 2003]. Koribalski et al. [2004] measures a heliocentric radial velocity, $V_{\rm helio}$, of -57 ± 2 km s^{-1} for NGC 6822 from its HIPASS spectrum, and this now a commonly cited value. Mateo [1998] and sources therein, also provide $V_{\rm helio}$ based on the HI component, $V_{\odot,\rm radio}$ of -54 ± 6 km s^{-1}, and Weldrake et al. [2003] similarly provides a HI derived systemic (radial) velocity[3] in the range -53.3 km s^{-1} to -54.7 km s^{-1} at the centre of the HI gas.

Rotation of the gas disk has also been measured at 21 cm. Mateo [1998] provides a value for the rotation of the HI disk, $v_{\rm rot,ISM}$, of 47 ± 3 km s^{-1}, and Weldrake et al. [2003] shows that the velocity of the HI disk ranges from -100 km s^{-1} at the NW extreme (blue-shifted) to $+10$ km s^{-1} at the SE extreme (red-shifted). McConnachie [2012] quotes a peak observed rotation speed of 47 ± 2.0 km s^{-1}, uncorrected for inclination or asymmetric drift, citing Koribalski et al. [2004] and Weldrake et al. [2003].

However, with regard to the stellar kinematics of NGC 6822, there are published

[2]Feast et al. [2012] does not claim any precision with the error value, owing to the difficulty in measuring the true uncertainty in the value of the distance modulus.

[3]I assume all velocities quoted in Weldrake et al. [2003] are corrected to heliocentric

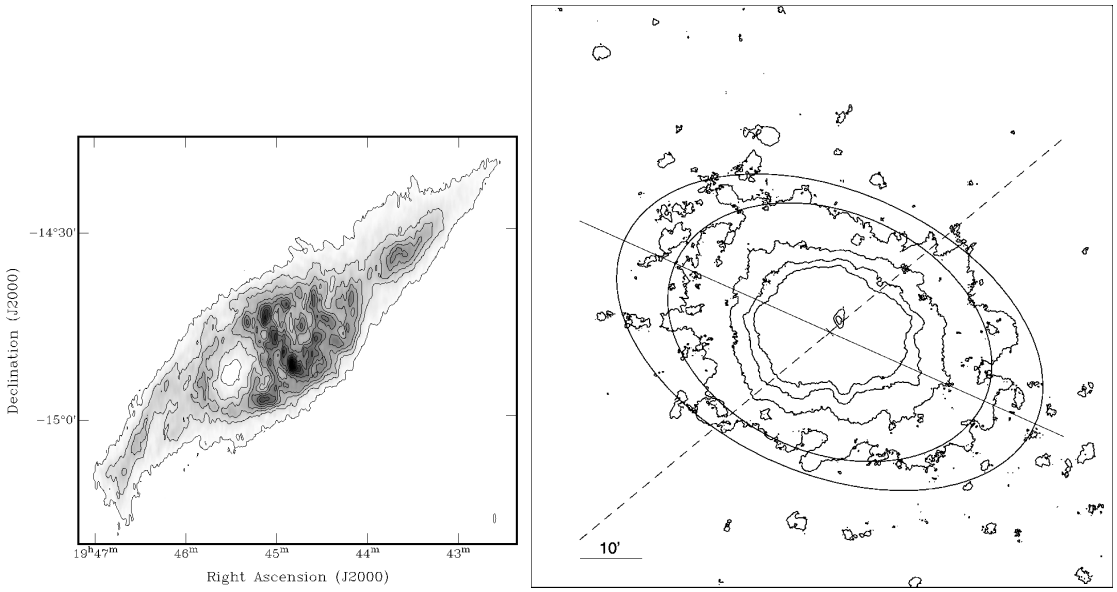

Figure 2.1.: Gas and stellar morphology of NGC 6822

Left hand panel, HI isodensity curves of NGC 6822 [de Blok and Walter, 2000]. The HI curves exhibit a disk-like structure, which is twisted with a major axis *PA* from $\sim 110°$ to $\sim 130°$.

Right hand panel, RGB stellar isodensity profiles [Demers et al., 2006]. The RGB profiles exhibit elliptical contours, where the major axis *PA* changes from $\sim 65°$ (outermost contour) to $\sim 80°$ (innermost contour).

The solid line in the right hand panel lies at 65° and the dashed line lies 130°. The panels are shown to approximately the same scale and orientation.

Table 2.1.: Published Distance and Kinematic Data for NGC 6822

Source:	Dist. kpc	Vrad(stellar) km/s	Vrad(HI) km/s	Vrot(stellar) km/s	Vrot(HI) km/s
Mateo [1998] +	490 ± 40	-53 ± 4	-54 ± 6	...	47 ± 3
Weldrake et al. [2003]	490 ± 40	...	-53.3 to -54.7	...	PA $109°$ to $150°$
Koribalski et al. [2004]	...	...	-57 ± 2 *	...	...
Demers et al. [2006]	...	$+10$ to -70	...	PA $63 - 67°$	PA$\sim 130°$
Gieren et al. [2006]	460 ± 4.4**	...	...	...	...
Feast et al. [2012]	479 ± 11**	...	...	...	...
McConnachie [2012]	459 ± 17	...	...	...	47.0 ± 2.0
Rich et al. [2014]	474 ± 13**	...	...	...	...
Kirby et al. [2014]	...	-54.5 ± 1.7	...	...	...

* HIPASS spectra measured at midpoint between the 50% peak flux points in km s^{-1}.
** Calculated from distance moduli using formula in Appendix A.

data for $V_{\rm helio}$, but little regarding stellar rotation. Mateo [1998] and references therein, provide a value of $V_{\rm helio}$ based on optical measurements[4] of $V_{\odot,\rm opt} = -53 \pm 4$ km s^{-1}. Kirby et al. [2014] studies the kinematics of seven isolated dwarf galaxies in the LG, including NGC 6822, from the radial velocities of red giant stars, finding a mean heliocentric radial velocity for NGC 6822, $\langle V_{\rm helio} \rangle$, of -54.5 ± 1.7 km s^{-1} and a dynamical mass over the half light radius of $M_{1/2} = 2.4 \pm 0.3 \times 10^8\ M_\odot$. Table 2.1 summarises these and other published data.

Most references to stellar rotation cite Demers et al. [2006], who in a separate paper [Demers and Battinelli, 2007] suggest that radial velocities of individual NGC 6822 giants might give some insight into rotation of the stellar population. In Demers et al. [2006], the radial velocities for 110 carbon stars, taken from a sample in Letarte et al. [2002] and lying within $15'$ (~ 2.1 kpc) of the HI major axis, are measured, although the individual stellar measurements are not published. A variation in residual velocity along the major axis of the outermost RGB isophote is interpreted to be a signature of rotation about the minor axis. As a result, the paper suggests that the carbon stars appear to rotate about an axis roughly perpendicular to the rotation axis of the HI disk, resembling a Polar Ring Galaxy (PRG). It would be extraordinarily useful if NGC 6822 is a PRG, since they are very rare. The Sloan Polar-Ring Catalogue (SPRC), which uses images from the Sloan Digital Sky Survey, includes only 6 confirmed PRGs from a total of just 275 candidates. Discovery of a nearby PRG would present a remarkable opportunity to study these galactic types at close hand.

[4] Assumed to be integrated light, but Mateo [1998] does not specify

Kirby et al. [2014] checked for signs of rotation in their sample of 7 dwarf galaxies, and found that only the Pegasus dwarf irregular showed obvious signs. For NGC 6822, they refer to the findings of Demers et al. [2006]. They comment that while a rotation of the order of ~ 10 km s^{-1} is possible in NGC 6822, their data were too highly obscured by velocity dispersions to be certain.

The published studies of the galaxy's stellar rotation are complemented by other studies of the motion of globular clusters [Veljanoski et al., 2015] and planetary nebulae [Flores-Durán et al., 2014]. Veljanoski et al. [2015] studies the globular cluster (GC) system of NGC 6822, in which 8 GCs are presently identified (see Table 1 therein). The radial velocities of 6 of the GCs are given and $\langle V_{\rm helio} \rangle$ is deduced to be between -59 and -60 km s^{-1}. The spatial distribution of the GCs in their data is rather linear and lies approximately parallel to the major axis of the AGB isophotes. Three possible dynamical models are considered:

- 'Disk model', in which the rotation axes are similar to that suggested by Demers et al. [2006]. The resulting rotation rate is 12 ± 10 km s^{-1}.

- 'Cigar model', where the cluster system shares the same rotation axis as the HI disk. In this case the rotation rate is determined to be 56 ± 31 km s^{-1}.

- A scenario where there is no net rotation by disconnecting any relationship between the gas disk and the stellar component.

In none of these models are they able to independently determine the *PA* of the rotation axis owing to the small number of objects in their sample of GCs, but their preferred case is the 'Disk model', owing to its low rotation rate. They argue that in the case of the 'Cigar model' the rotation is too high, and would cause the sample to flatten into a disk which they do not observe.

In Flores-Durán et al. [2014], the motion of 10 planetary nebulae (PNe) in the galaxy are studied. PNe are the evolutionary stage reached by AGBs after the end of their lives, and may thus provide complementary kinematic information of the galaxy. Flores-Durán et al. [2014] compute the mean $\langle V_{\rm helio} \rangle$ of the PNe to be -57.8 km s^{-1}. They compare their result with a C-star mean $V_{\rm helio}$ of -32.9 km s^{-1} (not cited), and the mean $V_{\rm helio}$ of 4 GCs of -88.3 km s^{-1} [Hwang et al., 2014] and deduce the PNe, C-stars and clusters belong to different dynamical systems. Referring to Demers et al. [2006], they also infer that different dynamical systems are involved for the gas disk and the stars, but with so few PNe, they are unable to reliably fit the radial velocity data to either system.

The Mateo [1998] census contains radio and optical $V_{\rm helio}$ values for NGC 6822 and rotation velocities of the HI gas. It does not provide any velocity for stellar rotation. In recent years, McConnachie [2012] has prepared a new census including over 100 galaxies within 3 Mpc of the LG barycentre, of which nearly 80 galaxies lie in the LG. This census includes data for recently discovered galaxies and recent measurement of key parameters. For NGC 6822, McConnachie [2012] and references therein give values for $V_{\rm helio}$, and for gas rotation but again none for stellar rotation.

This study provides the results of a new study of the kinematics of NGC 6822, based on the spectra of individual stars obtained by Sibbons et al. [2015] in 2011. It follows studies by Sibbons et al. [2012, 2015]) which classify stars, photometrically and spectroscopically, from a set taken from the catalogue of Letarte et al. [2002]. These studies were able to distinguish C-type and M-type AGBs from other types, so that although Demers and Battinelli [2007] cautions that the separation of carbon stars associated with NGC 6822 from foreground Galactic dwarfs might be difficult, my present study has the advantage of using the spectra of stars which have already been classified as carbon stars in NGC 6822, with a high degree of confidence.

The radial velocities of well over 100 stars within a 4 kpc radius of the centre of NGC 6822, (the *inner region*), and well over 100 stars outside the 4 kpc radius, (the *outer region*), are measured and reported. In the inner region many of these stars are classified as carbon stars and are expected to be associated with the galaxy [Sibbons et al., 2015]. In the outer region, most of the stars are expected to be foreground Milky Way stars [Sibbons et al., 2012, 2015].

Based on the aggregated sample of carbon stars in the inner region, a value for the heliocentric radial velocity of NGC 6822 is derived. The kinematics of individual stars in the sample indicate that they belong to the same population, supporting Sibbons et al. [2015]. Moreover, the radial velocity measurements are accurate enough to reveal rotation of the stellar component about an axis through the centre of the galaxy, and to derive its rotational speed and a new *PA* for the axis of rotation. In §2.2, I discuss the data set, its origins and its limitations. In §2.3, I discuss the method used to analyse the data set including the selection of objects for analysis. In §2.4, I discuss the results and in §2.5, I draw conclusions.

Structure of NGC 6822 in contrast to MW and M31

NGC 6822 comprises late type stars and little gas in the central core, a disk of gas and dust with star formation causing it to appear bluer in this region and a halo of older intermediate stars including red giant branch stars (RGBs) and asymptotic

branch stars (AGBs).

Its central core has been studied by Hodge et al. [1991]. It appears to be elliptical in shape with a major axis rotated to a PA$\sim 10°$. Its HI content has been studied by de Blok and Walter [2000] and its the stellar content, especially Red Giant Branch (RGB) and Asymptotic Giant Branch (AGB) stars, by Letarte et al. [2002], Battinelli et al. [2006], Demers et al. [2006] and Sibbons et al. [2012, 2015]. Letarte et al. [2002] showed that carbon stars lie well outside the HI disc. The HI gas disk appears to lie at a position angle (PA) of $\sim 130°$ when observed from tip to tip. However, it also appears to twist and in Weldrake et al. [2003], the PA is stated as $\sim 110°$, which is closer to the major axis of the central part of the disk. According to Demers et al. [2006] and Battinelli et al. [2006], the C-type stars and RGBs of NGC 6822 form ellipsoids as shown in right hand panel of Figure 2.1, where the major axis PA changes from $\sim 65°$ (outermost contour) to $\sim 80°$ (innermost contour).

The orientations of the gas disk and the stellar halo whose isophotal major axes are $\approx 90°$ apart, and the stellar radial velocity dispersion about putative rotation axes, led Demers et al. [2006] to conclude that the halo and disk rotate about axes $\approx 90°$ apart, thus suggesting an unusual type of galaxy, the polar ring galaxy. However, this study does not support this analysis.

2.2. Observations and Data

This study uses asymptotic giant branch (AGB) stars as tracers of kinematic properties of the galaxy. AGB stars are amongst the brightest stars in an intermediate-age or old stellar population and can be resolved in galaxies beyond the Milky Way, making it possible to study them individually. They are intermediate age stars of $2 - 8M_{\odot}$ which have evolved from the main sequence and through the red giant branch (RGB) stages of stellar evolution. They have swelled to a large radius and are thus bright with a relatively low temperature.

AGBs tend to divide into those with oxygen rich atmospheres (M-types), and those with carbon rich atmospheres (C-types or carbon stars). Their surface temperatures, $T_{\rm eff}$, range from as low as 2200 K [Matthews et al., 2015] for old stars near the end of their lives up to ~ 4000 K for intermediate age stars[5]. The continuum peaks at wavelengths in the near infra red, with increasing brightness through the I, J, H and K bands.

[5]In van Belle et al. [2013], 12 carbon stars are found to be in a range of $T_{\rm eff} = 2381 \pm 81$ K to 3884 ± 161 K, with a mean at 2800 ± 270 K.

The spectrum of a typical AGB contains a number of absorption features, predominantly broad TiO bands in M-type AGBs, broad CN bands in C-type AGBs. The $I-$band spectral region also contains the Ca II triplet lines in both types of AGB. The Ca II triplet lines are ideal for measuring radial velocities as they are narrow atomic features lying where the continuum is relatively strong, producing absorption features ideally suited to radial measurement. In this study, I use the spectra of carbon rich AGBs classified by Sibbons et al. [2015] as follows: confirmed C-type stars (C); tentative C-type stars (C:), confirmed C-type stars which exhibit Hα and sometimes [S II] and [N II] emission (Ce) and tentative C-type stars which similarly exhibit emission (Ce:).

Wide band, low resolution spectra for 323 target objects, out to $\approx$ 8 kpc from the galactic centre, were obtained using the AAOmega multifibre spectrograph and gratings 385R and 580V on 30 and 31 August 2011 [Sibbons et al., 2015]. This study uses the spectra from grating 385R only, which has a bandpass from 5687 Å to 8856 Å, covering the Ca II triplet, dispersed at 1.6 Å pixel^{-1}. A complete list of the objects is found in Appendix B, each with its spectroscopic classification [Sibbons et al., 2015]. Each object is identified by a number which corresponds to the fibre head covering the object, and throughout this paper, objects are referred to by their fibre number. The spectra were reduced by Dr L Sibbons to science frames, using the AAOmega pipeline. The spatial position of each object is plotted in Figure 2.2, which shows 135 objects in the inner region, and 188 objects in the outer region. Ninety eight black points and one red point show the positions of the C-type AGBs. The red point is the location of object #31 which was utilised in the processing of the data described later. Three black points located just outside the outermost isodensity profile were not used in the analysis, so the total number of carbon stars used is 96. Ellipses which reproduce the location and extent of the gas disk and outermost RGB isodensity profile of NGC 6822 are also plotted on Figure 2.2.

Figure 2.3 shows the spectra of a typical C-type AGB, object #31, for both observing nights. The upper panel shows the spectra measured by the red camera and shows the waveband containing the Ca II triplet shaded in grey. It is evident that the spectrum of 31 August has a higher photon count in the continuum than that of 30 August and this results in a correspondingly higher signal to noise ratio, *SNR*. This is generally the case for all spectra and led me to place more weight on the results for the night of 31 August. The lower panel expands the spectra over the Ca II triplet waveband indicating its absorption features at 8498.02 Å, 8542.09 Å and 8662.14 Å (rest).

Although the velocity resolution of the grating was rather low, $\approx$ 56 km s^{-1}

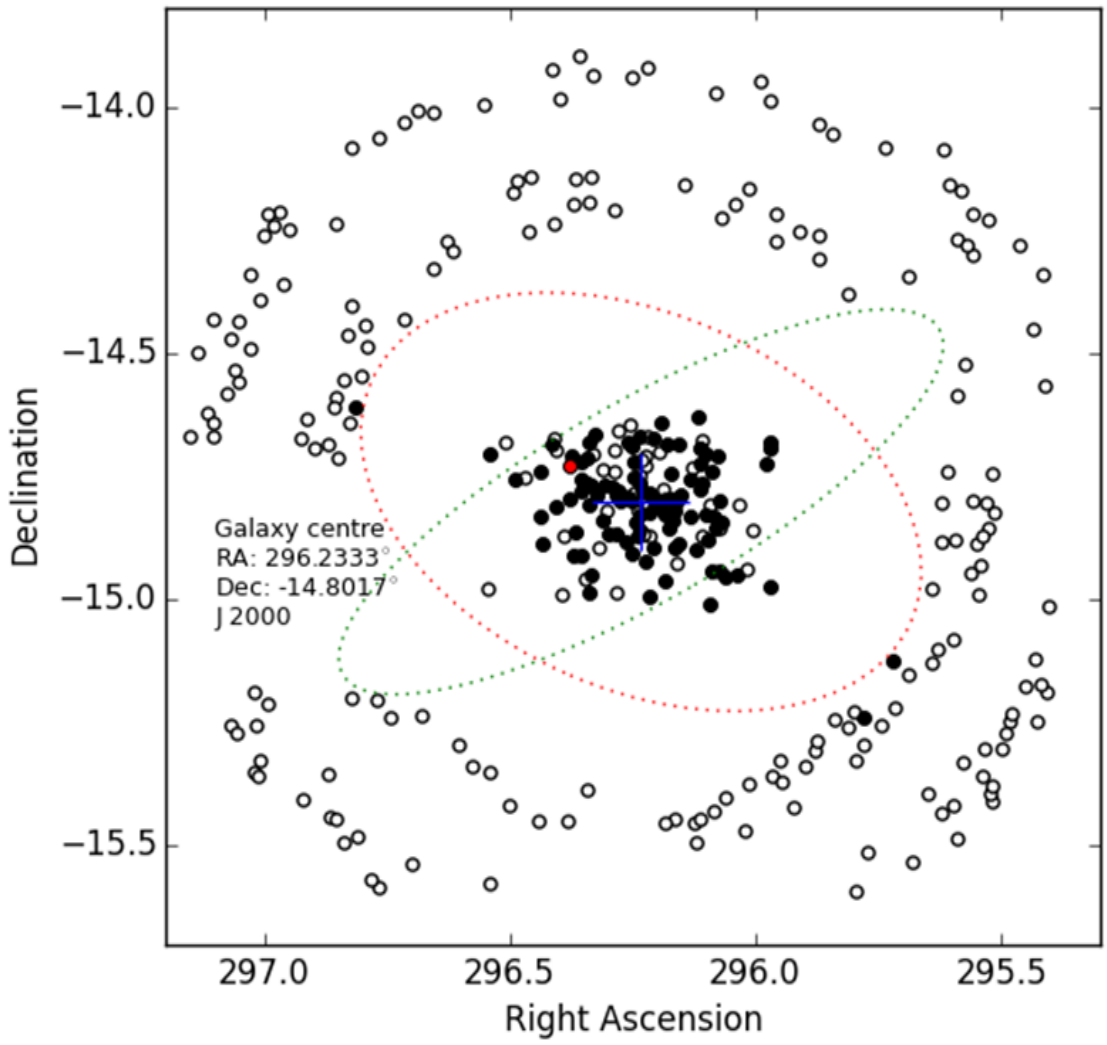

Figure 2.2.: Carbon star target locations
The locations of 323 NGC 6822 objects targeted by Sibbons et al. [2015], shown over 1.8° of the sky. The black points and red point show 99 objects classified by Sibbons et al. [2015] as C-type AGBs. The red point marks object #31, which is discussed in the text. The 3 outermost C-type AGBs lie more than 4 kpc from the galactic centre and were not used in the analysis. The open circles mark the remaining objects which are given other classifications. The dotted ellipses approximate the location and extent of the gas disk and outermost stellar isodensity profile shown in Figure 2.1. The concentric appearance of the outer objects is due to the layout of the fibres on the spectrograph field plate.

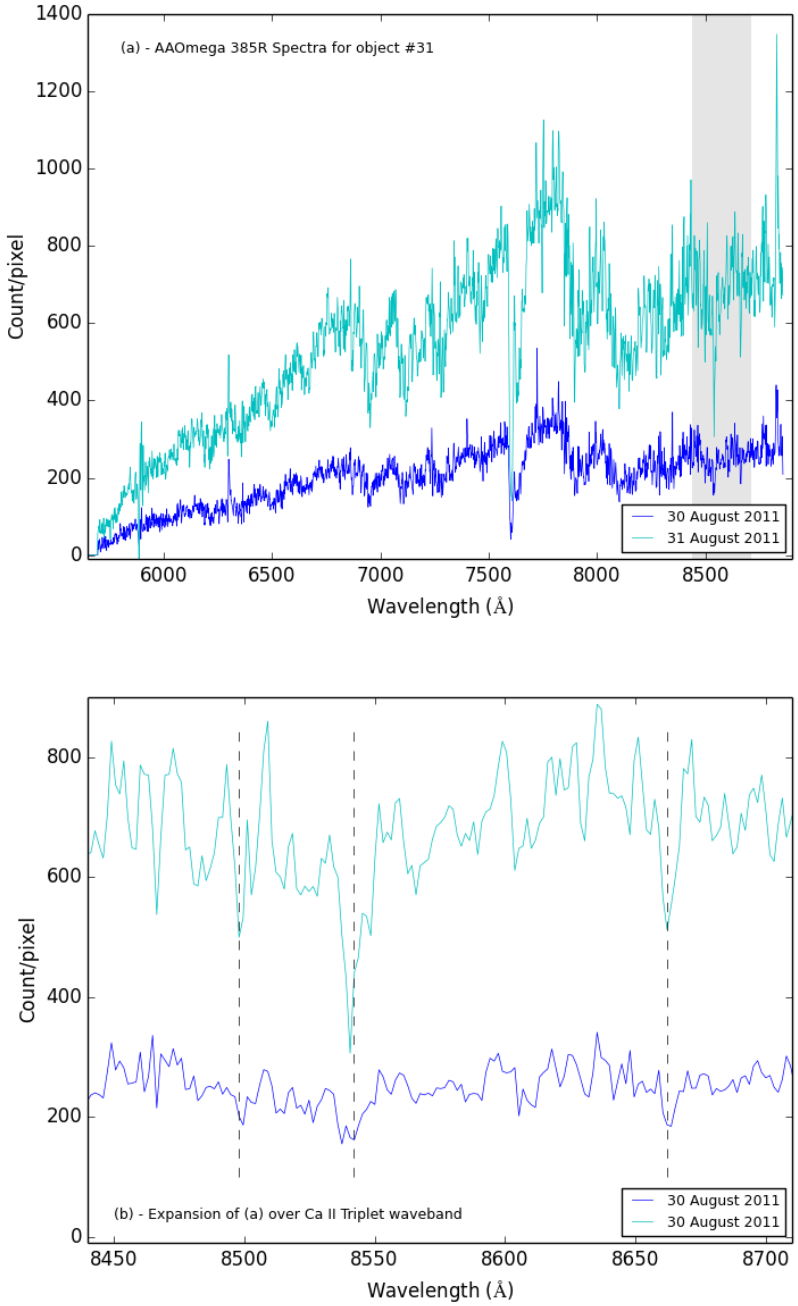

Figure 2.3.: Typical carbon star spectrum
Upper panel: Full red spectrum from AAOmega grating 385R for object # 31 on 30 and 31 August 2011. Object #31 is spectrally classified as a C-type star in Sibbons et al. [2015] and has CN absorption bands at 5730, 6206, 6332, 6478, 6631, 6925, 7088, 7259, 7437, 7876, 8026 Å which are characteristic of this type of star. The large absorption feature at 7594 Å is due to telluric O_2. The grey band indicates the waveband 8440Å to 8710Å containing the Ca II triplet features.
Lower panel: The same spectra expanded over the waveband 8440Å to 8710Å containing the Ca II triplet features used for radial velocity measurement. The centres of the Ca II triplet absorption lines are indicated by the vertical dashed lines at 8498.02 Å, 8542.09 Å, 8662.14 Å.

pixel^{-1} in the Ca II triplet waveband of interest, there were enough stars present in the sample to reduce the standard error in the mean velocity to an acceptably low value.

2.3. Radial Velocity Measurements

To measure relative velocities, I used the cross-correlation technique of Tonry and Davis [1979], as implemented in the IRAF[6] routine *fxcor*, star by star. For specific tasks, I also used other modules in IRAF as outlined in Appendix C.

2.3.1. Choice of spectral feature to cross correlate

In the measured spectra, absorption lines were examined to assess the best candidate for cross-correlation. The spectra exhibited features such as:

CN bands: these are characteristic of C-type objects with carbon rich atmospheres. Since molecular bands are much broader than atomic lines and are relatively featureless at the coarse resolution of the spectra, the velocity uncertainties are large.

TiO bands: these are characteristic of M-type objects with oxygen rich atmospheres. These present the same limitations as the CN bands.

Ca II triplet lines at 8498.02 Å, 8542.09 Å and 8662.14 Å: these occur in both C- and M- type AGBs, and the flux in the continuum of the cool AGB stars is close to its peak. The atomic lines are quite strong and narrow in many of the spectra.

The Na doublet (5895.92 Å and 5889.95 Å): these are common to many spectra but are contaminated by terrestrial sodium.

Hα absorption lines (6562.8 Å) are weak or absent in cool AGB stars. They were observed in a few cases [Sibbons et al., 2015], sometimes in emission.

Preliminary tests showed that the Ca II triplet absorption features gave the lowest velocity uncertainties, so it was chosen for use in the study. To ensure that the velocity was correctly calculated by *fxcor* throughout the study, all spectra were

[6]IRAF is distributed by the National Optical Astronomy Observatory, which is operated by the Association of Universities for Research in Astronomy (AURA) under a cooperative agreement with the National Science Foundation.

truncated to include only wavelengths inside the band (8440 Å to 8710 Å) which includes the Ca II triplet features.

2.3.2. Preparation of the template spectrum

The cross-correlation function in *fxcor* works best when the object and template spectra are well matched: ideally both of the same stellar type and both from the same stellar sample so that observing and instrumentation systematics are the same for both. Initially, the object on fibre #31 of the sample was chosen as a template for cross-correlation, as it is classified as a C type (carbon) star [Sibbons et al., 2012, 2015], has the best *SNR* for its type and has reasonably strong spectral features in the $I-$band. The object lies in the inner region of NGC 6822 and is shown by the red point in Figure 2.2. Although it is the brightest object in the sample, its spectra is still rather noisy in appearance, see Figure 2.3, and initial attempts to measure velocities using it as a template were limited by the noise in its spectrum. A decision was made to construct a composite spectrum to be used as the cross-correlation template, by co-adding the spectra of inner C-type targets.

The full list of 96 inner C-type targets, used to create the composite template, is shown in Table 2.2. Firstly, the bandwidth of the spectra was restricted to 8450 Å to 8700 Å to reduce spectral noise intruding from outside this waveband. Then, the relative velocity of each object was measured using *fxcor* with reference to object #31, for both observing nights. Each spectrum was corrected for this velocity using *dopcor* in IRAF. The corrected spectra were then co-added using IRAF's *scombine* routine to create a composite spectrum for each night. In a few cases, *fxcor* was not able to provide a valid result (see §2.3.4), so from the original 96 spectra, 90 went to make up the composite spectrum for the night of 30 August, and 93 for 31 August.

The composite spectrum for each night was then shifted to the rest frame by cross correlating, using *fxcor*, with a rest-frame spectrum of Arcturus[7] [Hinkle et al., 2000][8] similarly truncated to 8440 Å to 8710 Å as shown in Figure 2.4, and using *dopcor*. The Arcturus spectrum has higher *SNR* and higher resolution than the NGC 6822 sample. It exhibits well defined Ca II triplet absorption lines with typical Voigt profiles. Four iterations of correction were required to reduce the nightly templates to the rest frame with velocity residuals < 0.032 km s^{-1} (30 August 2011) and < 0.001 km s^{-1} (31 August 2011).

[7]Arcturus actually has a heliocentric radial velocity of -5.19 ± 0.04 km s^{-1} (SIMBAD), but the NOAO spectrum used is shifted to zero, which was confirmed using *splot*

[8]NOAO/AURA/NSF

Table 2.2.: List of inner field carbon stars

Class	Number of targets	Fibre Number
C	61	4, 6, 11, 12, 18, 23, 28, 31, 32, 38, 43, 48, 54, 68, 70, 76, 80, 85, 88 91, 94, 95, 98, 104, 112, 119, 122, 124, 136, 174, 191, 193, 198, 207 208, 210, 214, 220, 221, 226, 228, 229, 230, 235, 246, 257, 260, 262 267, 274, 287, 290, 292, 295, 305, 323, 326, 330, 334, 338, 398
C:	13	2, 3, 7, 10, 19, 20, 24, 53, 125, 204, 268, 322, 328
Ce	13	22, 25, 65, 71, 75, 86, 90, 96, 113, 201, 206, 211, 269
Ce:	9	1, 21, 45, 252, 266, 275, 298, 313, 314

Objects classified by [Sibbons et al., 2015] as carbon stars.
C C-type stars with carbon-rich atmospheres (carbon stars).
C: tentative C-type stars with carbon-rich atmospheres (carbon stars).
Ce C-type stars exhibiting Hα and sometimes [S II] and [N II] emission.
Ce: tentative C-type stars exhibiting Hα and sometimes [S II] and [N II] emission.

The nightly composite spectra were then further combined into a single composite spectrum, and readjusted to the rest frame again using the Arcturus spectrum, in the same way. Two iterations of correction were required to reduce the final composite template to the rest frame with velocity residuals of 0.015 km s^{-1}. The single composite spectrum is shown as the blue curve in Figure 2.5.

Comparison with Figure 2.3 shows smoother Ca II triplet features, due to noise cancellation by the combining process, an important consideration as the spectra had originally been taken with a relatively short exposure time. The undulations in the spectrum are due to the Ca II triplet and to CN absorption lines and provide a better match to the C-type object spectra.

While the inner region of the spectral sample is dominated by C-type stars, the outer region is dominated by M-type stars. Initially, the radial velocities of both the inner and outer region stars were found using the C-type composite template. However, as it is not matched to the spectra in the outer region, a second composite template was created, based on the outer region M-type stars, in a similar manner as for the C-type composite, using the object #36 in the first stage. This is an outer region object and classified in Sibbons et al. [2015] as a dM star. The M-star spectrum is shown as the cyan line in Figure 2.5. The M-type composite shows only three strong absorption lines, due to the Ca II triplet.

The C-type composite was used to measure the radial velocities of all objects in the sample, and the M-type composite was used to re-measure the radial velocities of the outer objects only.

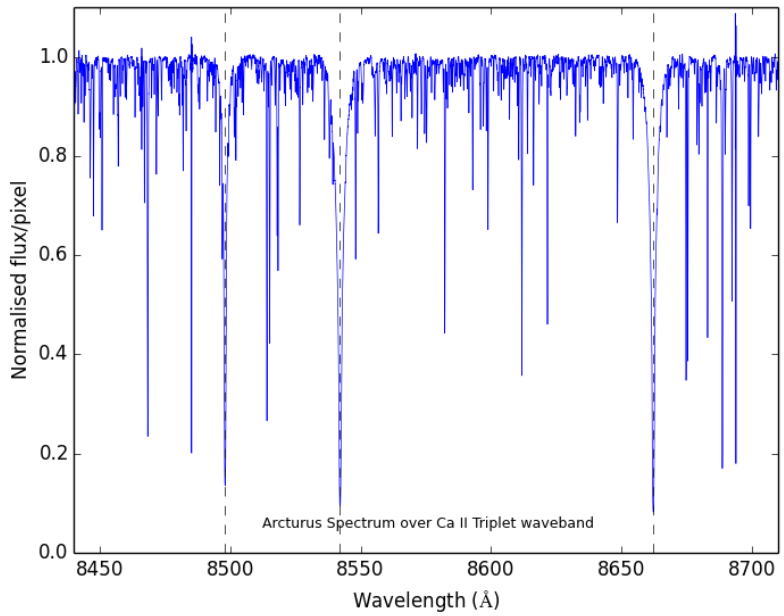

Figure 2.4.: Spectrum of Arcturus over the band 8440 Å to 8710 Å. The spectrum is in the rest frame. The locations of the Ca II triplet lines (at rest) are show as dashed vertical lines.

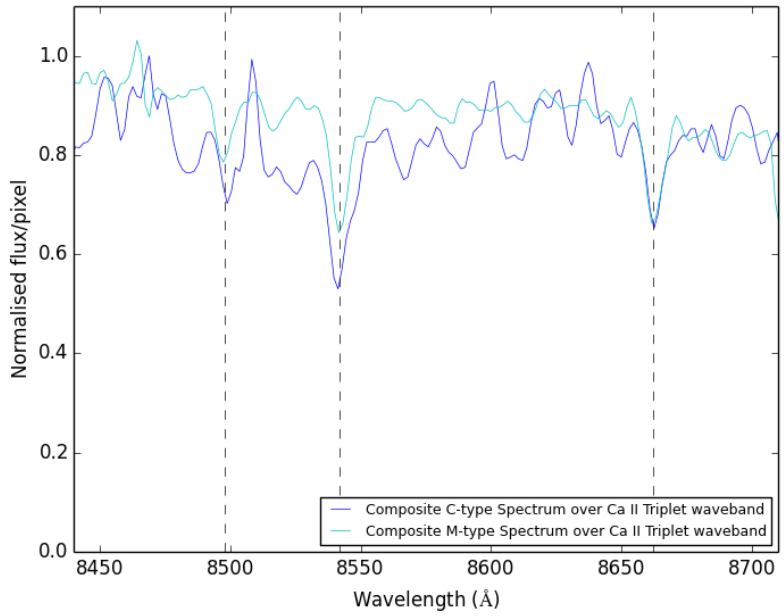

Figure 2.5.: Composite template spectra in the rest frame used for the radial velocity measurements. The centres of Ca II triplet features are shown by the vertical dashed lines.

2.3.3. Cross-correlation function

The cross-correlation function is obtained from the inverse Fourier transform of the product of the Fourier transform of each spectrum. A Gaussian profile is fit to it, and the radial velocity is computed from the location of the peak of the Gaussian, multiplied by the velocity dispersion. If the template spectrum is in the 'rest frame' (i.e. the position of the Ca II triplet as measured in a laboratory) then the offset measured will determine the radial velocity of the object relative to the Earth. To obtain the heliocentric velocity, $V_{\rm helio}$, a heliocentric correction is required to take account of the Earth's orbital motion about the Sun. The corrections adopted[9] were obtained using the *rvcorrect* module in IRAF.

The number of points over which the Gaussian profile is fitted can be selected. After experimentation, it was found that a 9 pixel Gaussian fit ($\equiv$ 13.5 Å or 717 km s^{-1}) provided a reasonable correspondence to the shape of the peak of the cross-correlation function without severely limiting the number of successful cross-correlations.

In general, the better the S/N, the better defined is the cross-correlation peak, the smaller the error and the greater the confidence in the velocity measured. The velocity resolution, and thus the error in radial velocity, $V_{\rm err}$, is proportional to the inverse of the resolving power, R^{-1}, of the spectroscope, and better radial velocity precision is obtained from more highly resolved spectra. *fxcor* reports the velocity error[10], the height of the cross-correlation function, and TDR[11] which effectively measures the SNR of the cross-correlation function. These data can be used to assess how reliable the results are, as we shall see later.

Figure 2.6 shows the cross-correlation function of the carbon star composite template with the spectrum for the object #31 and is used to illustrate a number of points. The cross-correlation function exhibits a clean central peak, with well defined side bands well below the peak. Such a shape will give reliable radial velocity measurements, and was found to be attainable if the $SNR \sim 10 - 20$. As SNR reduces, the cross-correlation peak becomes less well defined and the side bands grow in significance. In the worst cases, the side band levels can become higher than the central peak, and *fxcor* will not be able to fit reliably the Gaussian to the correct peak. In this case invalid results are produced. Means to eliminate these cases are discussed in §2.3.4.

[9] -19.5 km s^{-1} (30 August 2011) and -19.8 km s^{-1} (31 August 2011)
[10] computed from the FWHM of the Gaussian fit to the cross-correlation function
[11] Tonry and Davis r function [Tonry and Davis, 1979]

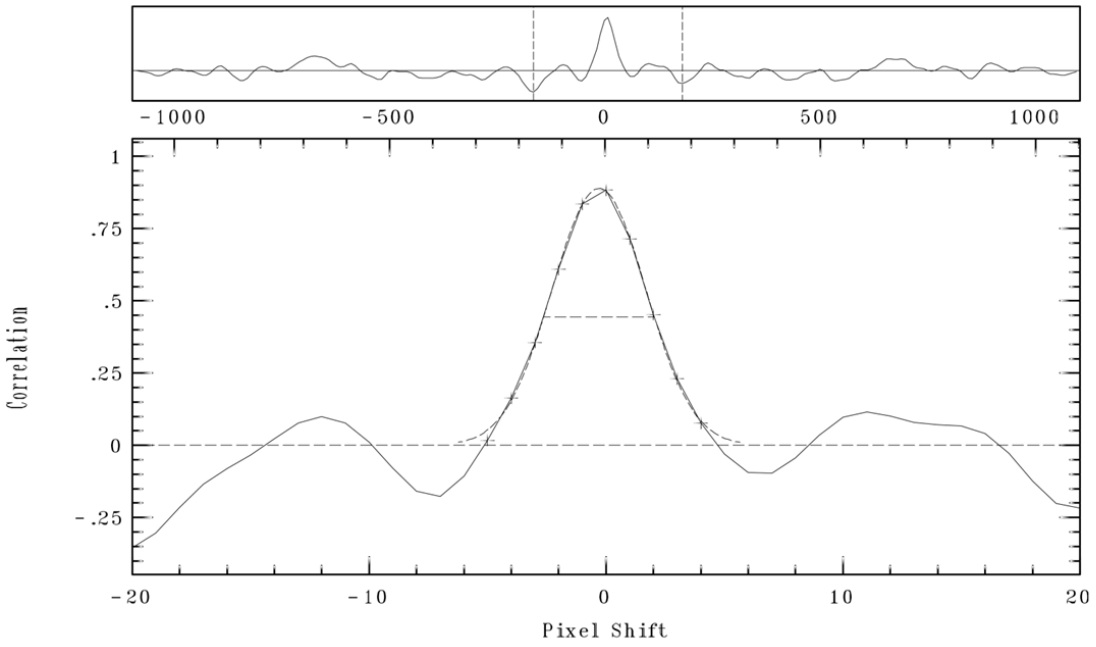

Figure 2.6.: Cross-correlation function of fibre number # 31 for 31 August and the C-type composite template a Gaussian fit of 9 points.

2.3.4. Selection criteria

The quality of the spectra is important. As well as low spectral resolution, many of the spectra had low *SNR* (< 10 /pixel), causing noisy cross-correlation functions. These sometimes returned unreliable results or failed to give a result at all. To overcome these difficulties, selection criteria were adopted to rule out any spectra which might give rise to unreliable results. The criteria were based on the strength of the cross-correlation function, *hght* and a determination of the acceptable range of radial velocities returned.

It was found, by inspection, that cross-correlation functions with $hght > 0.4$ give a reliable peak with low sidebands, but those with $hght < 0.2$ do not. In these cases, the peaks are weak with respect to the sidebands and in some cases, multiple peaks occur. Between these limits, the quality of the cross-correlations degrades but useful results can be achieved in many cases. After visual inspection of each cross-correlation function, I excluded all cross-correlation functions where $hght < 0.2$.

I then examined the *fxcor* velocity returns. In a number of cases, unrealistically high values of $V_{\rm helio}$ were observed. These can come about by selection of the 'wrong' peak by *fxcor* in noisy or multi-peak cross-correlation functions. Values of $V_{\rm helio}$ as large as ± 1554 km s^{-1}, ± 4184 km s^{-1} or ± 5734 km s^{-1} arise, which are regarded as unrealistic, and such values tend to be associated with *hght* values close to 0.2.

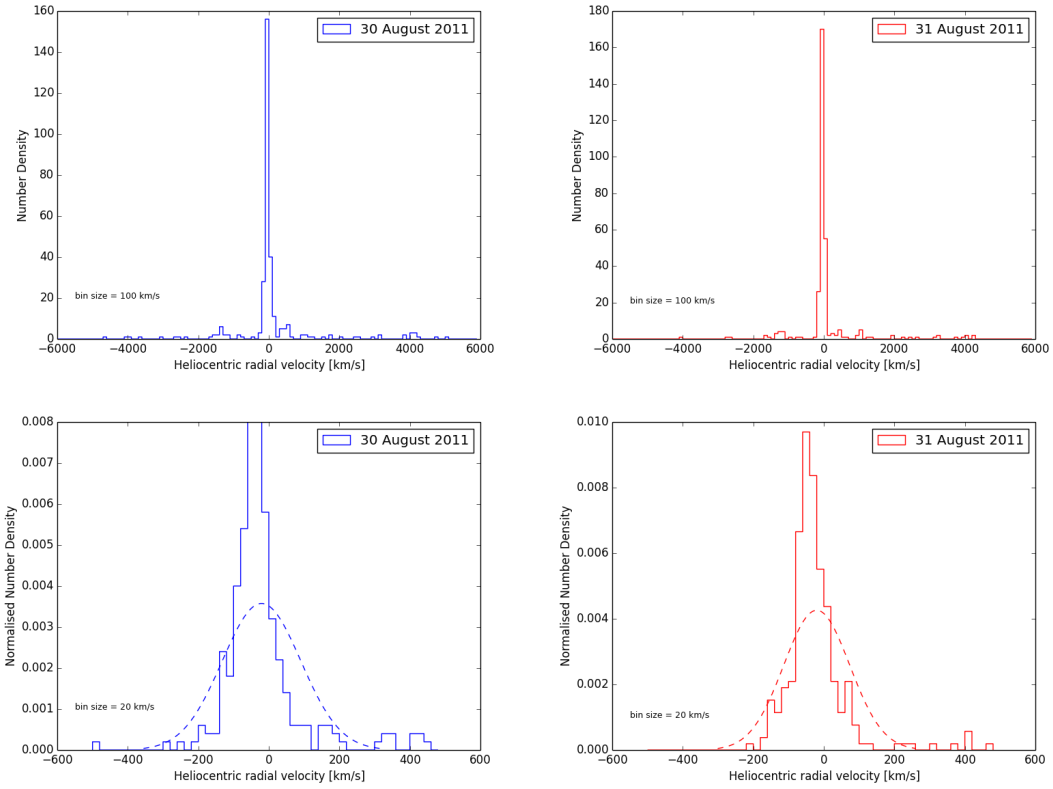

Figure 2.7.: Selection criteria - velocity histograms
Histograms showing the number distribution of heliocentric radial velocities returned from *fxcor*, using the composite template. The upper panels show the histograms over the velocity range -6000 km s^{-1} $< V_r <$ $+6000$ km s^{-1} for each night of observation. The lower panels expand these histograms over a velocity interval of -600 km s^{-1} $< V_r <$ $+600$ km s^{-1} for each night. Bin sizes are shown on each panel. The histograms show that the dominant number density lies within -200 km s^{-1} $< V_r <$ $+200$ km s^{-1}.

Analysis of the frequency distribution of velocity returns from *fxcor* showed that most returns fall within ± 200 km s^{-1}. Figure 2.7 shows histograms of the number distribution of $V_{\rm helio}$ over all the *fxcor* returns, and a clear narrow peak lying between ± 200 km s^{-1} can be seen. The standard deviations about the peaks for 30 August and 31 August are $\sigma = 66.19$ km s^{-1} and $\sigma = 55.56$ km s^{-1} respectively. Noting that on each night, some of the cross-correlation functions were returned with the reference 'INDEF', the number of returns falling within the ± 200 km s^{-1} range is 237 out of 320 on 30 August, (74% of the total population), and 253 out of 321 on 31 August, (79% of the total population). While there are clearly some returns lying outside the range, the histograms cut off quite sharply at that point and it would be necessary to extend the range by a considerable amount to add further numbers to the sample. I conclude therefore that values of $V_{\rm helio}$ falling outside this range are more likely to be affected by bad correlation functions due to noise and are rejected.

2.4. Results and Analysis

2.4.1. Cross-correlation results with the C-type template

All 323 objects were cross-correlated with the C-type composite template. Application of the criteria discussed in §2.3.4 resulted in 128 successful cross-correlations in the inner region and 107 in the outer region on 30 August, and 129 in the inner region and 124 in the outer region on 31 August. From the population of 96 C-type AGBs in the inner region, 89 gave acceptable results on 30 August and 92 on 31 August.

Table 2.3 summarises the results. Column [3] shows the mean heliocentric radial velocities $\langle V_{\rm helio} \rangle$ of the samples. For the inner region, this can be considered a good approximation to the heliocentric radial velocity of NGC 6822. The mean individual error in column [4] is large and reflects the low resolution and low *SNR* of the spectra. $\sigma(V_{\rm helio})$ in Column [5] is the velocity dispersion, which is also high, nevertheless, the standard error of the mean (SE) in column [6] is small, $3 - 8$ km s^{-1}, implying that, provided the individual errors are random, the mean and median (column [7]) heliocentric radial velocities are well constrained. The mean velocities show reasonable consistency from night to night, with differences similar to the standard error in the mean, SE. The inner region differs by more than 24 km s^{-1} from the outer region[12], supporting the suggestion that these objects in the outer region are not part of NGC 6822 [Sibbons et al., 2015].

The aggregated results of the cross-correlation of the spectra of objects in the outer region using the M-type template are also presented in Table 2.3. Both the formal errors, $\langle V_{\rm err} \rangle$, and the spread of results, $\sigma(V_{\rm helio})$, are reduced by switching to the M-type template in the outer region. The improvement observed in outer region errors when an M-star template is used appears to confirm the conclusion that the outer stars are predominantly M-type, dM-type, dK-type and other unclassified foreground stars of the Milky Way.

The full results of the radial velocity measurements and their individual errors over both nights are shown in Appendix B, with explanations of the column contents. Spectra which failed to meet the acceptance criteria are not included.

Figure 2.8 plots $V_{\rm helio}$ of all objects which meet the acceptance criteria, by distance D from the galactic centre, for both nights. It shows a number of differences between the inner and outer populations. The inner objects tend to clump more closely

[12]This supercedes the preliminary data stated in Sibbons et al. [2015] and is the result of more detailed work.

Table 2.3.: Summary of Results for spectra with *hght* ≥ 0.2 and $|V_{\rm helio}| < 200$ km s^{-1}.

Template Object Composite Template [1]	No. of Objects [2]	$\langle V_{\rm helio}\rangle$ [km s^{-1}] [3]	$\langle V_{\rm err}\rangle$ [km s^{-1}] [4]	$\sigma(V_{\rm helio})$ [km s^{-1}] [5]	SE [km s^{-1}] [6]	Median $V_{\rm helio}$ [km s^{-1}] [7]
30August2011						
Inner region (C-template)	128	−45	±42	45	±4	−43
Outer region (C-template)	107	−20	±63	81	±8	−19
Outer region (M-template)	100	−28	±54	60	±6	−22
31August2011						
Inner region (C-template)	129	−51	±32	29	±3	−51
Outer region (C-template)	124	−17	±60	66	±6	−9
Outer region (M-template)	133	−18	±49	58	±5	−19

around the median value for the inner region and they are therefore likely to be part of the same dynamical system, while the outer objects are much more widely spread about a different median value, indicating a separate population. This suggests that the inner population is associated with NGC 6822, supporting similar conclusions in Sibbons et al. [2012, 2015], while the outer population is not.

Thus, I conclude that the heliocentric radial velocity of NGC 6822, as based on the sample of the inner C-type AGB population, lies in the median range of -43 ± 4 to -51 ± 3 km s^{-1} (1σ). The data for 31 August are preferred, owing to their better *SNR*, lower errors and greater number of successful cross-correlations than the data for 30 August, and provides $V_{\rm helio} = -51 \pm 3$ km s^{-1} (1σ). This compares favourably with published values described earlier.

2.4.2. Velocity error, *hght* and *SNR*

Figure 2.9 shows a set of correlation diagnostics comparing $V_{\rm err}$, *hght* and *SNR* for objects in the inner region. The following trends can be seen.

The upper panel of Figure 2.9 show the degree of correlation between $V_{\rm err}$ and *hght*. The cut-off at *hght*= 0.2 is shown as a dotted line. Auto-correlating the composite template, *hght*= 1 and $V_{\rm err} = 0$ as expected. In the upper panel, dashed lines are drawn as a guide to the eye through this point and show how $V_{\rm err}$ is inversely proportional to *hght* with reduced scatter as *hght* increases. The scatter for the 31 August is slightly lower than for the 30 August.

The middle panel of Figure 2.9 show the degree of correlation between *hght* and

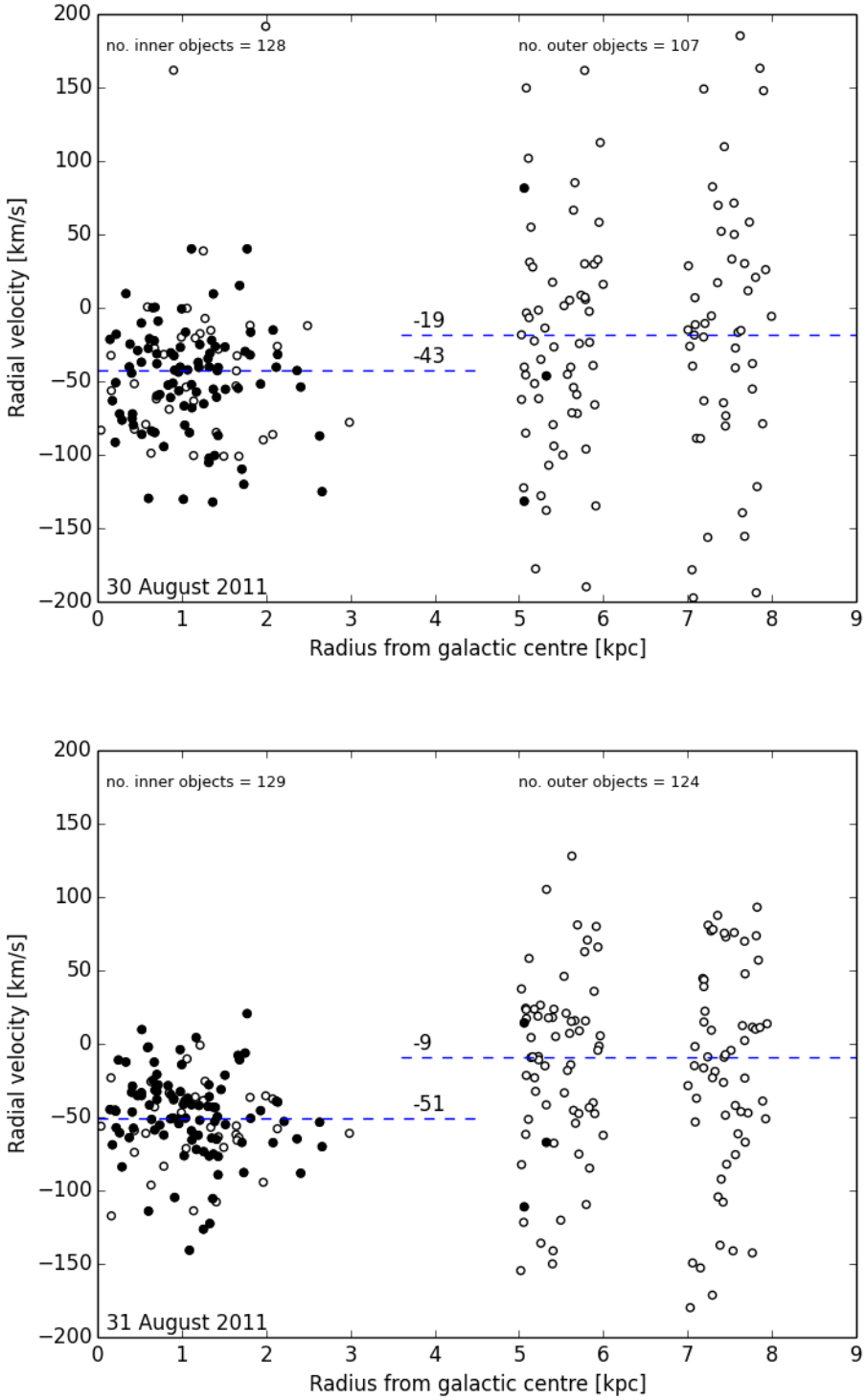

Figure 2.8.: Relationship between V_{helio} and distance D from the galactic centre, left panel for 30 August 2011 and right panel for 31 August 2011. The horizontal dashed lines represent the median radial velocity of the sample from Table 2.3. C-type AGBs are shown as black points.

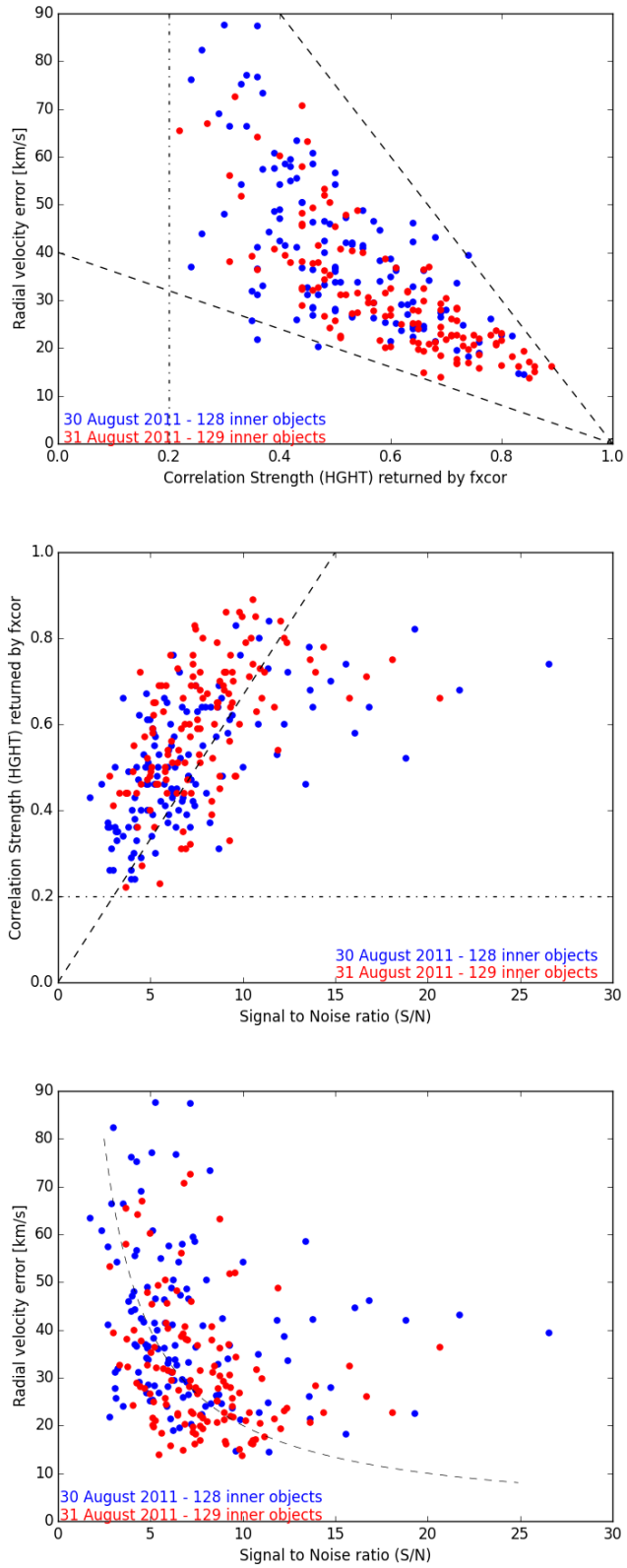

Figure 2.9.: Correlation diagnostics for objects in the inner region plotted for both nights. Upper panel: $V_{\rm err}$ and correlation strength (*hght*). Middle panel: correlation strength (*hght*) and *SNR*. Lower panel: $V_{\rm err}$ and signal to noise ratio (*SNR*). Each circle corresponds to the cross-correlation outcome for one object spectrum against the composite C-type template. The dot-dashed lines show the cut-off imposed at *hght* = 0.2. See §2.4.2 for a description of the dashed lines and curves.

SNR. Again the cut-off at *hght*= 0.2 is shown as a dotted line. The template *SNR* is 15 and a dashed line is plotted from the origin to (*SNR*=15, *hght*=1). The *hght* is slightly better for a given *SNR* on the night of 31 August, more points lie above the line, than on the 30 August.

The lower panel of Figure 2.9 show the resulting relationship between $V_{\rm err}$ vs *SNR*. The blue dashed curves represent $V_{\rm err} \propto 1/SNR$ with a constant of proportionality, estimated by eye, of 200. The inverse form of the curve can be inferred from Tonry and Davis [1979] (their equation 24), which is the basis of the velocity error function in *fxcor*. The denominator of this equation contains the quantity r (TDR in IRAF), where $r = hght/\sqrt{2}\sigma_a$. σ_a is the rms of a distorting function applied to the cross-correlation function and can be considered to represent noise in the cross-correlation function. For well matched object and template spectra, and a wavelength interval containing good spectral lines, such as are set up in this study, we might expect a relationship between the *SNR* of the cross-correlation function and, indirectly, the *SNR* of the spectra, leading to an inverse relation between $V_{\rm err}$ and *SNR*. $V_{\rm err}$ appears to be slightly better constrained on 31 August than on 30 August, as can be inferred by the greater number of points lying below the curve for that night.

Some of the spread in the correlations will be due to the mismatch between the spectral features of the composite template and the individual targets. Even with exquisite *SNR*, a mismatch in spectral type will result in a decreased *hght*, and increased $V_{\rm err}$, compared to a star which matches the spectral type of the template.

2.4.3. Rotation of the carbon star population

In the inner region, the $V_{\rm helio}$ of each C-type object was compared to the sample mean, $\langle V_{\rm helio} \rangle$, which I take to be the mean motion of the galaxy. This provides a measure of the motion of each object in the rest frame of the galactic centre of NGC 6822. Figure 2.10 plots the locations of the inner C-stars, colour coded by the value of its residual velocity, $V_{\rm helio} - \langle V_{\rm helio} \rangle$, using a colour range from red (for positive values) to blue (for negative values). The colour range is consistent with red and blue shift and indicates whether an object is receding or approaching in the rest frame of NGC 6822. In the lower panel for 31 August, it can be seen that receding objects dominate the south east sector and approaching objects the north west sector, suggesting rotation of the C-star population about an axis, oriented approximately NE-SW. In the upper panel, for the night of 30 August, the pattern is less obvious but still apparent.

To examine this further, an axis of rotation was hypothesised lying in the plane

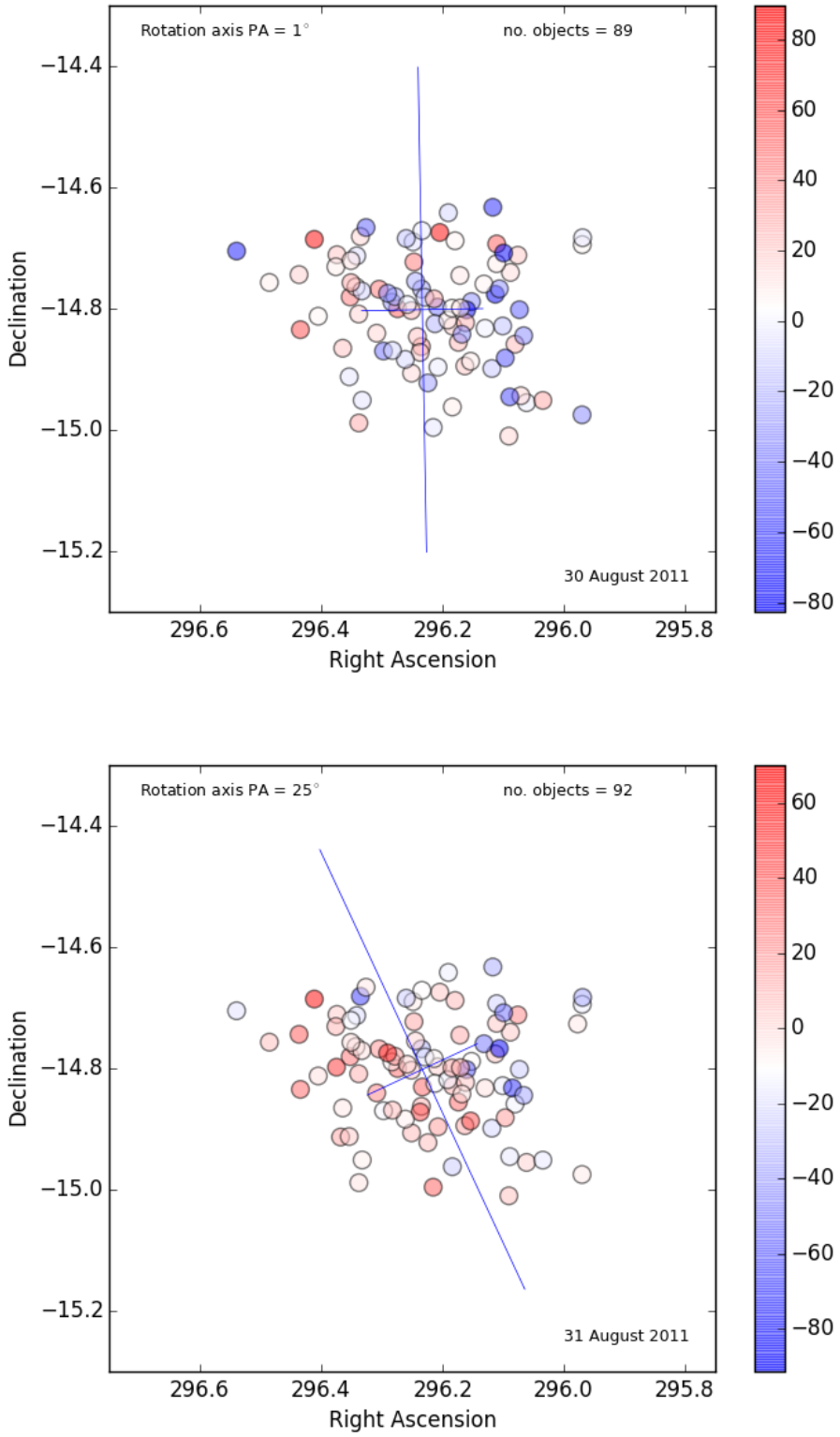

Figure 2.10.: Carbon star sample rotation
Residual velocity, $V_{\rm helio} - \langle V_{\rm helio} \rangle$, plots of the carbon star sample in the inner region of NGC6822. The long axis represents a derived axis of rotation and passes through the galactic centre at the intersection with the short axis.

of the sky and passing through a pivot point at the centre of the galaxy. The axis was rotated through 360 steps of 1°, starting at a position angle (PA) of 0°. At each step, the mean of the residual velocities of the stars on either side of the axis was computed. The subsample of stars falling on one side of the line is termed the 'North Bin', and for an axis with PA= 90°, this is defined naturally. The subsample falling on the other side of the line is termed the 'South Bin'. Membership of each bin changes as the axis of rotation sweeps around and the value of its mean velocity residual also changes. By plotting the mean velocity residuals over 360°, a clear rotational signature is observed, see Figure 2.11. The cyan curves plot the mean rotational velocity of the 'North Bin' and the dark blue curves plot the mean rotational velocity of the 'South Bin'. In both bins and on both nights the curves rise and fall in opposition as the putative axis is rotated, confirming my impression of a rotating population. Furthermore, the curves for the 30 August and 31 August both suggest a similar sense of speed and rotation, even though the curves for 30 August are noisier.

The green curve in each case shows the sum of the average 'North' and 'South' velocities, which is generally offset from zero as the number of stars in the 'North' and 'South' bins is not always equal at each step. Over the full 360°, the offset should average to zero if the centre of the stellar sample and the pivot point of the hypothesised axis of rotation (the galaxy centre) are coincident. In this case, the green curve appears to lie mainly above the zero line, which suggests that the pivot point adopted does not coincide perfectly with the rotational centre of the sample. Changing the co-ordinates of the galactic centre in my analysis to the centre of the sample eliminates the offset, but has no significant effect on the rotation characteristics.

Using a least squares method, a sinusoid of the form $\hat{y} = V_{\rm rot}\sin(\theta - \theta_0) + y_0$ was fitted to the measured residual velocities, y, for each bin, such that $(\hat{y} - y)^2$ is minimised. The peak amplitude gives the mean rotational velocity, $V_{\rm rot}$, θ tracks the PA of the hypothesised axis and is stepped in 1° intervals, and θ_0 is the value of θ when $\hat{y} - y_0 = 0$. y_0 is the offset. Solving for y_0, θ_0 and $V_{\rm rot}$, $\hat{y}$ is plotted as magenta and blue curves in the lower panels of Figures 2.10 for the 'North' and 'South' bins respectively. The rotation axis PA occurs at the peak of the sinusoid, so its PA is given by the value of θ when $\hat{y}$ is a maximum. This occurs at $\theta_0 \pm 90°$.

Table 2.4 provides a summary of the results obtained, with $V_{\rm rot}$ in column [2]. In column [3], I calculate the error in the velocity amplitude, $\Delta V_{\rm rot}$, from the RMS of the residual velocities found by deducting the sine function from each measured value over 360°, using the best fit PA. In columns [4] and [5], I show the PA of the

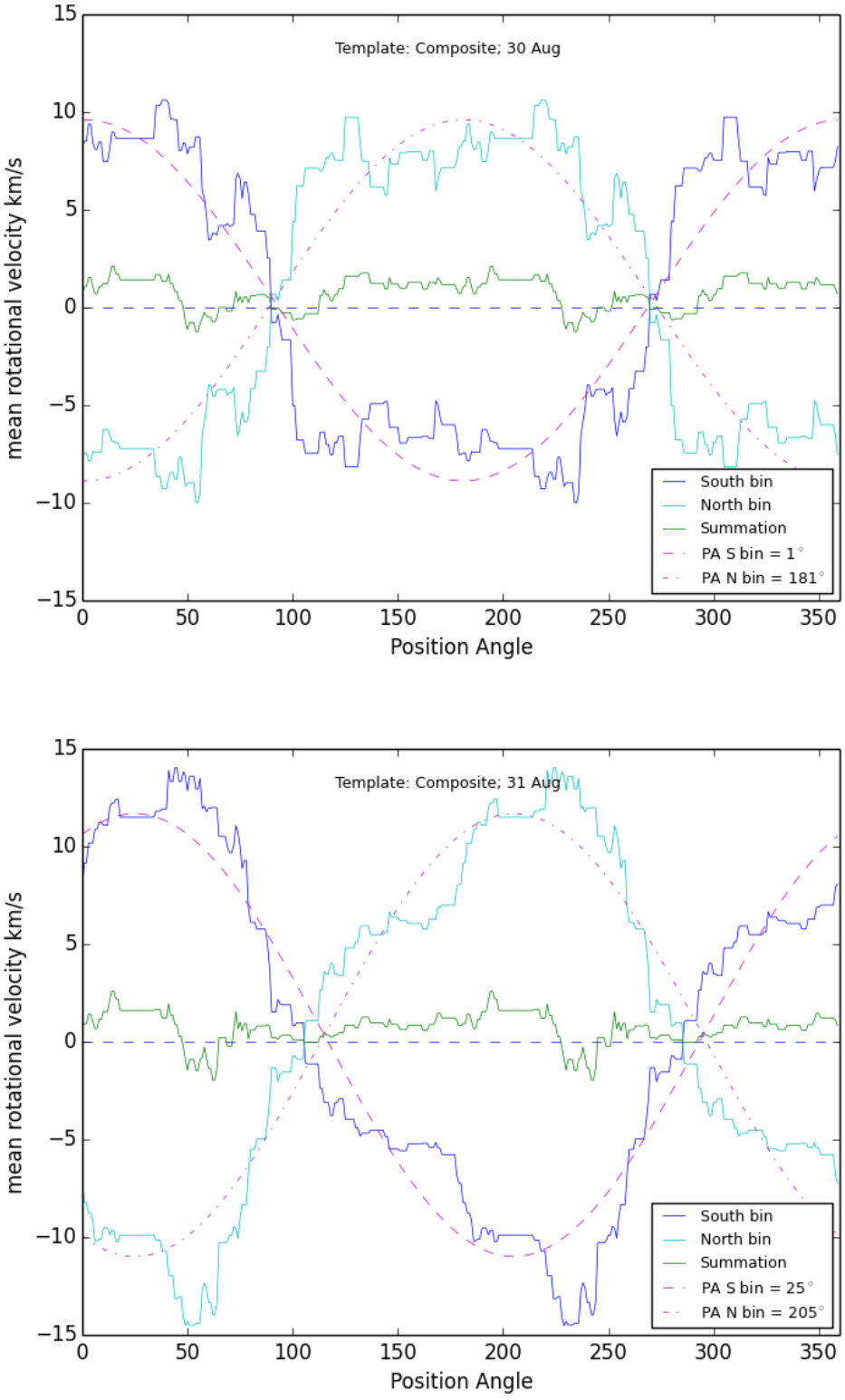

Figure 2.11.: Rotational signature of carbon star component in NGC 6822 derived by plotting the mean residual velocities, $\langle V_{\rm helio} - \langle V_{\rm helio} \rangle \rangle$, on either side of the putative rotation axis as a function of its position angle.

Table 2.4.: Summary of sinusoidal least squares fit to mean residual velocities.

Date	Rotation rate		Rotation axis		Offset
	$V_{\rm rot}$	$\Delta V_{\rm rot}$	PA	ΔPA	y_0
	km s^{-1}	km s^{-1}	$^\circ$	$^\circ$	km s^{-1}
[1]	[2]	[3]	[4]	[5]	[6]
30 Aug 2011	9.2	$\pm$2.3	1°	21°	0.4
31 Aug 2011	11.3	$\pm$2.1	25°	14°	0.4

galactic rotation axis and an estimate of its positional error found by taking the RMS, over 360°, of $\theta - \theta'$, where θ' is the angle which gives the value of $\hat{y}(\theta)$ in the sine function using the best fit PA. Column [6] shows the mean offset of the sinusoid due to the axis pivot point and the galactic centre not being coincident. Details of the error analysis calculations are given in Appendices A.2 and A.3.

The sense of rotation on both nights is the same and is such that the south eastern side is receding and the north western side is approaching, which corresponds with the rotation of HI gas in Weldrake et al. [2003]. Moreover the rotation velocities and estimated PA for each night correspond within the estimated errors which gives me good confidence in the result. Nevertheless, owing to the better quality spectra for 31 August, better SNR and better error results, I take the results for 31 August, i.e $V_{\rm rot} = 11.3 \pm 2.1$ km s^{-1} and $PA = 25 \pm 14^\circ$ as the more reliable.

2.5. Discussion and Conclusion

The heliocentric radial velocity obtained for the intermediate age, carbon star component of NGC 6822 is -51 ± 3 km s^{-1}, based on the results from the better of the two nights of observing. This is a little lower than its HI counterpart (-57 ± 2 km s^{-1} [Koribalski et al., 2004]) but shows only 1.6σ difference, which is not significant. The grouping of objects in the inner and outer regions of the observed field indicates that the inner objects belong to NGC 6822, while the outer objects are more likely to be Milky Way stars, in support of the conclusion in Sibbons et al. [2015].

Rotation of the carbon star population about an axis having $PA = 25 \pm 14^\circ$ has been shown with a rotation speed $V_{\rm rot} = 11.3 \pm 2.1$ km s^{-1}, based on the better of the two observing nights. The sense of rotation is that the SE corner is receding and the NW corner is approaching, which is similar to the rotation of the HI disk [Weldrake et al., 2003]. Furthermore, I infer from Weldrake et al. [2003], that the

PA of the rotation axis of the HI disk is $\sim 20^\circ$ to $\sim 40^\circ$ in the plane of the sky, assuming the rotation axis is perpendicular to the major axis of the gas disk. This is comparable to my estimate of the sky projected rotation axis of the C-type stellar population in this study. Thus, I find that both axes are approximately coincident and the sense of rotation of the stars and gas is the same, leading me to conclude that NGC 6822 is not a PRG.

Nevertheless, I note that the *PA* of the major axes of the isodensity contours of the RGB stars in Demers et al. [2006] varies from 80° for the innermost contour (radius= $10'$) to 65° for the outermost contour (radius= $35'$). The envelope of my inner sample of carbon stars has an angular radius of $\sim 17'$, and so falls between these extremes. Hence, there is a misalignment of $\sim 45^\circ$ between my rotation axis and the respective isodensity profile.

Furthermore, since $V_{\rm rot}$ is derived from mean velocities, it is reasonable to adopt the mean distance of the carbon star sample from the galaxy centre as a basis for further comparative discussion. This distance is $\langle D \rangle = 1.1$ kpc. Interpreting the velocity diagrams of Weldrake et al. [2003], the rotation speed of the HI disk can be estimated to be ~ 30 km s^{-1} at 1.1 kpc (≈ 8 arcmin) from the galactic centre. This rotation speed is faster than my carbon star sample confirming differences in the rotation speeds of the rotationally supported gas and the pressure supported intermediate age stellar populations.

3. Potential for future work

3.1. Further Spectroscopy

The sample of inner objects (< 4 kpc) from the centre of NGC 6822 observed spectroscopically up to now is a total of 135, of which 96 had been classified by Sibbons et al. [2015] as C-type AGBs (carbon stars). These stars were observed using a grating suited primarily for spectral classification and for a period of only 25 minutes, which was adequate for this purpose. However the *SNR* and spectral resolution were not ideal for radial velocity measurements.

There is no doubt that better *SNR* and higher resolution would improve the results of the existing sample and provide more convincing evidence of the stellar rotation in NGC 6822 in the existing sample. However adding to the C-type AGBs in the inner region by filling the gap between the central sample presented here and the 4 kpc radial extent inferred by Sibbons et al. [2012], would provide a much greater number of targets spread over a larger spatial distribution than measured so far. This would enable finer resolution of the kinematics within the isophotes, so as to examine radial velocities, and a reduced standard error in the mean. Hence it is proposed to observe the spectra of ~ 320 C-type stars lying in the elliptical region in Figure 2.2, using the AAOmega spectroscope on the Anglo-Australian Telescope (AAT) in service mode, with a grating suited to radial velocity measurement and a longer exposure time. The science benefits in the proposed measurements are:

- to confirm the rotational signature with better spectra (higher *SNR* and greater resolving power).
- to extend the measurements further out, with a greater number of points specifically chosen for this purpose, to see whether the speed of rotation and the axis of rotation changes with distance, since the PA of the isophotes in the right hand panel of Figure 2.1 is observed to change with radial distance.
- to explore further the apparent misalignment of the rotation axis and the isophotes.

- to explore how many of the C-type stellar candidates identified photometrically by Sibbons et al. [2012] beyond 4 kpc are genuine members of NGC 6822.

The AAOmega service programme permits nightly exposures of up to 6 hours in total in one shift, and booking can be done at any time, subject to AAO acceptance of the observing proposal. Ideally, observations should be scheduled for 2 nights to reduce the risk of loss of data owing to problems with the measurements. Exposures, see Figure 3.1, will be split into 3 data frames to minimise read out or cosmic ray problems. This reduces the *SNR* by a small amount but protects the measurements from instrument problems. 'Seeing' should be logged and reported on both nights.

It is proposed that all 96 inner C-type AGBs classified by Sibbons et al. [2015], and already studied in §2 plus 3 which lie outside 4 kpc [1] are targetted. Table 3.2 lists these objects and provides basic data for each including position and magnitude in the $I-$band. Up to 265 new targets of C-type AGBs will be selected from the target lists of Sibbons et al. [2012] within the stellar isophote shown in Figure 2.2 to enlarge the carbon star sample inside the isophote. Other stellar types and clusters will be excluded. The final number of targets will depend on the availability of fibres within AAOmega, restrictions placed on the AAOmega 2dF field plate layout by the fibre positioning software and the number of guide stars and sky fibres used. It is proposed to re-use guide stars and sky fibres from the previous study, and which are listed in Table 3.3. Further sky fibres adjacent to the new C-type targets are likely to be required, but sky fibres in the outer region can be re-used. Thus, while the maximum number of targets could be 364, the total is more likely to be ~ 320.

It is also proposed to use the AAOmega high resolution grating (1700D) which was specifically designed for use with the Ca II triplet and is therefore ideally suited to these new measurements. Centred on 8600 Å, it has a resolving power, $R\ (= \lambda/\Delta\lambda) = 10,338$ [reference: AAOmega grating calculator]. Thus at the central wavelength, the velocity resolution[2] is 29.02 km s^{-1} Å^{-1} $\equiv$ 24.14 km s^{-1} pixel^{-1}.[3]

AAOmega provides an on-line *SNR* calculator to determine the exposure times and resulting *SNR*. Exposure times have been reviewed using this tool. The faintest C-type star in the original sample has a $m_{\rm app} = 20.1$ (#262) and the brightest $m_{\rm app} = 17.8$ (#31), see Table 3.2. The mean magnitude of the stars in the sample is $m_{\rm app} = 19.2$. Allowing for readouts, the maximum exposure time is 348 minutes, and using this value, I have computed, using the AAOmega Multi-Object Spectrograph S/N Calculator, the *SNR* achieved for the faintest and brightest stars in my sample,

[1] #137 (5.32 kpc), #148 (5.06 kpc), #366 (5.06 kpc)
[2] velocity resolution $\Delta v = c\ R^{-1}$
[3] central resolution 0.832 Å pixel^{-1} [reference: AAOmega grating calculator]

Table 3.1.: Further observations: exposure time and *SNR* for NGC 6822 carbon star objects using AAOmega (3 Data Frame strategy), Grating 1700D, red camera, $I-$band.

	$I-$ (mag)	Exposure mins	Total h:m	*SNR*/Å dark sky	*SNR*/Å grey sky	*SNR*/Å bright moon	*SNR*/pixel dark sky	*SNR*/pixel grey sky	*SNR*/pixel bright moon
Faintest	20.1	348	6h0m	7.38	7.09	4.66	3.64	3.50	2.30
Mean	19.2	348	6h0m	16.13	15.55	10.47	7.96	7.68	5.17
Brightest	17.8	348	6h0m	49.21	47.95	35.08	24.30	23.67	17.32
Limiting mag. (*SNR*/Å $\geqslant 8$) (No. of brighter objects)				19.75 (88/96)	19.70 (86/96)	19.25 (54/96)			
Saturating mag.				13.80	13.81	13.87			

$I-$band magnitudes are taken from Table 3.2.
Magnitudes are given for the faintest star (ID 165760: fibre#262) in this sample, and the brightest (180514: fibre #31).
The mean magnitude of the sample = the median.
The limiting mag. is the faintest magnitude which provides *SNR*/Å $\geqslant 8$ for the exposure time stated,
The saturating mag. is calculated based on a saturating camera photon count of 65,000 counts/readout/pixel (AAOmega).
All calculations are made using the AAOmega Multi-Object Spectrograph S/N Calculator.

and for the mean magnitude of the sample (the mean magnitude and the median magnitude of the sample are equal so we can be sure that the distribution of magnitudes is not biassed either way). The computations were calculated for dark sky, grey sky and bright moon conditions and the results are shown in Table 3.1.

From my experience using grating 385R, an *SNR*/pixel > 10 is desirable to give a good basis for cross-correlation. This is equivalent to *SNR*/Å > 8, derived using the AAOmega exposure calculator for the 385R grating. I have aimed at obtaining *SNR*/Å $\geqslant 8$ using the 1700D grating with the sample. It is clear from Table 3.1 that this cannot achieved for the faintest object, even using the maximum time available for observation in one service shift. It can be achieved for many of the objects, using all time available in a single service shift. The limiting magnitudes in the three sky conditions in Table 3.1 are the faintest magnitudes required to achieve an *SNR*/Å $\geqslant 8$, and the number of objects in the current sample which meet this condition is shown. It can be seen that dark sky and grey sky conditions give similar numbers and are both acceptable conditions for the observations.

Table 3.1 also shows the magnitudes at which the CCD camera saturates. It is clear that the saturation level is well above the magnitude of the stars in the sample.

Table 3.2.: C-type objects from original work for re-measurement.

[1] Name:	[2] Type:	[3] Original Fibre# :	[4] RA: (rads)	[5] DEC: (rads)	[6] I: (mag)	[7] Comments:	[8] Name:	[9] Type:	[10] Original : Fibre# :	[11] RA: (rads)	[12] DEC: (rads)	[13] I: (mag)	[14] Comments:
217716	Ce	1	5.17027247	-0.2594010	19.3		299996	C:	137	5.16228250	-0.2660133	...	outer
239630	C:	2	5.17197707	-0.2609461	19.4		276398	C:	148	5.16129639	-0.2639907	...	outer
210316	C:	3	5.17375585	-0.2589137	18.9		245610	C	174	5.16564807	-0.2613645	19.2	
174035	C	4	5.17270284	-0.2567563	19.1		183391	C	191	5.16770974	-0.2572654	18.5	
199974	C	6	5.17271666	-0.2582747	19.2		193714	C	193	5.16814535	-0.2578942	19.4	
194949	C:	7	5.17232250	-0.2579722	18.9		178893	C	198	5.16810753	-0.2570137	19.0	
188246	C:	10	5.17464888	-0.2575548	18.3		197170	Ce	201	5.16883184	-0.2581060	19.0	
172656	C	11	5.17559281	-0.2566506	19.3		209652	C:	204	5.16765084	-0.2588725	19.3	
211898	C	12	5.17155892	-0.2590155	18.8		188974	Ce	206	5.16847187	-0.2575989	19.2	
190283	C	18	5.17215742	-0.2576813	19.6		201131	C	207	5.16896929	-0.2583446	19.2	
168284	C:	19	5.17335443	-0.2563137	19.0		191195	C	208	5.16802899	-0.2577366	19.5	
224407	C:	20	5.17370059	-0.2598693	19.5		201043	C	210	5.16745013	-0.2583383	19.1	
213379	Ce	21	5.17038882	-0.2591144	19.9		205865	Ce	211	5.16951180	-0.2586350	19.3	
200573	Ce	22	5.17095896	-0.2583116	19.0		212970	C	214	5.16732795	-0.2590868	19.5	
219598	C	23	5.17136257	-0.2595285	19.0		207096	C	220	5.16900274	-0.2587111	19.3	
203106	C:	24	5.17207816	-0.2584643	19.4		170279	C	221	5.16564153	-0.2564664	19.0	
209216	Ce	25	5.17024265	-0.2588454	19.1		170004	C	226	5.16810535	-0.2564446	19.6	
197464	C	28	5.17112041	-0.2581235	19.0		212351	C	228	5.16910601	-0.2590451	19.7	
180514	C	31	5.17273484	-0.2571025	17.8	brightest	167638	C	229	5.16563207	-0.2562662	18.7	
191382	C	32	5.17149129	-0.2577482	19.2		174226	C	230	5.16749667	-0.2567709	19.5	
218420	C	38	5.17253776	-0.2594480	19.0		173378	C	235	5.16790464	-0.2567073	19.2	
229856	C	43	5.17259885	-0.2602848	19.0		191318	C	246	5.17026811	-0.2577444	18.9	
201454	Ce	45	5.17056118	-0.2583630	19.4		195133	Ce	252	5.17017138	-0.2579829	19.4	
184448	C	48	5.17379440	-0.2573289	19.0		184858	C	257	5.16916346	-0.2573521	19.6	
248633	C:	53	5.17207307	-0.2615996	18.9		195884	C	260	5.16990522	-0.2580270	19.5	
229643	C	54	5.17235014	-0.2602698	18.9		165760	C	262	5.16974378	-0.2561144	20.1	faintest
220153	Ce	65	5.17030883	-0.2595673	19.6		200300	Ce	266	5.16939180	-0.2582946	19.7	
240673	C	68	5.16724505	-0.2610164	19.7		158986	C	267	5.16949725	-0.2555467	19.2	

Continued on next page

Table 3.2: C-type objects from original work for re-measurement (cont.).

Name:	Type:	Original Fibre# :	RA: (rads)	DEC: (rads)	I: (mag)	Comments:	Name:	Type:	Original Fibre# :	RA: (rads)	DEC: (rads)	I: (mag)	Comments:
237395	C	70	5.16740795	-0.2608137	19.9		157078	C:	268	5.16821662	-0.2553896	18.2	
228306	Ce	71	5.17055536	-0.2601660	19.8		200182	Ce	269	5.16914819	-0.2582873	18.9	
223056	Ce	75	5.17073498	-0.2597699	19.6		168826	C	274	5.16930454	-0.2563544	19.0	
237999	C	76	5.16772865	-0.2608481	20.0		168690	Ce	275	5.16889729	-0.2563437	19.2	
231793	C	80	5.17008412	-0.2604457	19.0		179183	C	287	5.16577534	-0.2570288	19.7	
208620	C	85	5.16793227	-0.2588066	18.5		192177	C	290	5.17198944	-0.2577977	19.7	
219351	Ce	86	5.17110441	-0.2595120	19.4		169202	C	292	5.17051318	-0.2563854	19.1	
226097	C	88	5.16979541	-0.2599910	19.3		165127	C	295	5.17025720	-0.2560621	18.8	
215861	Ce	90	5.16920854	-0.2592783	19.5		194777	Ce	298	5.17103314	-0.2579611	19.0	
250173	C	91	5.16993358	-0.2617290	19.2		167938	C	305	5.17070953	-0.2562875	18.8	
225648	C	94	5.16902165	-0.2599580	18.8		193220	Ce	313	5.17124331	-0.2578641	19.1	
242563	C	95	5.16938162	-0.2611385	19.8		198595	Ce	314	5.17067826	-0.2581899	19.7	
208714	Ce	96	5.16936926	-0.2588139	19.3		188333	C:	322	5.17230069	-0.2575596	18.6	
226603	C	98	5.16824425	-0.2600317	18.7		174472	C	323	5.17213415	-0.2567878	19.0	
209650	C	104	5.16843987	-0.2588725	19.4		176863	C	326	5.17230141	-0.2569241	19.0	
253239	C	112	5.16775483	-0.2619763	19.4		187649	C:	328	5.17044118	-0.2575175	18.7	
199754	Ce	113	5.16980850	-0.2582621	19.2		167230	C	330	5.17202798	-0.2562337	20.0	
207586	C	119	5.16988268	-0.2587426	19.1		177839	C	334	5.17048700	-0.2569643	19.4	
223739	C	122	5.16885584	-0.2598218	19.8		164010	C	338	5.17186654	-0.2559728	19.1	
239687	C	124	5.16677599	-0.2609499	19.3		152918	C:	366	5.18036411	-0.2550265	...	outer
216688	C:	125	5.16757812	-0.2593336	18.8		204144	C	398	5.17324316	-0.2585264	19.0	
222468	C	136	5.16785955	-0.2597292	19.5								

Table 3.3.: Guide stars and sky fibres

[1] Name:	[2] Type:	[3] Original Fibre# :	[4] RA: (°)	[5] DEC: (°)	[6] Mag: (mag)
twomass13	Guide	50	5.17404311	-0.2659673	13.4
twomass675	Guide	100	5.16945725	-0.2747138	13.7
257782	Guide	150	5.16344314	-0.2623734	13.6
twomass39	Guide	200	5.15987903	-0.2580619	13.9
47405	Guide	300	5.17213488	-0.2456880	13.1
twomass790	Guide	400	5.18798392	-0.2581676	14.0
sky00032	Sky	5	5.17973361	-0.2600424	...
sky00029	Sky	16	5.17853588	-0.2629537	...
sky00024	Sky	40	5.18215598	-0.2646898	...
sky00023	Sky	55	5.17733451	-0.2647014	...
sky00012	Sky	60	5.17734032	-0.2676103	...
sky00022	Sky	64	5.17251303	-0.2652890	...
sky00003	Sky	67	5.17915910	-0.2716779	...
sky00008	Sky	72	5.17432527	-0.2687777	...
sky00030	Sky	87	5.16709015	-0.2617984	...
sky00002	Sky	92	5.17312099	-0.2716876	...
sky00011	Sky	93	5.17070516	-0.2676166	...
sky00016	Sky	97	5.16949798	-0.2664531	...
sky00015	Sky	110	5.16768938	-0.2664526	...
sky00001	Sky	118	5.16527065	-0.2716857	...
sky00013	Sky	120	5.16467287	-0.2670314	...
sky00007	Sky	146	5.15923544	-0.2705100	...
sky00018	Sky	162	5.15924853	-0.2658567	...
sky00028	Sky	170	5.16407728	-0.2629585	...
sky00031	Sky	175	5.16347950	-0.2600487	...
sky00027	Sky	177	5.15865512	-0.2629464	...
sky00037	Sky	215	5.15687634	-0.2547967	...
sky00038	Sky	217	5.16950016	-0.2536545	...
sky00051	Sky	241	5.15869512	-0.2495665	...
sky00052	Sky	243	5.15749666	-0.2489813	...
sky00044	Sky	251	5.16469541	-0.2519057	...
sky00045	Sky	253	5.16349477	-0.2513220	...
sky00046	Sky	299	5.16890020	-0.2507456	...
sky00054	Sky	333	5.17610405	-0.2489964	...
sky00041	Sky	344	5.17490850	-0.2530698	...
sky00047	Sky	365	5.18091098	-0.2507315	...

When to observe

NGC 6822 appears in the southern night sky from May through September, when the nights are long. The AAT[4] requires target objects to be $> 30°$ above the horizon throughout observations. The rising and setting times of NGC 6822 at the AAT are shown in Table 3.4, computed using the formulae set out in the following box, and compared with the astronomical dusk and dawn obtained from the AAOmega/AAT website. The last three columns of Table 3.4 show when observations can start and finish and their total duration. To achieve an exposure of 348 minutes, NGC 6822 must be visible for more than 6 hours, which is possible from May 24 2016 until early September. Local time at AAO = universal time (UT) + 10 hrs.

[4]long. 149° 03′ 57.9″ E, lat. −31° 16′ 37.34″

First we calculate the angular distance (HA) from the meridian at the point of rising and setting to the observers meridian, using equation (3.1):

$$\cos \mathrm{HA} = \frac{\sin \mathrm{ALT} - \sin \mathrm{DEC} \times \sin \mathrm{LAT}}{\cos \mathrm{DEC} \times \cos \mathrm{LAT}} \quad \Rightarrow \quad \mathrm{HA} < 63.603^\circ, \text{ for } \mathrm{ALT} > 30^\circ \tag{3.1}$$

The local sidereal time (LST) of the object = Right Ascension (RA) when it transits the local meridian of the observer (LONG (E)). It can be stated in time or degrees. The times of rising and setting in sidereal time (expressed in degrees) are given by equation (3.2)

$$\mathrm{LST} = \begin{cases} \mathrm{RA} - \mathrm{HA} & \Rightarrow \ 232.930^\circ \ : \text{rising} \\ \mathrm{RA} & \Rightarrow \ 296.233^\circ \ : \text{transit} \\ \mathrm{RA} + \mathrm{HA} & \Rightarrow \ 359.836^\circ \ : \text{setting} \end{cases} \tag{3.2}$$

Now we find the corresponding angular distances, (GHA), from the Greenwich meridian to the rising, transit and setting meridians from equation (3.3).

$$\mathrm{GHA} \ = \mathrm{LST} - \mathrm{LONG\ (E)} \tag{3.3}$$

LONG (E) is the easterly longitude of the observatory from the Greenwich meridian. LST and GHA are both sidereal and measured relative to first line of Aries, Υ. Both progress around the clock with respect to solar time at the Greenwich meridian (UT) as the year progresses. We can take account of this by using the Julian Date (JD), as in equation (3.4).

$$\begin{aligned} \mathrm{GST} \ = \mathrm{GHA} - \mathrm{JD}(2000) \times 0.985647 - 100.46 \\ + (\mathrm{Year} - 2000 + 1) \times 360 \end{aligned} \tag{3.4}$$

where JD(2000) = JD - 2451545.0 and is derived from JD by setting JD(2000) = 0 at 12:00:00 on 1st January 2000.[a]. The factor 0.985647 converts JD(2000) to sidereal time and the term -100.46° is the angular distance of the Greenwich meridian from Υ at 12:00:00 01/01/2000. The term $+(\mathrm{Year} - 2000 + 1) \times 360$ takes account of the number of full orbital revolutions which have taken place since 12:00:00 01/01/2000 in order to reduce the result to an angle within 360°.

JD is calculated from equations (3.5) and (3.6) [Murray and Dermott, 1999] (their Appendix 3), as appropriate.

For Months: March to December

$$\begin{aligned} \mathrm{JD} = \mathrm{INT}(365.25 \times \mathrm{Year}) + \mathrm{INT}(30.6001 \times (\mathrm{Month} + 1)) + \mathrm{Day} \\ + \mathrm{INT}(\mathrm{Year}/400) - \mathrm{INT}(\mathrm{Year}/100) + 1720996.5 \end{aligned} \tag{3.5}$$

For Months: January and February

$$\begin{aligned} \mathrm{JD} = \mathrm{INT}(365.25 \times (\mathrm{Year} - 1)) + \mathrm{INT}(30.6001 \times (\mathrm{Month} + 12 + 1)) + \mathrm{Day} \\ + \mathrm{INT}(\mathrm{Year}/400) - \mathrm{INT}(\mathrm{Year}/100) + 1720996.5 \end{aligned} \tag{3.6}$$

The term INT(Year/400) - INT(Year/100) takes accounts of the 10 'lost' days when the calendar changed from 4 October to 15 October in 1582 (i.e. missing out 5-14 October), and the introduction of the leap year system adopted since then.

UT (solar time) is calculated from the GST (sidereal time), using equation (3.7).

$$\mathrm{UT\ [hrs:mins]} = \frac{\mathrm{GST}}{15 + 0.985647/24} \tag{3.7}$$

and finally:

$$\text{Local Time} = \mathrm{UT} + 10 \text{ hrs} \tag{3.8}$$

[a]The Julian calendar is based on a reference epoch of 12.00 noon on 1 January 4713 BCE. The number of days elapsed from this epoch to 12:00:00 01/01/2000 CE is 2451545.0, and the number of days elapsed from this epoch to 00:00:00 01/01/0000 CE is 1720996.5

Table 3.4.: NGC 6822 rising and setting times

2016			Night	Moon	Dusk	Dawn	Rising	Transit	Setting	Start	Finish	Duration (h:m)
May	1	S	1/2		18:49	05:13	00:54	05:08	09:21	00:54	05:13	04:18
May	2	M	2/3		18:48	05:13	00:50	05:04	09:17	00:50	05:13	04:22
May	3	T	3/4		18:48	05:14	00:46	05:00	09:13	00:46	05:14	04:27
May	4	W	4/5		18:47	05:14	00:42	04:56	09:10	00:42	05:14	04:31
May	5	T	5/6		18:46	05:15	00:38	04:52	09:06	00:38	05:15	04:36
May	6	F	6/7	New	18:45	05:16	00:34	04:48	09:02	00:34	05:16	04:41
May	7	S	7/8		18:45	05:16	00:30	04:44	08:58	00:30	05:16	04:45
May	8	S	8/9		18:44	05:17	00:26	04:40	08:54	00:26	05:17	04:50
May	9	M	9/10		18:43	05:17	00:22	04:36	08:50	00:22	05:17	04:54
May	10	T	10/11		18:43	05:18	00:19	04:32	08:46	00:19	05:18	04:58
May	11	W	11/12		18:42	05:18	00:15	04:28	08:42	00:15	05:18	05:02
May	12	T	12/13		18:42	05:19	00:11	04:24	08:38	00:11	05:19	05:07
May	13	F	13/14	First Q	18:41	05:19	00:07	04:20	08:34	00:07	05:19	05:11
May	14	S	14/15		18:41	05:20	00:03	04:17	08:30	00:03	05:20	05:16
May	15	S	15/16		18:40	05:20	23:59	04:13	08:26	23:59	05:20	05:20
May	16	M	16/17		18:40	05:21	23:55	04:09	08:22	23:55	05:21	05:25
May	17	T	17/18		18:39	05:22	23:51	04:05	08:18	23:51	05:22	05:30
May	18	W	18/19		18:39	05:22	23:47	04:01	08:15	23:47	05:22	05:34
May	19	T	19/20		18:38	05:23	23:43	03:57	08:11	23:43	05:23	05:39
May	20	F	20/21		18:38	05:23	23:39	03:53	08:07	23:39	05:23	05:43
May	21	S	21/22	Full	18:37	05:24	23:35	03:49	08:03	23:35	05:24	05:48
May	22	S	22/23		18:37	05:24	23:31	03:45	07:59	23:31	05:24	05:52
May	23	M	23/24		18:37	05:25	23:27	03:41	07:55	23:27	05:25	05:57
May	24	T	24/25		18:36	05:25	23:23	03:37	07:51	23:23	05:25	06:01
May	25	W	25/26		18:36	05:26	23:20	03:33	07:47	23:20	05:26	06:05
May	26	T	26/27		18:36	05:26	23:16	03:29	07:43	23:16	05:26	06:09
May	27	F	27/28		18:36	05:27	23:12	03:25	07:39	23:12	05:27	06:14
May	28	S	28/29		18:35	05:27	23:08	03:21	07:35	23:08	05:27	06:18
May	29	S	29/30	Last Q	18:35	05:28	23:04	03:18	07:31	23:04	05:28	06:23
May	30	M	30/31		18:35	05:28	23:00	03:14	07:27	23:00	05:28	06:27
May	31	T	31/1		18:35	05:28	22:56	03:10	07:23	22:56	05:28	06:31
June	1	W	1/2		18:35	05:29	22:52	03:06	07:19	22:52	05:29	06:36
June	2	T	2/3		18:34	05:29	22:48	03:02	07:16	22:48	05:29	06:40
June	3	F	3/4		18:34	05:30	22:44	02:58	07:12	22:44	05:30	06:45
June	4	S	4/5		18:34	05:30	22:40	02:54	07:08	22:40	05:30	06:49
June	5	S	5/6	New	18:34	05:31	22:36	02:50	07:04	22:36	05:31	06:54
June	6	M	6/7		18:34	05:31	22:32	02:46	07:00	22:32	05:31	06:58
June	7	T	7/8		18:34	05:31	22:28	02:42	06:56	22:28	05:31	07:02
June	8	W	8/9		18:34	05:32	22:25	02:38	06:52	22:25	05:32	07:07
June	9	T	9/10		18:34	05:32	22:21	02:34	06:48	22:21	05:32	07:10
June	10	F	10/11		18:34	05:33	22:17	02:30	06:44	22:17	05:33	07:15
June	11	S	11/12		18:34	05:33	22:13	02:26	06:40	22:13	05:33	07:19
June	12	S	12/13	First Q	18:34	05:33	22:09	02:22	06:36	22:09	05:33	07:23
June	13	M	13/14		18:34	05:34	22:05	02:19	06:32	22:05	05:34	07:28
June	14	T	14/15		18:34	05:34	22:01	02:15	06:28	22:01	05:34	07:32
June	15	W	15/16		18:35	05:34	21:57	02:11	06:24	21:57	05:34	07:36
June	16	T	16/17		18:35	05:34	21:53	02:07	06:20	21:53	05:34	07:40
June	17	F	17/18		18:35	05:35	21:49	02:03	06:17	21:49	05:35	07:45
June	18	S	18/19		18:35	05:35	21:45	01:59	06:13	21:45	05:35	07:49
June	19	S	19/20		18:35	05:35	21:41	01:55	06:09	21:41	05:35	07:53
June	20	M	20/21	Full	18:35	05:35	21:37	01:51	06:05	21:37	05:35	07:57
June	21	T	21/22		18:36	05:36	21:33	01:47	06:01	21:33	05:36	08:02
June	22	W	22/23		18:36	05:36	21:29	01:43	05:57	21:29	05:36	08:06
June	23	T	23/24		18:36	05:36	21:26	01:39	05:53	21:26	05:36	08:09
June	24	F	24/25		18:36	05:36	21:22	01:35	05:49	21:22	05:36	08:13
June	25	S	25/26		18:37	05:36	21:18	01:31	05:45	21:18	05:36	08:17
June	26	S	26/27		18:37	05:36	21:14	01:27	05:41	21:14	05:36	08:21
June	27	M	27/28		18:37	05:37	21:10	01:24	05:37	21:10	05:37	08:26
June	28	T	28/29	Last Q	18:38	05:37	21:06	01:20	05:33	21:06	05:33	08:27
June	29	W	29/30		18:38	05:37	21:02	01:16	05:29	21:02	05:29	08:27
June	30	T	31/1		18:38	05:37	20:58	01:12	05:25	20:58	05:25	08:27

Continued on next page

Table 3.4 (cont.) NGC 6822 rising and setting times

2016			Night	Moon	Dusk	Dawn	Rising	Transit	Setting	Start	Finish	Duration (h:m)
July	1	F	1/2		18:38	05:37	20:54	01:08	05:22	20:54	05:22	08:27
July	2	S	2/3		18:39	05:37	20:50	01:04	05:18	20:50	05:18	08:27
July	3	S	3/4		18:39	05:37	20:46	01:00	05:14	20:46	05:14	08:27
July	4	M	4/5	New	18:40	05:37	20:42	00:56	05:10	20:42	05:10	08:27
July	5	T	5/6		18:40	05:37	20:38	00:52	05:06	20:38	05:06	08:27
July	6	W	6/7		18:40	05:37	20:34	00:48	05:02	20:34	05:02	08:27
July	7	T	7/8		18:41	05:37	20:30	00:44	04:58	20:30	04:58	08:27
July	8	F	8/9		18:41	05:36	20:27	00:40	04:54	20:27	04:54	08:27
July	9	S	9/10		18:41	05:36	20:23	00:36	04:50	20:23	04:50	08:27
July	10	S	10/11		18:42	05:36	20:19	00:32	04:46	20:19	04:46	08:27
July	11	M	11/12		18:42	05:36	20:15	00:28	04:42	20:15	04:42	08:27
July	12	T	12/13	First Q	18:43	05:36	20:11	00:25	04:38	20:11	04:38	08:27
July	13	W	13/14		18:43	05:36	20:07	00:21	04:34	20:07	04:34	08:27
July	14	T	14/15		18:44	05:35	20:03	00:17	04:30	20:03	04:30	08:27
July	15	F	15/16		18:44	05:35	19:59	00:13	04:26	19:59	04:26	08:27
July	16	S	16/17		18:45	05:35	19:55	00:09	04:23	19:55	04:23	08:27
July	17	S	17/18		18:45	05:34	19:51	00:05	04:19	19:51	04:19	08:27
July	18	M	18/19		18:45	05:34	19:47	00:01	04:15	19:47	04:15	08:27
July	19	T	19/20		18:46	05:34	19:43	23:57	04:11	19:43	04:11	08:27
July	20	W	20/21	Full	18:46	05:33	19:39	23:53	04:07	19:39	04:07	08:27
July	21	T	21/22		18:47	05:33	19:35	23:49	04:03	19:35	04:03	08:27
July	22	F	22/23		18:47	05:33	19:32	23:45	03:59	19:32	03:59	08:27
July	23	S	23/24		18:48	05:32	19:28	23:41	03:55	19:28	03:55	08:27
July	24	S	24/25		18:48	05:32	19:24	23:37	03:51	19:24	03:51	08:27
July	25	M	25/26		18:49	05:31	19:20	23:33	03:47	19:20	03:47	08:27
July	26	T	26/27		18:49	05:31	19:16	23:29	03:43	19:16	03:43	08:27
July	27	W	27/28	Last Q	18:50	05:30	19:12	23:26	03:39	19:12	03:39	08:27
July	28	T	28/29		18:50	05:30	19:08	23:22	03:35	19:08	03:35	08:27
July	29	F	29/30		18:51	05:29	19:04	23:18	03:31	19:04	03:31	08:27
July	30	S	30/31		18:51	05:29	19:00	23:14	03:27	19:00	03:27	08:27
July	31	S	31/1		18:51	05:28	18:56	23:10	03:24	18:56	03:24	08:27
August	1	M	1/2		18:52	05:27	18:52	23:06	03:20	18:52	03:20	08:27
August	2	T	2/3		18:53	05:27	18:48	23:02	03:16	18:53	03:16	08:23
August	3	W	3/4	New	18:53	05:26	18:44	22:58	03:12	18:53	03:12	08:19
August	4	T	4/5		18:54	05:25	18:40	22:54	03:08	18:54	03:08	08:14
August	5	F	5/6		18:54	05:24	18:36	22:50	03:04	18:54	03:04	08:10
August	6	S	6/7		18:55	05:24	18:33	22:46	03:00	18:55	03:00	08:05
August	7	S	7/8		18:55	05:23	18:29	22:42	02:56	18:55	02:56	08:01
August	8	M	8/9		18:56	05:22	18:25	22:38	02:52	18:56	02:52	07:56
August	9	T	9/10		18:56	05:21	18:21	22:34	02:48	18:56	02:48	07:52
August	10	W	10/11		18:57	05:21	18:17	22:31	02:44	18:57	02:44	07:47
August	11	T	11/12	First Q	18:57	05:20	18:13	22:27	02:40	18:57	02:40	07:43
August	12	F	12/13		18:58	05:19	18:09	22:23	02:36	18:58	02:36	07:38
August	13	S	13/14		18:58	05:18	18:05	22:19	02:32	18:58	02:32	07:34
August	14	S	14/15		18:59	05:17	18:01	22:15	02:29	18:59	02:29	07:30
August	15	M	15/16		18:59	05:16	17:57	22:11	02:25	18:59	02:25	07:26
August	16	T	16/17		19:00	05:15	17:53	22:07	02:21	19:00	02:21	07:21
August	17	W	17/18		19:00	05:14	17:49	22:03	02:17	19:00	02:17	07:17
August	18	T	18/19		19:01	05:13	17:45	21:59	02:13	19:01	02:13	07:12
August	19	F	19/20	Full	19:01	05:12	17:41	21:55	02:09	19:01	02:09	07:08
August	20	S	20/21		19:02	05:11	17:37	21:51	02:05	19:02	02:05	07:03
August	21	S	21/22		19:02	05:10	17:34	21:47	02:01	19:02	02:01	06:59
August	22	M	22/23		19:03	05:09	17:30	21:43	01:57	19:03	01:57	06:54
August	23	T	23/24		19:04	05:08	17:26	21:39	01:53	19:04	01:53	06:49
August	24	W	24/25		19:04	05:07	17:22	21:35	01:49	19:04	01:49	06:45
August	25	T	25/26		19:05	05:06	17:18	21:32	01:45	19:05	01:45	06:40
August	26	F	26/27	Last Q	19:05	05:05	17:14	21:28	01:41	19:05	01:41	06:36
August	27	S	27/28		19:06	05:04	17:10	21:24	01:37	19:06	01:37	06:31
August	28	S	28/29		19:06	05:03	17:06	21:20	01:33	19:06	01:33	06:27
August	29	M	29/30		19:07	05:02	17:02	21:16	01:30	19:07	01:30	06:23
August	30	T	30/31		19:07	05:00	16:58	21:12	01:26	19:07	01:26	06:19
August	31	W	31/1	New	19:08	04:59	16:54	21:08	01:22	19:08	01:22	06:14

3.2. Galaxy Dynamic Mass

The dynamical mass of NGC 6822 is not well constrained at present. McConnachie [2012] gives a value of $100 \times 10^6\ M_\odot$ based on a putative mass-to-light ratio of $1\Upsilon_\odot$ and Mateo [1998] gives a value of $1640 \times 10^6\ M_\odot$ with a $\Upsilon = 17\ \Upsilon_\odot$. Weldrake et al. [2003] estimates of the baryonic mass of NGC 6822 of $2.8 \times 10^8\ M_\odot$ with individual contributions from its stellar content of $1.3 \times 10^8\ M_\odot$ (at $\Upsilon_{\text{stellar}} = 0.35$), and from its gas content of $1.5 \times 10^8\ M_\odot$, by selecting suitable halo models (for the stars and the gas) and finding the best fits of the velocity/radius combinations to the measured rotation curves. Weldrake et al. [2003] compares this with a dark halo mass estimated at $5.2 \times 10^{10}\ M_\odot$.

A simple approach to measuring the dynamical mass could assume that a test particle orbits the galaxy centre in circular orbit, of radius r, at a velocity v_c, and that the galaxy is an isotropic mass, which can be considered as a Newtonian central point source. The mass enclosed by the orbit, M_{enc}, is then given by equation (3.9).

$$M_{\text{enc}} = \frac{r}{G}\, v_c^2 \;\approx\; 2.326 \times \frac{R}{[\text{kpc}]} \times \frac{V_c^2}{[\text{km s}^{-1}]^2} \times 10^5\ \ [M_\odot] \tag{3.9}$$

where $G \approx 4.300 \times 10^{-6}$ kpc ${M_\odot}^{-1}$ (km s^{-1})^2. V_c is the circular velocity of a star in km s^{-1}, moving in a circular orbit of radius R in kpc.

If we let V_c of the test particle be equal to the rotation velocity calculated in §2.4.3, $V_{\text{rot}} = 11.3$ km s^{-1}, and using the mean distance, 1.1 kpc, of the inner population of C-type stars in the sample from the galaxy centre, see §2.5, as the corresponding orbital radius R of the test particle then, using equation (3.9), the dynamical mass enclosed $M_{\text{enc}} \sim 40 \times 10^6\ M_\odot$.

This treatment is a great oversimplification. Firstly, the kinematic assumption is too simple. The carbon stars in NGC 6822 form a pressure supported spheroid, and hence the rotation velocity of the C-star population significantly underestimates that of a rotationally supported orbit. Secondly, there is no attempt to de-project the measured radial velocities into orbital velocities about the galaxy centre, and thirdly, the mass distribution in NGC 6822 is too simple. The mass derived must therefore be considered a lower limit that underestimates the mass by a factor of a few. The HI disk, which is rotationally supported, is able to provide more reliable mass estimates [Weldrake et al., 2003].

Dynamical modelling of the AGB population would enable the galaxy mass to be estimated from the stellar rotation velocities measured, but this is a complicated procedure. The theory is covered in detail in Binney and Tremaine [2008] and Sparke

and Gallagher [2007] but the practicality of implementing the theory on NGC 6822 is not trivial and extends beyond the scope of this MPhil thesis.

Mateo [1998] suggests using the King method [Richstone and Tremaine, 1986] which adopts the formula in equation (3.10), to calculate the mass-to light ratio for a chosen halo model given the radial velocity dispersion profile, $\sigma(r)$, spectroscopically obtained, the surface brightness profile, $I(r)$, photometrically obtained, and the half-light radius, $R_{\rm h}$.

$$\frac{\mathcal{M}}{\mathcal{L}} = \eta \frac{9\sigma^2(0)}{2\pi G I(0) R_{\rm h}} \tag{3.10}$$

Equation (3.10) is derived from the Virial Theorem [Sparke and Gallagher, 2007] and is valid for galaxies where the stellar orbits are non-circular. The velocity dispersion is given by $\sigma^2 = \langle (v_r - \bar{v}_r)^2 \rangle$, where v_r are the stellar radial velocities and $\bar{v}_r$ is the mean galactic velocity. For many halo models, the constant of proportionality $\eta \approx 1$ [Richstone and Tremaine, 1986], but this is not so in all cases, so care must be taken. In the Plummer model for instance, $\eta \approx 2.6$ [Sparke and Gallagher, 2007].

Although my summary results include values for $\sigma(V_{\rm helio})$, see Table 2.3 column [5], they are not appropriate as an estimate of σ in equation (3.10), since they are dominated by the measurement errors $\langle V_{\rm err} \rangle$ in column [4] of the table. The new observations proposed in §3.1 will reduce $\langle V_{\rm err} \rangle$ and may yield sufficient accuracy for the mass-to light ratio to be estimated.

A number of halo models can give the gravitational potential, $\nabla\Phi$, of a galaxy depending on its morphology, and which could enable a better means to dynamically model the galaxy and to determine its dynamical mass. Some of these are listed below. Together with others, they are described in detail in Binney and Tremaine [2008]. For NGC 6822, the chosen halo will need to take account of the central core, the gas disk, the outer halo of RGBs/AGBs and a putative dark matter halo. The stellar halo will need to be able to cater for ellipsoidal density distributions in the core and RGB/AGB population, rather than spherical. King models have been used in the past [Hodge et al., 1991, Mateo, 1998] which have enough degrees of freedom to enable a wide variation in morphologies. Weldrake et al. [2003] uses an isothermal density profile, where the circular speeds are constant at all radii, for the stellar population, a Navarro-Frenk-White (NFW) for the dark matter halo and a thin disk approximation for the gas disk. The choice of the relevant halo will be an important feature in the further development of this topic.

Halo Models

Dynamical frameworks for future theoretical studies of the rotation in NGC 6822 could be chosen from the following halo models. The models are fully explained, with equations, in Binney and Tremaine [2008].

- **Plummer model**. This is a simple model for the potential of spherical systems and is unsuitable for ellipsoidal density halos.
- **Isothermal model**. This is similar to the Plummer model, adding an extra degree of freedom, and is useful where the velocities are constant over a wide radius.
- **King models**. These comprise a suite of models which provide flexibility by using three variable scale parameters applicable to a wider range of galactic shapes, including elliptical galaxies. King models are based on empirical data [King, 1962] and evolved over a long history [Richstone and Tremaine, 1986].
- **Density Models for Dark Matter Halos**. It has long been established that the kinematics of galaxies is dominated by dark matter. Dark matter halos can only be inferred by indirect means or simulation. A generalised version of the density model is given in Binney and Tremaine [2008] [their equation (2.64)]. This model has a number of forms but the most common form used for dark matter halos is the Navarro-Frenk-White (NFW) Model.

  The cusp at the centre of the NFW halo, where density $\rho \to \infty$ as the radius r from the centre reduces, see equation (1.1), has motivated considerable effort to understand if it is real, or if some physical mechanisms come into force to eliminate it. In Di Cintio et al. [2014], the NFW model is modified to remove the central cusp by the introduction of baryonic feedback mechanisms .
- **Disk potentials**. There are many variants of disk models which could apply to the gas disk. Weldrake et al. [2003] adopted a thin disk.

With the additional data proposed in §3.1, and more detailed dynamical modelling as introduced in §3.2, it would be possible to investigate further the structure or kinematics of the outer halo of NGC 6822, the mass profile of the galaxy and what these tell us about the structure and history of the brightest isolated dIrr galaxy.

4. Conclusions

This dissertation is the conclusion of three years of study into the kinematics of NGC 6822. The study used spectra taken for spectroscopic classification purposes over a wide band with low resolution. Moreover the exposure times were short and the *SNR* was low. Originally intended to be a familiarisation with spectral analysis, and not ideally suited to radial velocity measurements, I quickly found that using *IRAF* I was able to obtain reasonable radial velocity measurements from the spectra. The radial velocities I measured were close to other published sources and is one of only a small number of stellar based measurements of this kind. Moreover, I discovered a rotational signal in the data and refined the study to look at this in some detail. Demers et al. [2006] has suggested that NGC 6822 is a polar ring galaxy based on the measured radial velocities of of ~ 110 stars lying about a putative rotation axis lying along the major axis of the AGB stellar distribution. The Demers et al. [2006] result is often cited. My results show that this is not the case and that the galaxy rotates in coincidence with the HI disk. This result has been submitted for publication to MNRAS. The rotational signature of NGC 6822 was an unexpected discovery.

The second part of the study provides descriptions of two pieces of future work. The first is to extend the observations to a greater number of carbon stars lying within the isophotes, and repeat the measurements with greater spectral resolving power and better *SNR*. The second part is to undertake a theoretical study of the gravitational potential of NGC 6822 and to attempt to constrain its dynamical mass. This may lead to further discoveries of its dark matter content.

Finally, perhaps there is also something to be discovered by examining the kinematics of bright dwarf irregular galaxies close to the edge to the LG, where most are located, to seek out any signature of the interaction between gravitational forces and Hubble flow.

Appendices

A. Error formulae

A.1. Cosmological parameters error combination

The Planck cosmological parameters Ω_c and Ω_b are derived from the terms for $\Omega_c h^2$ and $\Omega_b h^2$ provided in Table 3 of Planck Collaboration et al. [2014b], where $h = H_0/100$. The values for Ω_c and Ω_b, and their errors $\pm\Delta\Omega_c$ and $\pm\Delta\Omega_b$, are computed by expanding $(\Omega \pm \Delta\Omega)(h \pm \Delta h)^2$ and dividing by h^2 to give:

$$\Omega \pm (2h\Omega\Delta h + \Omega\Delta h^2 + \Delta\Omega h^2 + 2h\Delta\Omega\Delta h + \Delta\Omega\Delta h^2)/h^2$$

A.2. Distance error, $\Delta(D)$

The formula used to determine the distance errors, $\Delta(D)$, from distance moduli, $(m-M)_0$, is $\Delta(D) = 0.46052\ \Delta(m-M)_0$ kpc. $\Delta(m-M)_0$ is the error in the distance modulus and D is the distance in kpc to the object. $D = 10^{\left(1+\frac{(m-M)}{5}\right)}$ kpc.

This expression is derived as follows:

$$\Delta \ln(x) \approx \frac{\Delta(x)}{x} \Rightarrow \Delta \log_{10}(x) \approx \frac{\Delta(x)}{x}.\frac{1}{\ln(10)} = 0.43429\ \frac{\Delta(x)}{x}$$

$$(m-M)_0 = 5\log_{10}(D) - 5 \Rightarrow \Delta(m-M)_0 = \Delta(5\log_{10}(D) - 5)$$

$$\text{So } \Delta(m-M)_0 \Rightarrow 5\,\Delta(\log_{10}(D) - 1) = 5\,\Delta\log_{10}\left(\frac{D}{10}\right), \text{ where } D \text{ is in pc}$$

Let $x = D/10$, rearranging we get

$$\Rightarrow \frac{\Delta(m-M)_0}{5} = \Delta\log_{10}(x) = 0.43429\ \frac{\Delta(x)}{x}$$

$$\Rightarrow \frac{\Delta(x)}{x} = \frac{1}{0.43429}\frac{\Delta(m-M)_0}{5} = 0.46052\,\Delta(m-M)_0$$

$$\text{and } \Rightarrow \Delta(x) = 0.46052\,\Delta(m-M)_0\,x$$

now $\Delta(x) = \Delta(D/10) = \Delta(D)/10$ and $x = D/10$, so

$$\Delta(D) = 0.46052.\Delta(m-M)_0.D, \text{ where } D = 10^{\left(1+\frac{(m-M)}{5}\right)}$$

A.3. Velocity error, ΔV_{rot}

The formula used for ΔV_{rot} is as follows:

$$\Delta V_{\mathrm{rot}} = \left\{ \frac{1}{360} \sum_{i=1}^{360} (\hat{y}_i - y_i)^2 \right\}^{\frac{1}{2}} \tag{A.1}$$

A.4. Position angle error, ΔPA

The formula used for ΔPA is as follows:

$$\Delta PA = \left\{ \frac{1}{360} \sum_{i=1}^{360} (\hat{\theta}_i - \theta_i)^2 \right\}^{\frac{1}{2}} \tag{A.2}$$

θ_i is incremented in 1° steps and for each increment the mean bin velocity, v_i, is taken. By setting $\hat{y}_i = v_i$ in equation (A.3), $\hat{\theta}_i$ is found.

$$\hat{\theta}_i = PA \pm \arcsin \left\{ \frac{\hat{y}_i - y_0}{V_{\mathrm{rot}}} \right\} \quad \text{the sign depends upon the quadrant} \tag{A.3}$$

which is derived from the equation $\hat{y} = V_{\mathrm{rot}} \sin(\theta - \theta_0) + y_0$, and where $\theta_0 = PA$ and y_0 is the offset, and V_{rot} is the overall computed rotation velocity of the galaxy.

B. Full Radial Velocity Results

Appendix B - Full radial velocity results for each object
Objects meeting the criteria ($hght \geqslant 0.2$, -200 km s$^{-1} \leqslant V_{\rm helio} \leqslant +200$ km s^{-1}).

[1]	[2]	[3]	[4]	[5]	[6]	[7]	[8]	[9]	[10]	[11]	[12]	[13]	[14]	[15]	[16]
							30 August 2011				31 August 2011				
#Fibre	ID	RA (°)	Dec (°)	distance (kpc)	phot. class.	spec. class.	*SNR*	*hght*	$V_{\rm helio}$ (km s^{-1})	$V_{\rm err}$ (km s^{-1})	*SNR*	*hght*	$V_{\rm helio}$ (km s^{-1})	$V_{\rm err}$ (km s^{-1})	Flag
1	217716	296.2348	-14.8626	0.52	M	Ce:	7	0.39	-10	49	9	0.48	-35	36	C
2	239630	296.3325	-14.9511	1.52	C*	C:	6	0.43	-55	41	7	0.54	-55	27	C
3	210316	296.4344	-14.8347	1.69	M	C:	5	0.59	15	25	6	0.76	-11	16	C
4	174035	296.3740	-14.7111	1.40	M*	C	3	0.37	-26	57	5	0.27	-43	67	C
6	199974	296.3748	-14.7981	1.17	M	C	...	...	...	...	9	0.65	4	24	C
7	194949	296.3522	-14.7807	1.00	C*	C:	12	0.72	-1	34	18	0.75	-14	23	C
8	242030	296.3458	-14.9601	1.64	...	...	6	0.60	-53	21	9	0.70	-62	22	...
9	220271	296.3905	-14.8726	1.43	...	...	5	0.48	-28	40	8	0.59	-63	27	...
10	188246	296.4855	-14.7568	2.12	M	C:	6	0.57	-40	29	10	0.80	-39	16	C
11	172656	296.5396	-14.7050	2.66	C*	C	5	0.29	-125	69	8	0.39	-70	41	C
12	211898	296.3085	-14.8405	0.70	M	C	9	0.57	-31	26	7	0.74	-21	20	C
14	246838	296.5442	-14.9802	2.99	...	...	4	0.36	-78	37	5	0.57	-61	28	...
15	206867	296.3018	-14.8222	0.59	...	...	7	0.42	1	58	8	0.42	-3	38	...
17	225812	296.3179	-14.8952	1.06	...	...	4	0.33	-0	75	6	0.51	-10	31	...
18	190283	296.3428	-14.7641	0.96	M	C	6	0.45	-44	33	5	0.36	-51	36	C
19	168284	296.4114	-14.6857	1.78	C*	C:	9	0.48	40	42	10	0.48	21	34	C
21	213379	296.2415	-14.8462	0.39	C*	Ce:	4	0.40	-25	42	...	...	...	...	C
22	200573	296.2741	-14.8002	0.34	M	Ce	8	0.37	10	73	9	0.72	-12	17	C
23	219598	296.2972	-14.8699	0.79	C*	C	6	0.36	-94	77	10	0.48	-62	52	C
24	203106	296.3382	-14.8089	0.87	C*	C:	7	0.64	-31	30	9	0.68	-35	21	C
25	209216	296.2331	-14.8307	0.25	M	Ce	...	...	...	...	12	0.64	-11	21	C
26	197590	296.3195	-14.7898	0.72	C*	M:	22	0.68	-9	43	9	0.45	-28	63	...
28	197464	296.2834	-14.7894	0.43	M	C	7	0.48	-80	47	9	0.70	-58	30	C
29	206129	296.2390	-14.8196	0.16	M	dKe:	12	0.60	-32	39	12	0.54	-23	49	...
31	180514	296.3759	-14.7309	1.33	M	C	10	0.83	-40	15	11	0.89	-36	16	C
32	191382	296.3046	-14.7679	0.66	M*	C	6	0.50	0	28	8	0.51	-25	22	C
33	306281	297.0555	-15.2739	7.90	...	...	4	0.26	148	63	...	...	...	...	...

Continued on next page

Appendix B (cont.): Objects meeting the criteria ($hght \geqslant 0.2$, -200 km s$^{-1} \leqslant V_{\rm helio} \leqslant +200$ km s^{-1}).

[1]	[2]	[3]	[4]	[5]	[6]	[7]	[8]	[9]	[10]	[11]	[12]	[13]	[14]	[15]	[16]
							30 August 2011				31 August 2011				
#Fibre	ID	RA (°)	Dec (°)	distance (kpc)	phot. class.	spec. class.	*SNR*	*hght*	$V_{\rm helio}$ (km s^{-1})	$V_{\rm err}$ (km s^{-1})	*SNR*	*hght*	$V_{\rm helio}$ (km s^{-1})	$V_{\rm err}$ (km s^{-1})	Flag
34	294767	296.9917	-15.2147	7.19	...	...	5	0.23	149	92	...	...	...	...	...
36	292760	296.7679	-15.2044	5.60	M	dM	23	0.57	5	50	48	0.61	7	51	M
38	218420	296.3646	-14.8653	1.21	C*	C	7	0.43	-25	26	7	0.32	-52	73	C
41	324220	297.0105	-15.3591	8.00	...	...	1	0.21	-6	26	...	...	...	...	...
43	229856	296.3681	-14.9132	1.47	C*	C	...	...	...	...	8	0.52	-31	31	C
45	201454	296.2513	-14.8031	0.15	C*	Ce:	16	0.58	-21	45	21	0.66	-45	36	C
47	291854	296.8191	-15.1996	5.92	...	...	...	...	...	...	5	0.30	80	51	...
48	184448	296.4366	-14.7439	1.75	M*	C	4	0.30	-30	48	7	0.31	-6	38	C
49	335226	296.9187	-15.4082	7.68	...	...	5	0.31	-156	63	7	0.26	2	69	...
51	341622	296.8634	-15.4414	7.55	...	...	4	0.23	71	106	...	...	...	...	...
52	342923	296.8514	-15.4482	7.52	...	...	2	0.28	33	60	...	...	...	...	...
53	248633	296.3380	-14.9886	1.82	C*	C:	6	0.46	-17	46	7	0.47	-51	38	C
54	229643	296.3538	-14.9124	1.37	C*	C	8	0.64	-55	24	10	0.71	-43	23	C
56	351371	296.8376	-15.4925	7.73	...	...	3	0.28	58	138	...	...	...	...	...
57	186954	296.4692	-14.7522	2.00	Unid*	dK	4	0.24	192	76	4	0.22	-35	65	...
58	249091	296.3913	-14.9908	2.08	...	...	7	0.47	-86	20	7	0.44	-38	46	...
62	299244	296.6764	-15.2377	5.22	...	...	...	...	...	...	4	0.28	19	62	...
65	220153	296.2369	-14.8721	0.60	M	Ce	9	0.31	-28	101	8	0.59	-2	31	C
68	240673	296.0613	-14.9551	1.93	M*	C	3	0.31	-52	66	4	0.36	-46	64	C
69	310311	296.6016	-15.2943	5.20	...	...	4	0.37	-178	72	6	0.33	-32	68	...
70	237395	296.0707	-14.9435	1.81	Unid*	C	3	0.26	-32	133	...	...	...	...	C
71	228306	296.2510	-14.9064	0.91	M	Ce	5	0.39	-33	61	6	0.56	-38	29	C
73	337540	296.5005	-15.4207	5.74	...	...	3	0.30	9	84	...	...	...	...	...
75	223056	296.2613	-14.8837	0.74	M	Ce	6	0.42	-59	55	9	0.33	-55	52	C
76	237999	296.0890	-14.9455	1.71	C*	C	4	0.24	-110	37	5	0.48	-67	27	C
78	220391	296.2125	-14.8731	0.63	...	...	9	0.64	-24	33	11	0.66	-26	30	...
80	231793	296.2240	-14.9224	1.04	C*	C	4	0.50	-80	57	9	0.79	-39	21	C
81	219171	296.2251	-14.8682	0.57	...	...	7	0.46	-79	36	8	0.72	-61	17	...
82	343626	296.3798	-15.4518	5.69	...	...	4	0.49	-72	24	...	...	...	...	...

Continued on next page

Appendix B (cont.): Objects meeting the criteria ($hght \geqslant 0.2$, -200 km s$^{-1} \leqslant V_{\rm helio} \leqslant +200$ km s^{-1}).

[1]	[2]	[3]	[4]	[5]	[6]	[7]	[8]	[9]	[10]	[11]	[12]	[13]	[14]	[15]	[16]
							30 August 2011				31 August 2011				
#Fibre	ID	RA (°)	Dec (°)	distance (kpc)	phot. class.	spec. class.	*SNR*	*hght*	$V_{\rm helio}$ (km s^{-1})	$V_{\rm err}$ (km s^{-1})	*SNR*	*hght*	$V_{\rm helio}$ (km s^{-1})	$V_{\rm err}$ (km s^{-1})	Flag
83	343571	296.4387	-15.4516	5.81	...	...	...	...	...	...	6	0.42	71	56	...
84	248651	296.2813	-14.9887	1.65	...	...	7	0.63	-43	29	10	0.85	-56	14	...
85	208620	296.1007	-14.8285	1.12	M	C	11	0.80	-68	23	11	0.85	-66	17	C
86	219351	296.2825	-14.8689	0.70	M	Ce	7	0.52	-60	47	9	0.76	-38	22	C
88	226097	296.2075	-14.8964	0.84	M	C	5	0.53	-53	27	5	0.65	-29	21	C
90	215861	296.1738	-14.8556	0.67	M	Ce	5	0.50	-22	37	6	0.50	-13	26	C
91	250173	296.2154	-14.9960	1.67	Unid*	C	6	0.39	-55	58	4	0.44	-8	29	C
94	225648	296.1631	-14.8945	0.98	C*	C	11	0.84	-27	14	9	0.86	-33	16	C
95	242563	296.1837	-14.9621	1.43	C*	C	7	0.41	-41	58	9	0.64	-77	25	C
96	208714	296.1830	-14.8289	0.48	M	Ce	8	0.64	-29	22	11	0.74	-35	17	C
98	226603	296.1186	-14.8987	1.26	M	C	6	0.65	-65	24	7	0.71	-74	23	C
99	330842	296.3425	-15.3862	5.08	M	dM	3	0.32	-46	62	7	0.32	24	62	M
101	220672	296.1067	-14.8742	1.22	...	...	3	0.36	-18	41	5	0.49	-1	35	...
102	344297	296.1232	-15.4552	5.66	M	dM	5	0.35	85	56	12	0.52	16	46	M
104	209650	296.1298	-14.8323	0.90	M	C	6	0.37	-51	33	7	0.35	-51	39	C
105	233186	296.1578	-14.9291	1.26	Unid*	Unid	19	0.52	39	42	17	0.71	-39	26	...
106	344467	296.1823	-15.4562	5.61	M	dK	7	0.48	-40	33	15	0.61	-14	44	...
107	351774	296.1202	-15.4946	6.00	...	...	3	0.29	16	55	6	0.53	-62	30	...
112	253239	296.0905	-15.0101	2.14	C*	C	3	0.35	-32	26	4	0.49	-40	24	C
113	199754	296.2082	-14.7973	0.21	C*	Ce	10	0.50	-92	54	8	0.67	-45	21	C
115	339686	296.0855	-15.4313	5.52	...	...	4	0.31	-100	52	...	...	...	...	...
116	326339	295.9452	-15.3703	5.41	...	...	4	0.29	-94	75	4	0.46	24	48	...
119	207586	296.2125	-14.8249	0.26	M	C	11	0.60	-72	35	8	0.60	-61	32	C
122	223739	296.1536	-14.8867	0.98	M	C	5	0.50	-40	36	7	0.44	-4	71	C
123	199930	296.2364	-14.7979	0.04	...	...	14	0.78	-83	26	14	0.78	-56	23	...
124	239687	296.0345	-14.9513	2.08	M*	C	7	0.40	-15	54	5	0.65	-67	20	C
125	216688	296.0804	-14.8587	1.36	M*	C:	16	0.74	-22	18	14	0.75	-64	21	C
126	327377	296.0117	-15.3746	5.23	M	dK	6	0.43	-2	45	8	0.31	-9	86	...
128	317678	295.9490	-15.3295	5.09	M	dM:	5	0.23	-3	60	9	0.35	17	72	M

Continued on next page

Appendix B (cont.): Objects meeting the criteria ($hght \geqslant 0.2$, -200 km s$^{-1} \leqslant V_{\rm helio} \leqslant +200$ km s^{-1}).

[1]	[2]	[3]	[4]	[5]	[6]	[7]	[8]	[9]	[10]	[11]	[12]	[13]	[14]	[15]	[16]
							30 August 2011				31 August 2011				
#Fibre	ID	RA (°)	Dec (°)	distance (kpc)	phot. class.	spec. class.	*SNR*	*hght*	$V_{\rm helio}$ (km s^{-1})	$V_{\rm err}$ (km s^{-1})	*SNR*	*hght*	$V_{\rm helio}$ (km s^{-1})	$V_{\rm err}$ (km s^{-1})	Flag
129	337831	295.9231	-15.4220	5.89	M	dK	4	0.37	30	36	7	0.39	36	66	...
130	313097	295.8791	-15.3090	5.23	M	dK	6	0.34	-62	114	12	0.48	-11	57	...
131	355390	295.7730	-15.5140	7.18	M	dM:	...	...	...	...	11	0.38	45	185	M
132	300999	295.8370	-15.2467	5.02	...	...	...	...	...	...	5	0.23	-155	63	...
133	372253	295.7961	-15.5937	7.68	M	dK	7	0.35	30	115	8	0.41	70	68	...
134	317557	295.7940	-15.3291	5.79	M	dK:	5	0.49	6	52	7	0.41	16	80	...
135	303607	295.8101	-15.2604	5.25	M	dM	...	...	...	...	7	0.39	26	94	M
136	222468	296.0965	-14.8814	1.32	M	C	4	0.47	-105	31	7	0.59	-28	39	C
137	299996	295.7770	-15.2414	5.32	M	C:	3	0.42	-46	32	5	0.53	-67	38	...
138	297583	295.7998	-15.2294	5.12	M	dM	8	0.44	-7	59	16	0.57	58	57	M
139	303122	295.7434	-15.2578	5.62	M	dM	...	...	...	...	7	0.59	15	41	M
141	310841	295.7774	-15.2973	5.67	...	...	...	...	...	...	8	0.46	-54	51	...
142	309370	295.8729	-15.2897	5.13	M	dM	8	0.37	31	63	...	...	...	...	M
145	350411	295.5879	-15.4876	7.93	M	dK	5	0.24	26	103	8	0.48	-51	53	...
147	340026	295.6209	-15.4331	7.40	...	...	4	0.23	52	77	4	0.26	-92	169	...
148	276398	295.7205	-15.1256	5.06	C	C:	5	0.36	-132	46	9	0.65	-111	26	...
149	332677	295.6490	-15.3953	7.00	M	dM:	5	0.35	-15	28	10	0.42	-29	50	M
152	336076	295.5172	-15.4125	7.89	...	...	3	0.30	-79	36	5	0.46	-39	56	...
153	337060	295.5954	-15.4181	7.45	...	...	3	0.26	-73	76	7	0.39	73	86	...
154	282194	295.6896	-15.1551	5.41	...	...	2	0.41	-27	72	4	0.39	-68	28	...
155	332908	295.5222	-15.3965	7.77	...	...	4	0.44	-38	31	5	0.38	11	76	...
156	329347	295.5168	-15.3809	7.72	M	dM:	7	0.36	12	53	12	0.55	-47	47	M
157	324005	295.5370	-15.3580	7.46	M	dM:	...	...	...	...	9	0.47	-82	46	M
158	312062	295.5349	-15.3035	7.19	M	dM:	8	0.40	-20	51	15	0.53	-16	60	M
159	318572	295.5762	-15.3334	7.08	M	dK	10	0.54	-19	52	15	0.61	-15	33	...
160	312215	295.4992	-15.3044	7.43	M	dK	...	...	...	...	10	0.31	-9	94	...
161	301044	295.4803	-15.2470	7.29	...	...	...	...	...	...	1	0.31	-171	36	...
163	298121	295.4782	-15.2320	7.24	M	dM:	...	...	...	...	8	0.38	81	68	M
164	305736	295.4917	-15.2713	7.32	M	dK	...	...	...	...	11	0.34	-19	89	...

Continued on next page

Appendix B (cont.): Objects meeting the criteria ($hght \geqslant 0.2$, -200 km s$^{-1} \leqslant V_{\rm helio} \leqslant +200$ km s^{-1}).

[1]	[2]	[3]	[4]	[5]	[6]	[7]	[8]	[9]	[10]	[11]	[12]	[13]	[14]	[15]	[16]
							30 August 2011				31 August 2011				
#Fibre	ID	RA (°)	Dec (°)	distance (kpc)	phot. class.	spec. class.	*SNR*	*hght*	$V_{\rm helio}$ (km s^{-1})	$V_{\rm err}$ (km s^{-1})	*SNR*	*hght*	$V_{\rm helio}$ (km s^{-1})	$V_{\rm err}$ (km s^{-1})	Flag
165	271722	295.6271	-15.1013	5.63	...	...	4	0.37	-71	43	7	0.35	128	66	...
166	301701	295.4275	-15.2504	7.68	...	...	...	...	...	...	4	0.24	-67	77	...
167	277183	295.6402	-15.1297	5.65	M	dM	10	0.25	66	100	...	...	...	...	M
169	287590	295.4488	-15.1787	7.24	...	...	3	0.28	-156	42	6	0.49	-9	59	...
171	276077	295.4292	-15.1240	7.19	...	...	5	0.31	-63	36	8	0.29	15	62	...
172	289833	295.4060	-15.1896	7.60	M	dK	10	0.43	-17	71	15	0.73	-61	39	...
173	286135	295.4173	-15.1719	7.45	M	dM	7	0.33	-80	52	10	0.35	-49	60	M
174	245610	295.9698	-14.9751	2.63	M	C	3	0.33	-87	54	4	0.72	-53	28	C
176	248935	295.5452	-14.9900	5.91	...	...	2	0.24	-135	100	...	...	...	...	...
178	246831	295.6393	-14.9802	5.14	M	dK:	5	0.48	55	37	9	0.53	-9	52	...
180	267519	295.5965	-15.0808	5.78	...	...	2	0.30	162	69	...	...	...	...	...
181	254251	295.4047	-15.0152	7.09	M	dK	12	0.55	7	38	19	0.69	-2	46	...
183	222762	295.5945	-14.8825	5.33	M	dM	...	...	...	...	9	0.29	105	59	M
184	223794	295.5475	-14.8869	5.72	M	dM	10	0.31	-24	79	12	0.35	9	51	M
185	215764	295.5244	-14.8552	5.88	M	dMe:	5	0.31	-39	81	8	0.30	-40	54	M
186	223551	295.6212	-14.8859	5.11	M	dK	5	0.30	102	100	9	0.45	-52	56	...
187	202875	296.0932	-14.8081	1.16	...	...	4	0.40	-21	47	8	0.61	-36	37	...
188	239242	295.5597	-14.9496	5.71	...	...	...	...	...	...	6	0.39	-75	42	...
189	234263	295.5405	-14.9339	5.84	M	dM:	6	0.39	-24	32	12	0.37	-85	31	M
190	220386	295.5359	-14.8731	5.80	M	dK	7	0.38	-190	49	9	0.54	-110	43	...
191	183391	296.0880	-14.7402	1.31	C*	C	6	0.41	-34	41	5	0.52	-43	48	C
193	193714	296.1129	-14.7762	1.02	C*	C	7	0.42	-130	59	9	0.72	-41	26	C
194	184165	295.6097	-14.7429	5.18	M	dM:	5	0.41	-22	53	7	0.44	24	81	M
195	208174	295.5125	-14.8268	5.96	M	dMe	5	0.44	113	76	9	0.55	5	70	M
198	178893	296.1107	-14.7258	1.20	C*	C	6	0.55	-40	49	6	0.69	-42	24	C
199	185402	295.5161	-14.7470	5.95	M	dMe	16	0.49	58	47	20	0.66	-2	49	M
201	197170	296.1522	-14.7884	0.68	M	Ce	7	0.72	-85	20	6	0.73	-59	22	C
202	201578	295.5278	-14.8036	5.83	M	dMe:	9	0.45	-2	54	15	0.47	-43	34	M
203	216118	296.0726	-14.8565	1.41	...	...	5	0.46	-85	29	6	0.47	-108	41	...

Continued on next page

Appendix B (cont.): Objects meeting the criteria ($hght \geqslant 0.2$, -200 km s$^{-1} \leqslant V_{\rm helio} \leqslant +200$ km s^{-1}).

[1]	[2]	[3]	[4]	[5]	[6]	[7]	[8]	[9]	[10]	[11]	[12]	[13]	[14]	[15]	[16]
							30 August 2011				31 August 2011				
#Fibre	ID	RA (°)	Dec (°)	distance (kpc)	phot. class.	spec. class.	*SNR*	*hght*	$V_{\rm helio}$ (km s^{-1})	$V_{\rm err}$ (km s^{-1})	*SNR*	*hght*	$V_{\rm helio}$ (km s^{-1})	$V_{\rm err}$ (km s^{-1})	Flag
204	209652	296.0846	-14.8323	1.26	C*	C:	...	...	...	...	6	0.44	-126	48	C
205	201803	295.6219	-14.8043	5.06	M	dM:	4	0.46	-122	50	5	0.30	-122	53	M
206	188974	296.1316	-14.7593	0.92	M	Ce	7	0.48	-42	33	8	0.66	-105	19	C
207	201131	296.1601	-14.8021	0.61	M	C	8	0.64	-130	25	9	0.72	-114	28	C
208	191195	296.1062	-14.7672	1.09	M	C	5	0.46	-85	27	6	0.44	-141	45	C
209	200928	295.5591	-14.8014	5.58	M	dMe:	6	0.32	-45	69	9	0.52	-18	42	M
210	201043	296.0731	-14.8017	1.33	M	C	4	0.38	-102	44	5	0.58	-77	21	C
211	205865	296.1912	-14.8187	0.38	C*	Ce	8	0.55	-40	41	12	0.80	-64	23	C
213	143954	295.4092	-14.5679	7.11	M	dM	3	0.34	-89	39	5	0.36	-37	50	M
214	212970	296.0661	-14.8446	1.43	M*	C	5	0.30	-87	88	7	0.31	-89	56	C
216	217770	296.0040	-14.8628	1.97	...	...	4	0.26	-90	44	4	0.46	-94	38	...
218	135229	295.5748	-14.5261	5.94	...	...	...	...	...	...	2	0.21	66	65	...
219	203778	296.0307	-14.8112	1.68	...	...	4	0.29	-101	94	3	0.48	-64	53	...
220	207096	296.1620	-14.8231	0.62	M	C	5	0.61	-21	25	5	0.40	-42	60	C
221	170279	295.9695	-14.6944	2.37	M	C	4	0.66	-43	24	7	0.76	-65	18	C
222	147856	295.5879	-14.5868	5.65	...	...	4	0.31	-54	66	4	0.45	-45	60	...
223	235703	296.0176	-14.9387	2.13	...	...	2	0.46	-26	61	4	0.44	-58	58	...
225	166319	296.1062	-14.6769	1.50	...	...	3	0.36	-101	31	5	0.46	-71	49	...
226	170004	296.1106	-14.6932	1.37	Unid*	C	5	0.34	10	77	3	0.41	-75	39	C
228	212351	296.1680	-14.8422	0.64	M	C	5	0.53	-84	42	6	0.69	-52	18	C
229	167638	295.9689	-14.6830	2.41	M*	C	6	0.50	-54	34	7	0.83	-88	16	C
230	174226	296.0757	-14.7119	1.51	M	C	2	0.43	-27	63	3	0.44	-21	33	C
232	100740	295.4153	-14.3432	7.82	...	...	3	0.20	-122	173	5	0.27	93	86	...
233	179746	296.2203	-14.7284	0.64	...	...	6	0.45	-99	31	6	0.54	-96	32	...
235	173378	296.0991	-14.7082	1.37	C*	C	5	0.46	-132	28	4	0.55	-106	40	C
236	92831	295.5579	-14.3032	7.03	...	...	...	...	...	...	8	0.22	-180	54	...
237	88989	295.4625	-14.2837	7.77	M	dM	6	0.22	-55	80	10	0.42	-143	56	M
238	186430	296.2347	-14.7504	0.44	M	Unid	13	0.46	-83	59	9	0.56	-74	31	...
242	78560	295.5253	-14.2302	7.63	M	dK	7	0.33	-15	76	13	0.55	-46	51	...

Continued on next page

Appendix B (cont.): Objects meeting the criteria ($hght \geqslant 0.2$, -200 km s$^{-1} \leqslant V_{\rm helio} \leqslant +200$ km s^{-1}).

[1]	[2]	[3]	[4]	[5]	[6]	[7]	[8]	[9]	[10]	[11]	[12]	[13]	[14]	[15]	[16]
							30 August 2011				31 August 2011				
#Fibre	ID	RA (°)	Dec (°)	distance (kpc)	phot. class.	spec. class.	*SNR*	*hght*	$V_{\rm helio}$ (km s^{-1})	$V_{\rm err}$ (km s^{-1})	*SNR*	*hght*	$V_{\rm helio}$ (km s^{-1})	$V_{\rm err}$ (km s^{-1})	Flag
244	67411	295.5797	-14.1739	7.62	...	...	2	0.26	185	88	...	...	...	...	...
245	86214	295.5885	-14.2705	7.01	M	dM	10	0.38	29	49	...	...	...	...	M
246	191318	296.2345	-14.7677	0.29	C*	C	14	0.68	-76	21	10	0.79	-84	21	C
252	195133	296.2290	-14.7813	0.18	C*	Ce:	12	0.53	-63	42	10	0.60	-69	27	C
254	64581	295.6043	-14.1601	7.57	M	dM:	5	0.56	-41	31	9	0.55	-42	42	M
255	93873	295.8687	-14.3087	5.19	...	...	2	0.28	-52	67	3	0.25	-23	51	...
256	50172	295.6167	-14.0903	7.94	...	...	...	...	...	...	2	0.35	14	64	...
257	184858	296.1712	-14.7452	0.70	M	C	5	0.40	-38	49	7	0.60	-33	28	C
258	173834	296.2229	-14.7102	0.79	...	...	6	0.44	-32	50	7	0.69	-83	23	...
259	49090	295.7356	-14.0852	7.39	...	...	...	...	...	...	6	0.36	-137	119	...
260	195884	296.2137	-14.7839	0.22	M	C	9	0.62	-18	24	11	0.73	-57	21	C
261	83041	295.9087	-14.2535	5.40	...	...	4	0.38	-80	65	4	0.39	-141	59	...
262	165760	296.2045	-14.6743	1.12	M	C	6	0.44	40	37	6	0.49	-42	51	C
263	107892	295.8087	-14.3808	5.03	M	dK	5	0.38	-62	82	10	0.33	-82	88	...
266	200300	296.1843	-14.7992	0.41	M	Ce:	8	0.44	-44	50	8	0.53	-33	27	C
267	158986	296.1904	-14.6417	1.41	M	C	5	0.61	-61	36	5	0.50	-65	45	C
268	157078	296.1170	-14.6327	1.74	M	C:	6	0.66	-120	36	8	0.80	-88	22	C
269	200182	296.1704	-14.7988	0.52	C*	Ce	7	0.69	-37	27	9	0.67	-33	37	C
271	42925	295.8407	-14.0569	7.15	...	...	3	0.37	-89	67	7	0.30	-153	75	...
273	172060	296.1964	-14.7023	0.90	C*	dK	4	0.36	162	98	6	0.23	-38	96	...
274	168826	296.1793	-14.6880	1.07	M	C	5	0.67	-42	34	9	0.69	-37	29	C
277	76159	295.9555	-14.2182	5.50	...	...	...	...	...	...	8	0.26	-120	69	...
279	181364	296.1274	-14.7337	1.05	...	...	9	0.69	-54	26	9	0.64	-71	28	...
281	30076	295.9677	-13.9884	7.30	...	...	4	0.33	82	56	7	0.49	-23	34	...
282	22972	295.9881	-13.9511	7.55	...	...	4	0.42	50	36	6	0.49	76	35	...
283	194386	296.1861	-14.7787	0.44	...	...	10	0.76	-52	21	10	0.86	-59	15	...
284	173114	296.3308	-14.7071	1.14	M*	dM:	19	0.82	-63	22	...	...	...	...	...
285	78272	296.0687	-14.2288	5.09	M	dM:	...	...	...	...	7	0.48	23	47	M
286	27278	296.0793	-13.9738	7.19	M	dM:	...	...	...	...	9	0.39	44	89	M

Continued on next page

Appendix B (cont.): Objects meeting the criteria ($hght \geqslant 0.2$, -200 km s$^{-1} \leqslant V_{\rm helio} \leqslant +200$ km s^{-1}).

[1]	[2]	[3]	[4]	[5]	[6]	[7]	[8]	[9]	[10]	[11]	[12]	[13]	[14]	[15]	[16]
							30 August 2011				31 August 2011				
#Fibre	ID	RA (°)	Dec (°)	distance (kpc)	phot. class.	spec. class.	*SNR*	*hght*	$V_{\rm helio}$ (km s^{-1})	$V_{\rm err}$ (km s^{-1})	*SNR*	*hght*	$V_{\rm helio}$ (km s^{-1})	$V_{\rm err}$ (km s^{-1})	Flag
287	179183	295.9771	-14.7267	2.21	C*	C	...	...	...	...	4	0.44	-53	32	C
289	64658	296.1430	-14.1604	5.53	...	...	4	0.42	1	47	5	0.42	46	60	...
290	192177	296.3332	-14.7707	0.87	M	C	4	0.43	-61	56	5	0.59	-51	20	C
291	74535	296.2869	-14.2100	5.08	...	...	3	0.26	-85	46	6	0.27	-62	47	...
292	169202	296.2486	-14.6898	0.96	M	C	5	0.57	-56	46	7	0.66	-54	15	C
293	159727	296.2520	-14.6456	1.34	...	...	3	0.50	-15	28	5	0.47	-57	33	...
294	17384	296.2199	-13.9232	7.51	...	...	...	...	...	...	5	0.38	-5	42	...
295	165127	296.2339	-14.6713	1.12	M	C	6	0.76	-52	19	8	0.68	-59	20	C
296	171315	296.4032	-14.6991	1.66	...	...	5	0.50	-33	37	5	0.69	-66	14	...
297	21034	296.2502	-13.9411	7.36	M	dK	4	0.45	70	43	7	0.65	-104	36	...
298	194777	296.2784	-14.7801	0.42	C*	Ce:	9	0.61	-72	37	9	0.72	-29	23	C
301	164620	296.2195	-14.6690	1.14	...	...	4	0.62	-101	29	6	0.63	-114	32	...
302	182253	296.3110	-14.7364	0.85	...	...	5	0.58	-69	38	5	0.62	-33	25	...
304	62395	296.3653	-14.1494	5.68	M	dM	6	0.46	-59	52	...	...	...	...	M
305	167938	296.2598	-14.6842	1.03	M*	C	5	0.55	-67	41	7	0.82	-76	18	C
306	12243	296.3583	-13.8970	7.81	M	dM:	6	0.40	21	39	8	0.37	10	46	M
307	20479	296.3300	-13.9385	7.43	M	dK	8	0.40	-65	53	9	0.61	-26	43	...
308	71601	296.3390	-14.1952	5.26	...	...	2	0.22	-35	84	4	0.33	-136	57	...
309	72678	296.3685	-14.2006	5.26	...	...	4	0.27	-128	87	...	...	...	...	...
311	61106	296.3327	-14.1429	5.69	...	...	...	...	...	...	5	0.38	81	77	...
313	193220	296.2904	-14.7745	0.53	M	Ce:	7	0.36	-86	87	5	0.46	10	32	C
314	198595	296.2580	-14.7932	0.22	M	Ce:	15	0.70	-51	28	12	0.79	-46	24	C
316	162531	296.2790	-14.6591	1.28	...	...	3	0.35	-7	32	4	0.44	-26	38	...
317	29959	296.3970	-13.9879	7.09	M	dM:	6	0.48	-11	35	9	0.51	-53	43	M
318	61790	296.4553	-14.1463	5.90	...	...	5	0.29	-66	53	6	0.51	-48	32	...
319	32087	296.5526	-13.9992	7.36	M	dK	5	0.29	17	76	10	0.50	88	53	...
320	183545	296.2857	-14.7407	0.68	...	...	9	0.58	-27	34	7	0.69	-43	28	...
321	196632	296.2456	-14.7865	0.16	...	...	17	0.64	-56	46	14	0.72	-117	28	...
322	188333	296.3510	-14.7571	1.05	M*	C:	27	0.74	-17	39	12	0.84	-51	19	C

Continued on next page

Appendix B (cont.): Objects meeting the criteria ($hght \geqslant 0.2$, -200 km s$^{-1} \leqslant V_{\rm helio} \leqslant +200$ km s^{-1}).

[1]	[2]	[3]	[4]	[5]	[6]	[7]	[8]	[9]	[10]	[11]	[12]	[13]	[14]	[15]	[16]
							30 August 2011				31 August 2011				
#Fibre	ID	RA (°)	Dec (°)	distance (kpc)	phot. class.	spec. class.	*SNR*	*hght*	$V_{\rm helio}$ (km s^{-1})	$V_{\rm err}$ (km s^{-1})	*SNR*	*hght*	$V_{\rm helio}$ (km s^{-1})	$V_{\rm err}$ (km s^{-1})	Flag
323	174472	296.3415	-14.7129	1.17	C*	C	5	0.51	-57	34	7	0.57	-72	29	C
324	67487	296.4927	-14.1743	5.78	M	dM:	6	0.31	30	71	8	0.42	63	54	M
325	170941	296.2867	-14.6973	1.00	M*	dK	14	0.64	-20	42	16	0.66	-47	32	...
326	176863	296.3510	-14.7207	1.19	C*	C	7	0.53	-37	27	6	0.51	-62	23	C
327	83584	296.4613	-14.2566	5.03	M	dM:	9	0.34	-18	83	15	0.59	37	34	M
328	187649	296.2445	-14.7547	0.41	M	C:	9	0.66	-75	25	11	0.72	-46	18	C
330	167230	296.3354	-14.6811	1.33	C*	C	4	0.49	-31	46	7	0.51	-123	41	C
332	35137	296.6521	-14.0153	7.57	M	dK:	5	0.29	-27	116	8	0.27	-76	105	...
334	177839	296.2471	-14.7230	0.68	M	C	8	0.63	0	27	9	0.65	-32	28	C
336	38421	296.7117	-14.0327	7.68	M	dK:	...	...	...	...	6	0.28	-23	34	...
337	45220	296.7658	-14.0663	7.68	...	...	...	...	...	...	8	0.30	48	77	...
338	164010	296.3261	-14.6662	1.39	M	C	4	0.34	-100	66	7	0.60	-53	20	C
345	117821	296.7135	-14.4348	5.06	...	...	7	0.34	-40	72	...	...	...	...	...
348	80533	296.8526	-14.2400	7.03	...	...	4	0.37	-26	67	...	...	...	...	...
349	176619	296.2290	-14.7201	0.70	...	...	6	0.54	-62	34	9	0.65	-28	25	...
351	98241	296.6535	-14.3304	5.32	M	dM	5	0.52	-138	30	10	0.41	-42	95	M
352	91537	296.6148	-14.2963	5.35	...	...	3	0.44	-107	46	...	...	...	...	...
354	165802	296.4082	-14.6744	1.81	...	...	3	0.26	-12	82	6	0.53	-37	40	...
355	82795	296.9455	-14.2523	7.54	...	...	...	...	...	...	7	0.28	-141	111	...
357	84888	296.9962	-14.2637	7.81	...	...	3	0.31	-194	34	...	...	...	...	...
358	123455	296.8291	-14.4649	5.71	...	...	...	...	...	...	5	0.42	-48	71	...
359	127636	296.7871	-14.4884	5.31	M	dK:	4	0.29	-14	96	9	0.56	-15	53	...
360	104563	296.9575	-14.3638	7.07	...	...	3	0.43	-197	49	...	...	...	...	...
361	112177	296.8211	-14.4041	5.94	M	dM:	5	0.24	33	66	11	0.50	-4	75	M
362	81011	296.9797	-14.2425	7.81	M	dM	...	...	...	...	8	0.33	74	94	M
364	110475	297.0062	-14.3949	7.28	...	...	3	0.35	-5	90	5	0.40	9	64	...
366	152918	296.8130	-14.6119	5.06	M	C:	4	0.24	82	99	9	0.58	14	26	...
368	119903	296.7926	-14.4460	5.54	...	...	...	...	...	...	7	0.43	-33	85	...
369	167631	296.5085	-14.6829	2.49	...	...	3	0.36	-12	22	...	...	...	...	...

Continued on next page

Appendix B (cont.): Objects meeting the criteria ($hght \geqslant 0.2$, -200 km s$^{-1} \leqslant V_{\rm helio} \leqslant +200$ km s^{-1}).

[1]	[2]	[3]	[4]	[5]	[6]	[7]	[8]	[9]	[10]	[11]	[12]	[13]	[14]	[15]	[16]
							30 August 2011				31 August 2011				
#Fibre	ID	RA (°)	Dec (°)	distance (kpc)	phot. class.	spec. class.	*SNR*	*hght*	$V_{\rm helio}$ (km s^{-1})	$V_{\rm err}$ (km s^{-1})	*SNR*	*hght*	$V_{\rm helio}$ (km s^{-1})	$V_{\rm err}$ (km s^{-1})	Flag
370	140011	296.8003	-14.5496	5.16	M	dM:	6	0.43	28	32	12	0.49	-9	41	M
371	117981	297.0500	-14.4357	7.45	...	...	...	...	...	...	8	0.40	-7	46	...
372	117401	297.1003	-14.4324	7.84	M	dK:	...	...	...	...	6	0.30	57	57	...
373	158905	296.8255	-14.6414	5.09	...	...	3	0.27	150	64	7	0.59	-22	28	...
374	141439	296.8344	-14.5561	5.40	...	...	2	0.49	17	40	5	0.33	18	43	...
375	130447	297.1311	-14.5022	7.86	...	...	2	0.27	163	55	5	0.34	11	40	...
376	148616	296.8530	-14.5907	5.43	M	dK:	...	...	...	...	8	0.28	5	44	...
377	152475	296.8548	-14.6095	5.40	...	...	...	...	...	...	10	0.26	-150	45	...
378	124695	297.0647	-14.4717	7.44	...	...	5	0.24	110	93	9	0.43	75	45	...
379	128222	297.0240	-14.4918	7.06	M	dM:	5	0.35	-40	36	9	0.25	-149	72	M
380	141960	297.0478	-14.5586	7.05	...	...	3	0.34	-178	53	...	...	...	...	...
381	136987	297.0594	-14.5348	7.21	...	...	6	0.30	-11	59	7	0.23	22	47	...
382	168122	296.8688	-14.6850	5.35	...	...	...	...	...	...	8	0.21	18	116	...
383	146932	297.0727	-14.5825	7.19	M	dM:	...	...	...	...	8	0.40	39	43	M
384	165837	296.9215	-14.6746	5.79	...	...	3	0.27	-96	94	...	...	...	...	...
388	157802	296.9112	-14.6362	5.78	M	dK:	11	0.34	7	51	...	...	...	...	...
389	165036	297.1028	-14.6708	7.28	...	...	...	...	...	...	7	0.25	77	136	...
390	155389	297.1115	-14.6241	7.42	M	dM:	...	...	...	...	14	0.27	-108	81	M
393	159040	297.1004	-14.6420	7.30	...	...	...	...	...	...	6	0.25	78	47	...
394	165107	297.1484	-14.6712	7.65	M	dM:	4	0.29	-139	53	9	0.53	12	28	M
395	170606	296.8965	-14.6958	5.56	...	...	...	...	...	...	5	0.33	21	58	...
398	204144	296.4050	-14.8125	1.42	Unid*	C	11	0.73	-43	25	11	0.63	-50	32	C
399	174894	296.8487	-14.7146	5.14	...	...	...	...	...	...	10	0.64	4	43	...

The following table explains the content of each column in the Appendix B

Column	Description
1 & 2	Fibre number and the target identifier respectively as defined by Sibbons et al. [2015].
3 & 4	Right ascension (RA) and declination (Dec) of each object (J2000) according to Sibbons et al. [2015].
5	Distance of the object from the galactic centre ($\alpha = 19^h : 44^m : 56^s$ (296.2333°), J2000 and $\delta = -14° : 48' : 06''$ (−14.8017°), J2000) centred on the optical co-ordinates of NGC 6822[1] adopted by Sibbons et al. [2012, 2015] and a galactic distance of 490 kpc [Mateo, 1998].
6 & 7	Photometric classification of each object from Sibbons et al. [2012], and its corresponding spectroscopic classification from Sibbons et al. [2015]. See Sibbons et al. [2015] for J, H, K magnitudes
8 & 12	*SNR* of each object calculated in the band 8560 Å to 8650 Å for the nights of 30 August 2011 and 31 August 2011 respectively.
9, 10 & 11	*hght*, the heliocentric radial velocity (V_{helio}) and the velocity error (V_{err}) returned from *fxcor* for the night of 30 August 2011.
13, 14 & 15	*hght*, the heliocentric radial velocity (V_{helio}) and the velocity error (V_{err}) returned from *fxcor* for the night of 31 August 2011.
16	Flag showing which objects were used in the composite templates: "C" for the C-type composite and "M" for the M-type composite.

C. IRAF modules used in the study

The following IRAF applications were used in this study :

- *splot* is a spectrum plotting package which enables each spectrum to be individually examined. The package can be used to find the S/N ratio over various bands and the signal level measured pixel by pixel. *splot* lies in the **onedspec** folder in the **noao** package within IRAF.

- *rvidlines* is a single spectrum plot which enables the user to identify and select one or more spectral lines and input their rest values. The module then computes the V_r and an error value for the lines. This package can be used to establish the motion of the template with respect to the observer.

- *rvcorrect* is a module which enables the heliocentric correction to be found given the epoch of the observation, the locations of the observatory and object.

- *scopy* is a routine in *onedspec* in IRAF, which is used to copy .fits files into .fits or .txt files and can be used to place limitations on selected parameters, such as the wave band of interest.

- *dopcor* is a routine also in *onedspec*, in which a spectrum can be Doppler corrected by a shift which can be individually assigned. If the amount of shift required is determined by *fxcor* from a reference spectrum in a 'rest frame', the object spectrum can be shifted to the 'rest frame'. In general for multiple spectra. the amount of Doppler shift will differ from object to object. For a group of ~ 100 objects, this process was automated in *Python*.

- *scombine* is another routine in *onedspec*, which enables two or more spectra to be combined into a single spectra.

Many of the routines were automated in *Python* using *Pyraf*. Scripts have been written to:

- Measure the SNR of all objects in the range 8560 Å to 8650 Å.
- Generate the composite template and measure its SNR.
- Select acceptable results meeting the selection criteria, plot radial velocities, histograms and plots of errors with respect to the SNR and *hght*.
- Compute and plot the rotation of the AGB stellar content.

Bibliography

B. P. Abbott, R. Abbott, T. D. Abbott, M. R. Abernathy, F. Acernese, K. Ackley, C. Adams, T. Adams, P. Addesso, R. X. Adhikari, and et al. Observation of Gravitational Waves from a Binary Black Hole Merger. *Physical Review Letters*, 116(6):061102, Feb. 2016. doi: 10.1103/PhysRevLett.116.061102.

B. P. e. Abbott. Astrophysical implications of the binary black hole merger gw150914. *The Astrophysical Journal Letters*, 818(2):L22, 2016. URL `http://stacks.iop.org/2041-8205/818/i=2/a=L22`.

S. Alam, F. D. Albareti, C. Allende Prieto, F. Anders, S. F. Anderson, T. Anderton, B. H. Andrews, E. Armengaud, É. Aubourg, S. Bailey, and et al. The Eleventh and Twelfth Data Releases of the Sloan Digital Sky Survey: Final Data from SDSS-III. *ApJS*, 219:12, July 2015. doi: 10.1088/0067-0049/219/1/12.

G. Bagheri, M.-R. L. Cioni, and R. Napiwotzki. The detection of an older population in the Magellanic Bridge. *A&A*, 551:A78, Mar. 2013. doi: 10.1051/0004-6361/201118236.

P. Battinelli, S. Demers, and W. E. Kunkel. Photometric survey of the polar ring galaxy NGC 6822. *A&A*, 451:99–108, May 2006. doi: 10.1051/0004-6361:20054718.

K. Bechtol, A. Drlica-Wagner, E. Balbinot, A. Pieres, J. D. Simon, B. Yanny, B. Santiago, R. H. Wechsler, J. Frieman, A. R. Walker, P. Williams, E. Rozo, E. S. Rykoff, A. Queiroz, E. Luque, A. Benoit-Lévy, D. Tucker, I. Sevilla, R. A. Gruendl, L. N. da Costa, A. Fausti Neto, M. A. G. Maia, T. Abbott, S. Allam, R. Armstrong, A. H. Bauer, G. M. Bernstein, R. A. Bernstein, E. Bertin, D. Brooks, E. Buckley-Geer, D. L. Burke, A. Carnero Rosell, F. J. Castander, R. Covarrubias, C. B. D'Andrea, D. L. DePoy, S. Desai, H. T. Diehl, T. F. Eifler, J. Estrada, A. E. Evrard, E. Fernandez, D. A. Finley, B. Flaugher, E. Gaztanaga, D. Gerdes, L. Girardi, M. Gladders, D. Gruen, G. Gutierrez, J. Hao, K. Honscheid, B. Jain, D. James, S. Kent, R. Kron, K. Kuehn, N. Kuropatkin, O. Lahav, T. S. Li, H. Lin, M. Makler, M. March, J. Marshall, P. Martini, K. W. Merritt, C. Miller, R. Miquel, J. Mohr, E. Neilsen, R. Nichol, B. Nord, R. Ogando, J. Peoples, D. Petravick, A. A. Plazas, A. K. Romer, A. Roodman, M. Sako, E. Sanchez, V. Scarpine, M. Schubnell, R. C. Smith, M. Soares-Santos, F. Sobreira, E. Suchyta, M. E. C. Swanson, G. Tarle, J. Thaler, D. Thomas, W. Wester, J. Zuntz, and DES Collaboration. Eight New Milky Way Companions Discovered in First-year Dark Energy Survey Data. *ApJ*, 807:50, July 2015. doi: 10.1088/0004-637X/807/1/50.

V. Belokurov, D. B. Zucker, N. W. Evans, G. Gilmore, S. Vidrih, D. M. Bramich, H. J. Newberg, R. F. G. Wyse, M. J. Irwin, M. Fellhauer, P. C. Hewett, N. A. Walton, M. I. Wilkinson, N. Cole, B. Yanny, C. M. Rockosi, T. C. Beers, E. F. Bell, J. Brinkmann, Ž. Ivezić, and R. Lupton. The Field of Streams: Sagittarius and Its Siblings. *ApJ*, 642:L137–L140, May 2006. doi: 10.1086/504797.

V. Belokurov, N. W. Evans, M. J. Irwin, D. Lynden-Bell, B. Yanny, S. Vidrih, G. Gilmore, G. Seabroke, D. B. Zucker, M. I. Wilkinson, P. C. Hewett, D. M. Bramich, M. Fellhauer, H. J. Newberg, R. F. G. Wyse, T. C. Beers, E. F. Bell, J. C. Barentine, J. Brinkmann, N. Cole, K. Pan, and D. G. York. An orphan in the "field of streams". *The Astrophysical Journal*, 658 (1):337, 2007. URL `http://stacks.iop.org/0004-637X/658/i=1/a=337`.

J. Binney and M. Merrifield. *Galactic Astronomy*. 1998.

J. Binney and S. Tremaine. *Galactic Dynamics: Second Edition*. Princeton University Press, 2008.

M. R. Blanton, D. W. Hogg, N. A. Bahcall, J. Brinkmann, M. Britton, A. J. Connolly, I. Csabai, M. Fukugita, J. Loveday, A. Meiksin, J. A. Munn, R. C. Nichol, S. Okamura, T. Quinn, D. P. Schneider, K. Shimasaku, M. A. Strauss, M. Tegmark, M. S. Vogeley, and D. H. Weinberg. The Galaxy Luminosity Function and Luminosity Density at Redshift z = 0.1. *ApJ*, 592:819–838, Aug. 2003. doi: 10.1086/375776.

M. Boylan-Kolchin, J. S. Bullock, and M. Kaplinghat. Too big to fail? The puzzling darkness of massive Milky Way subhaloes. *MNRAS*, 415:L40–L44, July 2011. doi: 10.1111/j.1745-3933.2011.01074.x.

T. K. Chan, D. Kereš, J. Oñorbe, P. F. Hopkins, A. L. Muratov, C.-A. Faucher-Giguère, and E. Quataert. The impact of baryonic physics on the structure of dark matter haloes: the view from the FIRE cosmological simulations. *MNRAS*, 454:2981–3001, Dec. 2015. doi: 10.1093/mnras/stv2165.

A. D. Chernin, I. D. Karachentsev, M. J. Valtonen, V. P. Dolgachev, L. M. Domozhilova, and D. I. Makarov. The very local Hubble flow: Computer simulations of dynamical history. *A&A*, 415:19–25, Feb. 2004. doi: 10.1051/0004-6361:20034170.

A. D. Chernin, I. D. Karachentsev, O. G. Nasonova, P. Teerikorpi, M. J. Valtonen, V. P. Dolgachev, L. M. Domozhilova, and G. G. Byrd. Dark energy domination in the Virgocentric flow. *A&A*, 520:A104, Sept. 2010. doi: 10.1051/0004-6361/201014912.

P. Coles and F. Lucchin. *Cosmology: The Origin and Evolution of Cosmic Structure, Second Edition*. July 2002.

M. Colless, G. Dalton, S. Maddox, W. Sutherland, P. Norberg, S. Cole, J. Bland-Hawthorn, T. Bridges, R. Cannon, C. Collins, W. Couch, N. Cross, K. Deeley, R. De Propris, S. P. Driver, G. Efstathiou, R. S. Ellis, C. S. Frenk, K. Glazebrook, C. Jackson, O. Lahav, I. Lewis, S. Lumsden, D. Madgwick, J. A. Peacock, B. A. Peterson, I. Price, M. Seaborne, and K. Taylor. The 2dF Galaxy Redshift Survey: spectra and redshifts. *MNRAS*, 328:1039–1063, Dec. 2001. doi: 10.1046/j.1365-8711.2001.04902.x.

W. J. G. de Blok and F. Walter. Evidence for Tidal Interaction and a Supergiant H I Shell in the Local Group Dwarf Galaxy NGC 6822. *ApJ*, 537:L95–L98, July 2000. doi: 10.1086/312777.

G. de Vaucouleurs. Classification and Morphology of External Galaxies. *Handbuch der Physik*, 53:275, 1959.

G. de Vaucouleurs, A. de Vaucouleurs, H. G. Corwin, Jr., R. J. Buta, G. Paturel, and P. Fouqué. *Third Reference Catalogue of Bright Galaxies. Volume I: Explanations and references. Volume II: Data for galaxies between 0^h and 12^h. Volume III: Data for galaxies between 12^h and 24^h.* 1991.

H. J. de Vega and N. G. Sanchez. Model-independent analysis of dark matter points to a particle mass at the keV scale. *MNRAS*, 404:885–894, May 2010. doi: 10.1111/j.1365-2966.2010.16319.x. URL `http://adsabs.harvard.edu/abs/2010MNRAS.404..885D`.

S. Demers and P. Battinelli. The Singular Contribution of AGB Stars to our Understanding of Galactic Dynamics. In F. Kerschbaum, C. Charbonnel, and R. F. Wing, editors, *Why Galaxies Care About AGB Stars: Their Importance as Actors and Probes*, volume 378 of *Astronomical Society of the Pacific Conference Series*, page 469, Nov. 2007.

S. Demers, P. Battinelli, and W. E. Kunkel. A Local Group Polar Ring Galaxy: NGC 6822. *ApJ*, 636:L85–L88, Jan. 2006. doi: 10.1086/500207.

C. Destri, H. J. de Vega, and N. G. Sanchez. Fermionic warm dark matter produces galaxy cores in the observed scales. *ArXiv e-prints*, Apr. 2012. URL `http://adsabs.harvard.edu/abs/2012arXiv1204.3090D`.

A. Di Cintio, C. B. Brook, A. A. Dutton, A. V. Macciò, G. S. Stinson, and A. Knebe. A mass-dependent density profile for dark matter haloes including the influence of galaxy formation. *MNRAS*, 441:2986–2995, July 2014. doi: 10.1093/mnras/stu729.

A. Drlica-Wagner, K. Bechtol, E. S. Rykoff, E. Luque, A. Queiroz, Y.-Y. Mao, R. H. Wechsler, J. D. Simon, B. Santiago, B. Yanny, E. Balbinot, S. Dodelson, A. Fausti Neto, D. J. James, T. S. Li, M. A. G. Maia, J. L. Marshall, A. Pieres, K. Stringer, A. R. Walker, T. M. C. Abbott, F. B. Abdalla, S. Allam, A. Benoit-Lévy, G. M. Bernstein, E. Bertin, D. Brooks, E. Buckley-Geer, D. L. Burke, A. Carnero Rosell, M. Carrasco Kind, J. Carretero, M. Crocce, L. N. da Costa, S. Desai, H. T. Diehl, J. P. Dietrich, P. Doel, T. F. Eifler, A. E. Evrard, D. A. Finley, B. Flaugher, P. Fosalba, J. Frieman, E. Gaztanaga, D. W. Gerdes, D. Gruen, R. A. Gruendl, G. Gutierrez, K. Honscheid, K. Kuehn, N. Kuropatkin, O. Lahav, P. Martini, R. Miquel, B. Nord, R. Ogando, A. A. Plazas, K. Reil, A. Roodman, M. Sako, E. Sanchez, V. Scarpine, M. Schubnell, I. Sevilla-Noarbe, R. C. Smith, M. Soares-Santos, F. Sobreira, E. Suchyta, M. E. C. Swanson, G. Tarle, D. Tucker, V. Vikram, W. Wester, Y. Zhang, J. Zuntz, and The DES Collaboration. Eight Ultra-faint Galaxy Candidates Discovered in Year Two of the Dark Energy Survey. *ApJ*, 813: 109, Nov. 2015. doi: 10.1088/0004-637X/813/2/109.

N. W. Evans and M. I. Wilkinson. The mass of the Andromeda galaxy. *MNRAS*, 316:929–942, Aug. 2000. doi: 10.1046/j.1365-8711.2000.03645.x.

B. Famaey and S. McGaugh. Modified Newtonian Dynamics (MOND): Observational Phenomenology and Relativistic Extensions. *ArXiv e-prints*, Dec. 2011. URL `http://adsabs.harvard.edu/abs/2011arXiv1112.3960F`.

M. W. Feast, P. A. Whitelock, J. W. Menzies, and N. Matsunaga. The Cepheid distance to the Local Group galaxy NGC 6822. *MNRAS*, 421:2998–3003, Apr. 2012. doi: 10.1111/j.1365-2966.2012.20525.x.

J. L. Feng. Dark Matter Candidates from Particle Physics and Methods of Detection. *ARA&A*, 48:495–545, Sept. 2010. doi: 10.1146/annurev-astro-082708-101659.

D. J. Fixsen. The Temperature of the Cosmic Microwave Background. *ApJ*, 707:916–920, Dec. 2009. doi: 10.1088/0004-637X/707/2/916.

S. N. Flores-Durán, M. Peña, L. Hernández-Martínez, J. García-Rojas, and M. T. Ruiz. Kinematic study of planetary nebulae in NGC 6822. *A&A*, 568:A82, Aug. 2014. doi: 10.1051/0004-6361/201322002.

A. Friedmann. Über die Krümmung des Raumes. *Zeitschrift fur Physik*, 10:377–386, 1922. doi: 10.1007/BF01332580.

M. J. Geller and J. P. Huchra. Mapping the universe. *Science*, 246:897–903, Nov. 1989. doi: 10.1126/science.246.4932.897.

W. Gieren, G. Pietrzyński, K. Nalewajko, I. Soszyński, F. Bresolin, R.-P. Kudritzki, D. Minniti, and A. Romanowsky. The Araucaria Project: An Accurate Distance to the Local Group Galaxy NGC 6822 from Near-Infrared Photometry of Cepheid Variables. *ApJ*, 647:1056–1064, Aug. 2006. doi: 10.1086/505574.

E. K. Grebel, J. S. Gallagher, III, and D. Harbeck. The Progenitors of Dwarf Spheroidal Galaxies. *AJ*, 125:1926–1939, Apr. 2003. doi: 10.1086/368363.

P. Guhathakurta, R. M. Rich, D. B. Reitzel, M. C. Cooper, K. M. Gilbert, S. R. Majewski, J. C. Ostheimer, M. C. Geha, K. V. Johnston, and R. J. Patterson. Dynamics and stellar content of the giant southern stream in m31. i. keck spectroscopy of red giant stars. *The Astronomical Journal*, 131(5):2497, 2006. URL `http://stacks.iop.org/1538-3881/131/i=5/a=2497`.

Q. Guo, S. White, M. Boylan-Kolchin, G. De Lucia, G. Kauffmann, G. Lemson, C. Li, V. Springel, and S. Weinmann. From dwarf spheroidals to cD galaxies: simulating the galaxy population in a ΛCDM cosmology. *MNRAS*, 413:101–131, May 2011. doi: 10.1111/j.1365-2966.2010.18114.x.

K. Hinkle, L. Wallace, J. Valenti, and D. Harmer. *Visible and Near Infrared Atlas of the Arcturus Spectrum 3727-9300 A*. 2000.

G. Hinshaw, D. Larson, E. Komatsu, D. N. Spergel, C. L. Bennett, J. Dunkley, M. R. Nolta, M. Halpern, R. S. Hill, N. Odegard, L. Page, K. M. Smith, J. L. Weiland, B. Gold, N. Jarosik, A. Kogut, M. Limon, S. S. Meyer, G. S. Tucker, E. Wollack, and E. L. Wright. Nine-year Wilkinson Microwave Anisotropy Probe (WMAP) Observations: Cosmological Parameter Results. *ApJS*, 208:19, Oct. 2013. doi: 10.1088/0067-0049/208/2/19.

P. Hodge, T. Smith, P. Eskridge, H. MacGillivray, and S. Beard. A COSMOS study of the structure and content of NGC 6822. *ApJ*, 379:621–630, Oct. 1991. doi: 10.1086/170534.

P. W. Hodge. *The physics and astronomy of galaxies and cosmology*. 1966.

E. Hubble. No. 304. N.G.C. 6822, a remote stellar system. *Contributions from the Mount Wilson Observatory / Carnegie Institution of Washington*, 304:1–25, 1925.

E. P. Hubble. *Realm of the Nebulae*. 1936.

N. Hwang, H. S. Park, M. G. Lee, S. Lim, P. W. Hodge, S. C. Kim, B. Miller, and D. Weisz. Spectroscopic Study of Extended Star Clusters in Dwarf Galaxy NGC 6822. *ApJ*, 783:49, Mar. 2014. doi: 10.1088/0004-637X/783/1/49.

I. D. Karachentsev and D. A. Makarov. The Galaxy Motion Relative to Nearby Galaxies and the Local Velocity Field. *AJ*, 111:794, Feb. 1996. doi: 10.1086/117825.

I. D. Karachentsev and O. G. Nasonova. The observed infall of galaxies towards the Virgo cluster. *MNRAS*, 405:1075–1083, June 2010. doi: 10.1111/j.1365-2966.2010.16501.x.

I. D. Karachentsev, V. E. Karachentseva, W. K. Huchtmeier, and D. I. Makarov. A Catalog of Neighboring Galaxies. *AJ*, 127:2031–2068, Apr. 2004. doi: 10.1086/382905.

I. D. Karachentsev, O. G. Kashibadze, D. I. Makarov, and R. B. Tully. The Hubble flow around the Local Group. *MNRAS*, 393:1265–1274, Mar. 2009. doi: 10.1111/j.1365-2966.2008.14300.x.

I. D. Karachentsev, D. I. Makarov, and E. I. Kaisina. Updated Nearby Galaxy Catalog. *AJ*, 145: 101, Apr. 2013. doi: 10.1088/0004-6256/145/4/101.

I. D. Karachentsev, L. N. Makarova, R. B. Tully, P.-F. Wu, and A. Y. Kniazev. KK258, a new transition dwarf galaxy neighbouring the Local Group. *MNRAS*, 443:1281–1290, Sept. 2014. doi: 10.1093/mnras/stu1217.

I. D. Karachentsev, A. Y. Kniazev, and M. E. Sharina. The isolated dSph galaxy KKs3 in the local Hubble flow. *Astronomische Nachrichten*, 336:707, Sept. 2015a. doi: 10.1002/asna.201512207.

I. D. Karachentsev, L. N. Makarova, D. I. Makarov, R. B. Tully, and L. Rizzi. A new isolated dSph galaxy near the Local Group. *MNRAS*, 447:L85–L89, Feb. 2015b. doi: 10.1093/mnrasl/slu181.

D. Kim and H. Jerjen. Horologium II: A Second Ultra-faint Milky Way Satellite in the Horologium Constellation. *ApJ*, 808:L39, Aug. 2015. doi: 10.1088/2041-8205/808/2/L39.

D. Kim, H. Jerjen, D. Mackey, G. S. Da Costa, and A. P. Milone. A Hero's Dark Horse: Discovery of an Ultra-faint Milky Way Satellite in Pegasus. *ApJ*, 804:L44, May 2015a. doi: 10.1088/2041-8205/804/2/L44.

D. Kim, H. Jerjen, A. P. Milone, D. Mackey, and G. S. Da Costa. Discovery of a Faint Outer Halo Milky Way Star Cluster in the Southern Sky. *ApJ*, 803:63, Apr. 2015b. doi: 10.1088/0004-637X/803/2/63.

I. King. The structure of star clusters. I. an empirical density law. *AJ*, 67:471, Oct. 1962. doi: 10.1086/108756. URL `http://adsabs.harvard.edu/abs/1962AJ.....67..471K`.

E. N. Kirby, J. S. Bullock, M. Boylan-Kolchin, M. Kaplinghat, and J. G. Cohen. The dynamics of isolated Local Group galaxies. *MNRAS*, 439:1015–1027, Mar. 2014. doi: 10.1093/mnras/stu025.

E. N. Kirby, J. G. Cohen, J. D. Simon, and P. Guhathakurta. Triangulum II: Possibly a Very Dense Ultra-Faint Dwarf Galaxy. *ArXiv e-prints*, Oct. 2015a.

E. N. Kirby, J. D. Simon, and J. G. Cohen. Spectroscopic Confirmation of the Dwarf Galaxies Hydra II and Pisces II and the Globular Cluster Laevens 1. *ApJ*, 810:56, Sept. 2015b. doi: 10.1088/0004-637X/810/1/56.

A. Klypin, A. V. Kravtsov, O. Valenzuela, and F. Prada. Where Are the Missing Galactic Satellites? *ApJ*, 522:82–92, Sept. 1999. doi: 10.1086/307643.

A. Klypin, I. Karachentsev, D. Makarov, and O. Nasonova. Abundance of field galaxies. *MNRAS*, 454:1798–1810, Dec. 2015. doi: 10.1093/mnras/stv2040.

E. Komatsu, K. M. Smith, J. Dunkley, C. L. Bennett, B. Gold, G. Hinshaw, N. Jarosik, D. Larson, M. R. Nolta, L. Page, D. N. Spergel, M. Halpern, R. S. Hill, A. Kogut, M. Limon, S. S. Meyer, N. Odegard, G. S. Tucker, J. L. Weiland, E. Wollack, and E. L. Wright. Seven-year Wilkinson Microwave Anisotropy Probe (WMAP) Observations: Cosmological Interpretation. *ApJS*, 192:18, Feb. 2011. doi: 10.1088/0067-0049/192/2/18. URL `http://adsabs.harvard.edu/abs/2011ApJS..192...18K`.

S. E. Koposov, V. Belokurov, G. Torrealba, and N. W. Evans. Beasts of the Southern Wild : Discovery of nine Ultra Faint satellites in the vicinity of the Magellanic Clouds. *ApJ*, 805:130, June 2015. doi: 10.1088/0004-637X/805/2/130.

B. S. Koribalski, L. Staveley-Smith, V. A. Kilborn, S. D. Ryder, R. C. Kraan-Korteweg, E. V. Ryan-Weber, R. D. Ekers, H. Jerjen, P. A. Henning, M. E. Putman, M. A. Zwaan, W. J. G. de Blok, M. R. Calabretta, M. J. Disney, R. F. Minchin, R. Bhathal, P. J. Boyce, M. J. Drinkwater, K. C. Freeman, B. K. Gibson, A. J. Green, R. F. Haynes, S. Juraszek, M. J. Kesteven, P. M. Knezek, S. Mader, M. Marquarding, M. Meyer, J. R. Mould, T. Oosterloo, J. O'Brien, R. M. Price, E. M. Sadler, A. Schröder, I. M. Stewart, F. Stootman, M. Waugh, B. E. Warren, R. L. Webster, and A. E. Wright. The 1000 Brightest HIPASS Galaxies: H I Properties. *AJ*, 128:16–46, July 2004. doi: 10.1086/421744.

B. P. M. Laevens, N. F. Martin, E. J. Bernard, E. F. Schlafly, B. Sesar, H.-W. Rix, E. F. Bell, A. M. N. Ferguson, C. T. Slater, W. E. Sweeney, R. F. G. Wyse, A. P. Huxor, W. S. Burgett, K. C. Chambers, P. W. Draper, K. A. Hodapp, N. Kaiser, E. A. Magnier, N. Metcalfe, J. L. Tonry, R. J. Wainscoat, and C. Waters. Sagittarius II, Draco II and Laevens 3: Three New Milky Way Satellites Discovered in the Pan-STARRS 1 3 Survey. *ApJ*, 813:44, Nov. 2015a. doi: 10.1088/0004-637X/813/1/44.

B. P. M. Laevens, N. F. Martin, R. A. Ibata, H.-W. Rix, E. J. Bernard, E. F. Bell, B. Sesar, A. M. N. Ferguson, E. F. Schlafly, C. T. Slater, W. S. Burgett, K. C. Chambers, H. Flewelling, K. A. Hodapp, N. Kaiser, R.-P. Kudritzki, R. H. Lupton, E. A. Magnier, N. Metcalfe, J. S. Morgan, P. A. Price, J. L. Tonry, R. J. Wainscoat, and C. Waters. A New Faint Milky Way Satellite Discovered in the Pan-STARRS1 3π Survey. *ApJ*, 802:L18, Apr. 2015b. doi: 10.1088/2041-8205/802/2/L18.

B. Letarte, S. Demers, P. Battinelli, and W. E. Kunkel. The Extent of NGC 6822 Revealed by Its C Star Population. *AJ*, 123:832–839, Feb. 2002. doi: 10.1086/338319.

A. Liddle. *An Introduction to Modern Cosmology, Second Edition*. May 2003.

M. R. Lovell, V. Eke, C. S. Frenk, L. Gao, A. Jenkins, T. Theuns, J. Wang, S. D. M. White, A. Boyarsky, and O. Ruchayskiy. The haloes of bright satellite galaxies in a warm dark matter universe. *MNRAS*, 420:2318–2324, Mar. 2012. doi: 10.1111/j.1365-2966.2011.20200.x.

N. F. Martin, D. L. Nidever, G. Besla, K. Olsen, A. R. Walker, A. K. Vivas, R. A. Gruendl, C. C. Kaleida, R. R. Muñoz, R. D. Blum, A. Saha, B. C. Conn, E. F. Bell, Y.-H. Chu, M.-R. L. Cioni, T. J. L. de Boer, C. Gallart, S. Jin, A. Kunder, S. R. Majewski, D. Martinez-Delgado, A. Monachesi, M. Monelli, L. Monteagudo, N. E. D. Noël, E. W. Olszewski, G. S. Stringfellow, R. P. van der Marel, and D. Zaritsky. Hydra II: A Faint and Compact Milky Way Dwarf Galaxy Found in the Survey of the Magellanic Stellar History. *ApJ*, 804:L5, May 2015. doi: 10.1088/2041-8205/804/1/L5.

M. L. Mateo. Dwarf Galaxies of the Local Group. *ARA&A*, 36:435–506, 1998. doi: 10.1146/annurev.astro.36.1.435.

L. D. Matthews, E. Gérard, and T. Le Bertre. Discovery of a shell of neutral atomic hydrogen surrounding the carbon star IRC+10216. *MNRAS*, 449:220–233, May 2015. doi: 10.1093/mnras/stv263.

A. W. McConnachie. The Observed Properties of Dwarf Galaxies in and around the Local Group. *AJ*, 144:4, July 2012. doi: 10.1088/0004-6256/144/1/4.

M. Milgrom. A modification of the Newtonian dynamics as a possible alternative to the hidden mass hypothesis. *ApJ*, 270:365–370, July 1983. doi: 10.1086/161130.

H. L. Morrison, M. Mateo, E. W. Olszewski, P. Harding, R. C. Dohm-Palmer, K. C. Freeman, J. E. Norris, and M. Morita. Mapping the Galactic Halo. I. The "Spaghetti" Survey. *AJ*, 119:2254–2273, May 2000. doi: 10.1086/301357.

C. D. Murray and S. F. Dermott. *Solar system dynamics*. 1999.

J. F. Navarro, C. S. Frenk, and S. D. M. White. A Universal Density Profile from Hierarchical Clustering. *ApJ*, 490:493–508, Dec. 1997.

E. Papastergis and F. Shankar. An assessment of the "too big to fail" problem for field dwarf galaxies in view of baryonic feedback effects. *ArXiv e-prints*, Nov. 2015.

S. Perlmutter, G. Aldering, G. Goldhaber, R. A. Knop, P. Nugent, P. G. Castro, S. Deustua, S. Fabbro, A. Goobar, D. E. Groom, I. M. Hook, A. G. Kim, M. Y. Kim, J. C. Lee, N. J. Nunes, R. Pain, C. R. Pennypacker, R. Quimby, C. Lidman, R. S. Ellis, M. Irwin, R. G. McMahon, P. Ruiz-Lapuente, N. Walton, B. Schaefer, B. J. Boyle, A. V. Filippenko, T. Matheson, A. S. Fruchter, N. Panagia, H. J. M. Newberg, W. J. Couch, and T. S. C. Project. Measurements of Ω and Λ from 42 High-Redshift Supernovae. *ApJ*, 517:565–586, June 1999. doi: 10.1086/307221.

Planck Collaboration, P. A. R. Ade, N. Aghanim, M. I. R. Alves, C. Armitage-Caplan, M. Arnaud, M. Ashdown, F. Atrio-Barandela, J. Aumont, H. Aussel, and et al. Planck 2013 results. I. Overview of products and scientific results. *A&A*, 571:A1, Nov. 2014a. doi: 10.1051/0004-6361/201321529.

Planck Collaboration, P. A. R. Ade, N. Aghanim, C. Armitage-Caplan, M. Arnaud, M. Ashdown, F. Atrio-Barandela, J. Aumont, C. Baccigalupi, A. J. Banday, and et al. Planck 2013 results. XVI. Cosmological parameters. *A&A*, 571:A16, Nov. 2014b. doi: 10.1051/0004-6361/201321591.

J. A. Rich, S. E. Persson, W. L. Freedman, B. F. Madore, A. J. Monson, V. Scowcroft, and M. Seibert. A New Cepheid Distance Measurement and Method for NGC 6822. *ApJ*, 794:107, Oct. 2014. doi: 10.1088/0004-637X/794/2/107.

D. O. Richstone and S. Tremaine. Measuring mass-to-light ratios of spherical stellar systems by core fitting. *AJ*, 92:72–74, July 1986. doi: 10.1086/114135. URL `http://ukads.nottingham.ac.uk/abs/1986AJ.....92...72R`.

A. G. Riess, A. V. Filippenko, P. Challis, A. Clocchiatti, A. Diercks, P. M. Garnavich, R. L. Gilliland, C. J. Hogan, S. Jha, R. P. Kirshner, B. Leibundgut, M. M. Phillips, D. Reiss, B. P. Schmidt, R. A. Schommer, R. C. Smith, J. Spyromilio, C. Stubbs, N. B. Suntzeff, and J. Tonry. Observational Evidence from Supernovae for an Accelerating Universe and a Cosmological Constant. *AJ*, 116:1009–1038, Sept. 1998. doi: 10.1086/300499.

B. Rogers, I. Ferreras, S. Kaviraj, A. Pasquali, and M. Sarzi. Star formation and nuclear activity in close pairs of early-type galaxies. *MNRAS*, 399:2172–2182, Nov. 2009. doi: 10.1111/j.1365-2966.2009.15422.x.

D. J. Sand, K. Spekkens, D. Crnojević, J. R. Hargis, B. Willman, J. Strader, and C. J. Grillmair. Antlia B: A Faint Dwarf Galaxy Member of the NGC 3109 Association. *ApJ*, 812:L13, Oct. 2015. doi: 10.1088/2041-8205/812/1/L13.

A. Sandage, M. Sandage, and J. Kristian. *Galaxies and the Universe*. 1975.

L. F. Sibbons, S. G. Ryan, M.-R. L. Cioni, M. Irwin, and R. Napiwotzki. The AGB population of NGC 6822: distribution and the C/M ratio from JHK photometry. *A&A*, 540:A135, Apr. 2012. doi: 10.1051/0004-6361/201118365.

L. F. Sibbons, S. G. Ryan, R. Napiwotzki, and G. P. Thompson. Spectral classification of photometrically selected AGB candidates in NGC 6822. *A&A*, 574:A102, Feb. 2015. doi: 10.1051/0004-6361/201423981.

M. F. Skrutskie, R. M. Cutri, R. Stiening, M. D. Weinberg, S. Schneider, J. M. Carpenter, C. Beichman, R. Capps, T. Chester, J. Elias, J. Huchra, J. Liebert, C. Lonsdale, D. G. Monet, S. Price, P. Seitzer, T. Jarrett, J. D. Kirkpatrick, J. E. Gizis, E. Howard, T. Evans, J. Fowler, L. Fullmer, R. Hurt, R. Light, E. L. Kopan, K. A. Marsh, H. L. McCallon, R. Tam, S. Van Dyk, and S. Wheelock. The Two Micron All Sky Survey (2MASS). *AJ*, 131:1163–1183, Feb. 2006. doi: 10.1086/498708.

L. S. Sparke and J. S. Gallagher, III. *Galaxies in the Universe*. Feb. 2007.

V. Springel, S. D. M. White, A. Jenkins, C. S. Frenk, N. Yoshida, L. Gao, J. Navarro, R. Thacker, D. Croton, J. Helly, J. A. Peacock, S. Cole, P. Thomas, H. Couchman, A. Evrard, J. Colberg, and F. Pearce. Simulations of the formation, evolution and clustering of galaxies and quasars. *Nature*, 435:629–636, June 2005. doi: 10.1038/nature03597.

V. Springel, J. Wang, M. Vogelsberger, A. Ludlow, A. Jenkins, A. Helmi, J. F. Navarro, C. S. Frenk, and S. D. M. White. The Aquarius Project: the subhaloes of galactic haloes. *MNRAS*, 391:1685–1711, Dec. 2008. doi: 10.1111/j.1365-2966.2008.14066.x.

E. Starkenburg, A. Helmi, H. L. Morrison, P. Harding, H. van Woerden, M. Mateo, E. W. Olszewski, T. Sivarani, J. E. Norris, K. C. Freeman, S. A. Shectman, R. C. Dohm-Palmer, L. Frey, and D. Oravetz. Mapping the galactic halo. viii. quantifying substructure. *The Astrophysical Journal*, 698(1):567, 2009. URL `http://stacks.iop.org/0004-637X/698/i=1/a=567`.

G. Thompson, S. Ryan, and L. Sibbons. The rotation of the halo of NGC 6822 from the radial velocities of carbon stars. *MNRAS*, 2016.

E. J. Tollerud, J. S. Bullock, L. E. Strigari, and B. Willman. Hundreds of Milky Way Satellites? Luminosity Bias in the Satellite Luminosity Function. *ApJ*, 688:277-289, Nov. 2008. doi: 10.1086/592102.

J. Tonry and M. Davis. A survey of galaxy redshifts. I - Data reduction techniques. *AJ*, 84: 1511–1525, Oct. 1979. doi: 10.1086/112569.

T. S. van Albada, J. N. Bahcall, K. Begeman, and R. Sancisi. Distribution of dark matter in the spiral galaxy NGC 3198. *ApJ*, 295:305–313, Aug. 1985. doi: 10.1086/163375.

G. T. van Belle, C. Paladini, B. Aringer, J. Hron, and D. Ciardi. The PTI Carbon Star Angular Size Survey: Effective Temperatures and Non-sphericity. *ApJ*, 775:45, Sept. 2013. doi: 10.1088/0004-637X/775/1/45.

J. Veljanoski, A. M. N. Ferguson, A. D. Mackey, A. P. Huxor, J. R. Hurley, E. J. Bernard, P. Côté, M. J. Irwin, N. F. Martin, W. S. Burgett, K. C. Chambers, H. Flewelling, R. Kudritzki, and C. Waters. The globular cluster system of NGC 6822. *MNRAS*, 452:320–332, Sept. 2015. doi: 10.1093/mnras/stv1259.

D. T. F. Weldrake, W. J. G. de Blok, and F. Walter. A high-resolution rotation curve of NGC 6822: a test-case for cold dark matter. *MNRAS*, 340:12–28, Mar. 2003. doi: 10.1046/j.1365-8711.2003.06170.x.

K. W. Willett, C. J. Lintott, S. P. Bamford, K. L. Masters, B. D. Simmons, K. R. V. Casteels, E. M. Edmondson, L. F. Fortson, S. Kaviraj, W. C. Keel, T. Melvin, R. C. Nichol, M. J. Raddick, K. Schawinski, R. J. Simpson, R. A. Skibba, A. M. Smith, and D. Thomas. Galaxy Zoo 2: detailed morphological classifications for 304 122 galaxies from the Sloan Digital Sky Survey. *MNRAS*, 435:2835–2860, Nov. 2013. doi: 10.1093/mnras/stt1458.

M. Zemp. The Structure of Cold Dark Matter Halos: Recent Insights from High Resolution Simulations. *Modern Physics Letters A*, 24:2291–2305, 2009. doi: 10.1142/S0217732309031880.

A. Zolotov, A. M. Brooks, B. Willman, F. Governato, A. Pontzen, C. Christensen, A. Dekel, T. Quinn, S. Shen, and J. Wadsley. Baryons Matter: Why Luminous Satellite Galaxies have Reduced Central Masses. *ApJ*, 761:71, Dec. 2012. doi: 10.1088/0004-637X/761/1/71.

F. Zwicky. Die Rotverschiebung von extragalaktischen Nebeln. *Helvetica Physica Acta*, 6:110–127, 1933.